ALMA MATER STUDIORUM · UNIVERSITÀ DI BOLOGNA

DOTTORATO DI RICERCA IN

Fisica

Ciclo XXVII

In-situ and real time scanning probe microscopy of organic ultra thin films

Presentata da: Stefano Chiodini

Coordinatore Dottorato:
Prof. Fabio Ortolani

Relatore:
 Prof.ssa Beatrice Fraboni

Co-relatori:
Dr. Cristiano Albonetti
Prof. Fabio Biscarini

Esame finale anno: 2015

Ad Adrica,
al CNR e...
e al lavoro!

Ringraziamenti

Sono stati tre anni intensi, decisamente volati.

Ringrazio la mia famiglia, Franco, Marisa, Davide, Laura, Ines, compresa Ilaria che presto si unirà a noi. Ringrazio Paola e Guido per l'amore verso la cultura in tutte le sue forme. Certe cose viste sin da 'cinni' rimangono. Eccome. Ringrazio gli amici di Bologna per le belle serate passate insieme e contemporaneamente il supporto nei momenti difficili (i.e. parte del secondo anno di dottorato). Ringrazio Bruno Franchi per la disponibilità e la competenza. Chissà l'ingegnere cosa starà pensando adesso... La matematica serve si o no? Mè al deg ed sé (all'1%!). Ringrazio gli amici e i colleghi del CNR, non certo solo un luogo di lavoro ma ben di più. Nonostante tutto, ovviamente. Un ringraziamento speciale a Fabio Biscarini e Cristiano Albonetti: Fabio per avermi dato l'opportunità di entrare al CNR, con tutte le conseguenze annesse: l'emozione del primo lavoro, la possibilità di lavorare in un gruppo.... Tanta roba come si suol dire, e in un periodo come questo dove non si trova un lavoro neanche a piangere, questo non è poco. Ringrazio poi Cristiano: la quotidiana presenza, energia, voglia, competenza, sostegno morale sono stati determinanti. E mi sono anche divertito. La transizione da teorico a sperimentale (o sperimentorico) te la devo tutta. Chi l'avrebbe detto? io no.

Contents

Introduction

In recent decades, Organic Thin Film Transistors (OTFTs) have focused lots of interest due to their low cost, large area and flexible properties which have brought them to be considered the building blocks of the future organic electronics[1–4]. The first OTFT was fabricated in 1986 utilizing a film of polythiophene as a semiconducting layer [5]. In 1989, Horowitz [6] reported the first OTFT employing a small conjugated molecule (sexithiophene- 6T). Mobilities close to amorphous silicon's one have been obtained and a broad spectrum of novel semiconductors and new fabrication techniques have led to a remarkable progress in performance of OTFTs[7]. The progress in understanding the physics behind OTFTs has been possible due to advances in Ultra High Vacuum (UHV) growth, such as Organic Molecular Beam Epitaxy (OMBE)[8], as a means to deposite organic thin films in a control manner and with high chemical purity, and also to techniques such as X-ray reflectivity, low energy electron diffraction (LEED) and Scanning Probe Microscopy (SPM) which reveal the morphology of the thin film and provide evidences for the predictions of growth theories. More specifically, in-situ and real time techniques have developed as a powerful tool to get unprecedent insight into complex dynamic processes, that cannot be unravelled by common ex-situ measurements[9,10].

Experimentally, devices based on the same organic material deposited in different ways, i.e. by varying the deposition rate of the molecules, show different electrical performance. As predicted theoretically, this is due to the speed and rate by which charge carriers can be transported by hopping in organic thin films, transport that depends on the molecular arrangement of the molecules.

This strongly suggests a correlation between the morphology of the organic semiconductor and the performance of the OTFT. Several contributions on this issue are present in literature. Among them, the CNR-ISMN group in Bologna, have contributed with several publications ranging from the study of the activation-diffusional energies for 6T [11,12], to the discovery of which layers mainly contribute to charge transport in OFETs [13], to the result that the effective Debye length in OTFTs depends on the multiscale morphology [14].

Extensive works have been published on the correlation between morphology and OTFTs performance ([13,14]) but still, a complete picture of the physics behind has to be obtained. This is why we propose an in-situ real time SPM study of organic semiconductor growth as an almost unprecedent experiment with the aim to fully describe the morphological evolution of the ultra-thin film and find the relevant morphological parameters affecting the OTFT electrical response.

For the case of 6T on silicon oxide, we have shown that the growth mechanism is 2D+3D, with a roughening transition ([15]) at the third layer. Then, we have fitted the experimental data, i.e. the root mean square roughness, with a Distributed Growth Model (DGM) ([9,16]) obtaining a good agreement. This shows that, to have a full description of the growth mechanism, interlayer diffusion has to be taken into account. Moreover, trying to estimate the Ehrlich-Schwoebel barrier ([17,18]), we noticed the experimental temperature evolution of the growth exponent *beta* ([19]) to have an opposite trend to the one expected, specifically a rapid roughening behaviour ([20]). This is interpreted as the signature of a more complex growth dynamics, which probably takes into account also upward molecules current ([20]) and/or downward funneling ([21]). The desorption energy of 6T on silicon oxide, the diffusion energies and fractal dimensions were also calculated.

Aiming to further investigate the very first steps of growth, i.e. the nucleation centers, following ([22]), we tried to obtain an experimental definition of nucleation center. To do this, we planned to perform Electrostatic Force Microscopy (EFM) measurements on bare silicon oxide to image possible surface regions with different surface potential, as expected in ([22]). Then, 6T molecules at very low coverage ($< 5\% ML$) are deposited. Such experiment aims to observe if the positions of the nucleation centers are correlated with the electrostatic potential changes on the substrate, as previously imaged by EFM.

Unfortunately, due to a technical problem in the z-piezo of the microscope, which required the work of a specialist from Omicron NanoTechnology GmbH ([23]), stopping the machine for few months, we were not able to complete this work which will be finished in the next future. Although the experimental part of the work was not achieved, we developed an original mathematical model to estimate theoretically and more accurately than before, the capacitance of an EFM tip in front of a metallic substrate. Analytical expression for this capacitance are important for a better understanding of EFM images and the limit of resolution of an EFM microscope ([24,25]). In the future, we aim to extend this EFM theoretical model, even in presence of thin film in between the EFM tip and the substrate([26]), a work which will

describe more accurately also the experimental definition of the nucleation center concept presented above.

Finally, we also realized and finished two additional works. In the first, we obtained Ultra High Vacuum (UHV) non contact Atomic Force Microscopy (AFM) images of 6T flat lying molecules layer both on silicon oxide and on top of 6T islands. This molecular configuration was already investigated by several techniques ([27,28]), but still, at our knowledge, UHV AFM images clearly showing their existence were lacking.

Moreover, we also performed ex-situ AFM imaging on a bilayer film composed of pentacene (a p-type semiconductor) and C60 (an n-type semiconductor). The aim was to relate the in-situ real time electrical characterization of the bilayer transistor with the interface morphology of the heterojunction.

Bibliography

[1] C. Dimitrakopoulos and P. Malenfant. *Advanced Materials*, **14**, 99 (2002)

[2] J. Fraxedas. *Advanced Materials*, **14**, 1603 (2002)

[3] G. Horowitz, R. Hajlaoui, H. Bouchriha, R. Bourguiga and M. Hajlaoui. *Advanced Materials*, **10**, 923 (1998)

[4] T. W. Kelley, P. F. Baude, C. Gerlach, D. E. Ender, D. Muyres, M. Haase, D. E. Vogel and S. D. Theiss. *Chemistry of Materials*, **16**, 4413 (2004)

[5] A. Tsumura, H. Koezuka and T. Ando. *Applied Physics Letters*, **49**, 1210 (1986)

[6] G. Horowitz, D. Fichou, X. Peng, Z. Xu, F. Garnier, M. Molrculaires, H. Dunant and M. Balkanski. *Solid State Communications*, **72**, 381 (1989)

[7] R. A. Street. *Advanced Materials*, **21**, 2007 (2009)

[8] S. R. Forrest. *Chemical reviews*, **97**, 1793 (1997)

[9] A. C. Mayer, R. Ruiz, H. Zhou, R. L. Headrick, A. Kazimirov and G. G. Malliaras. *Physical Review B*, **73**, 1 (2006)

[10] W. Braun, B. Jenichen, V. M. Kaganer, L. Shtukenberg, A. G. Daweritz and K. H. Ploog. *Surface Science*, **525**, 126 (2003)

[11] F. Biscarini. *Physical Review B*, **52** (1995)

[12] F. Biscarini, P. Samorì, O. Greco and R. Zamboni. *Physical Review Letters*, **1**, 2389 (1997)

[13] F. Dinelli, M. Murgia, P. Levy, M. Cavallini, F. Biscarini and D. de Leeuw. *Physical Review Letters*, **92**, 116802 (2004)

[14] A. Shehu, S. D. Quiroga, P. D'Angelo, C. Albonetti, F. Borgatti, M. Murgia, A. Scorzoni, P. Stoliar and F. Biscarini. *Physical Review Letters*, **104**, 246602 (2010)

[15] X. Zhang, E. Barrena, D. de Oteyza and H. Dosch. *Surface Science*, **601**, 2420 (2007)

[16] P. I. Cohen, G. S. Petrich, P. R. Pukite and G. J. Whaley. *Surface Science*, **216**, 222 (1989)

[17] G. Ehrlich. *The Journal of Chemical Physics*, **44**, 1039 (1966)

[18] R. L. Schwoebel. *Journal of Applied Physics*, **37**, 3682 (1966)

[19] A.-L. Barabasi and H. E. Stanley. *Fractal Concepts In Surface Growth*. Cambridge University Press (1995)

[20] A. Durr, F. Schreiber, K. Ritley, V. Kruppa, J. Krug, H. Dosch and B. Struth. *Physical Review Letters*, **90**, 016104 (2003)

[21] J. W. Evans, D. E. Sanders, P. A. Thiel and A. E. DePristo. *Phys. Rev. B*, **41**, 5410 (1990)

[22] O. M. Roscioni, L. Muccioli, R. G. Della Valle, A. Pizzirusso, M. Ricci and C. Zannoni. *Langmuir*, **29**, 8950 (2013)

[23] 'website Omicron:'. http://omicron.de/en/home

[24] S. Belaidi, P. Girard and G. Leveque. *Journal of Applied Physics*, **81**, 1023 (1997)

[25] G. Gomila, J. Toset and L. Fumagalli. *Journal of Applied Physics*, **104**, 024315 (2008)

[26] L. Fumagalli, G. Ferrari, M. Sampietro and G. Gomila. *Applied Physics Letters*, **91**, 243110 (2007)

[27] M. A. Loi, E. Da Como, F. Dinelli, M. Murgia, R. Zamboni, F. Biscarini and M. Muccini. *Nat. Mat.*, **4**, 81 (2005)

[28] F. Dinelli, C. Albonetti and O. V. Kolosov. *Ultramicroscopy*, **111**, 267 (2011)

Chapter 1

Organic thin film growth

1.1 Organic Molecular Beam Epitaxy

During the past decades, a huge progress has been made in growing ultra-thin organic films and multilayer structures with a wide range of exciting properties. Perhaps the most important advance has been the use of **Ultra High Vacuum (UHV) growth, sometimes referred to as Organic Molecular Beam Deposition (OMBD), or Organic Molecular Beam Epitaxy (OMBE)**, as a means to achieve, for the first time, both monolayer control over the growth of organic thin films with extremely high chemical purity and structural precision.
When combined with the ability to perform in-situ high-resolution structural diagnostics of the films as they are being deposited, techniques such as OMBE have provided an entirely new prospect for understanding many of the fundamental structural and optoelectronic properties of ultra-thin organic films systems.

The most common means for the OMBE growth of organic thin films is to use an ultrahigh-vacuum apparatus. Typically growth occurs by the sublimation in a background vacuum ranging from 10^{-7} to 10^{-11} mbar of a highly purified powder or a melt of the organic source material from a temperature controlled oven or Knudsen cell. The evaporant is collimated by passing through a series of orifices, after which it is deposited on a substrate held perpendicular to the beam approximately 10-20 cm from the source. The flux of the molecular beam is controlled by a combination of oven temperature as well as mechanical shutter which can switch the beam flux from on to off. By sequentially shuttering the beam flux from more than one Knudsen cell, multilayer structure consisting of alternating layers of different compounds can be grown by this method. Growth rate is measured using a Quartz Crystal Balance (QCB) which monitors the film thickness.

One significant advantage of using OMBE is that numerous in situ film diag-

nostics can be employed both during and immediately after growth. Many growth
chambers are equipped with reflection high energy electron diffraction (RHEED)
allowing in-situ determination of the thin-film crystalline structure. Other diagnos-
tics include low-energy electron diffraction (LEED). Finally, many other vacuum
analysis techniques such as UHV STM, Auger electron spectroscopy, etc. have all
been employed in conjunction with OMBE.

Like for inorganic film growth theory ([1,2]), the two standard approaches in any
theoretical treatment of kinetics are to explain the system in terms of the **ther-
modynamic driving forces**, or in terms of the **fundamental rate equations**.
The rate equations can be further subdivided into an **atomistic, or microscopic**,
approach that accounts for individual molecules as they go through the various
processes (adsorption, desorption, diffusion, capture and release) or a **phenomeno-
logical, or macroscopic**, explanation that looks for correlations and the so called
scaling laws over large distances.
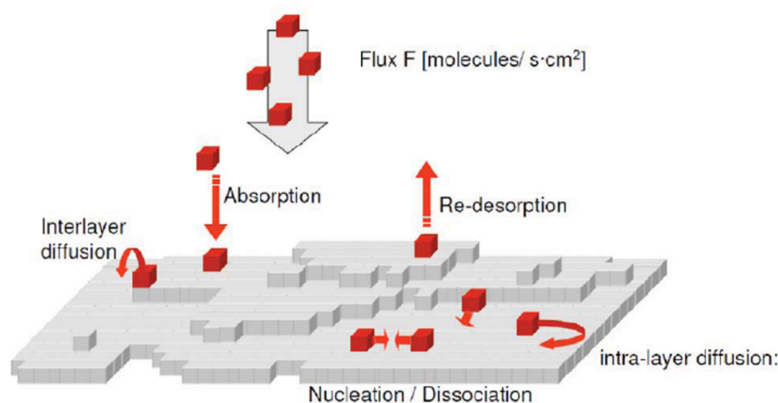
Figure 1.1: Typical processes happening at a surface: absorption, desorption, nu-
cleation, dissociation and (inter/intralayer) diffusion.

**The dynamics of the first monolayer can be explained by calculating the
density of islands** that consists of few molecules as they nucleate and evolve in
time. The results from SPM, LEEM, or Transmission Electron Microscopy (TEM)
can be used to understand the dynamics and compare with theory. Through the use
of classical nucleation theory, one can extract valuable information like the critical
cluster size and the energy of diffusion for a monomer.

**To understand the film evolution over several monolayers, it helps to
consider the layer occupancies** (or fractional coverages) of each layer, rather than

the individual islands in each layer, because the details and experimental methods become daunting otherwise. For instance, there have been attempts to extend the rate equation approach to incorporate the subsequent layers, but with little success due to the increased number of parameters needed to quantify the system. Comparing these theories with experimental data can yield information on the coverage of each layer with time, the critical coverage for coalescence, the island shape, and the presence and magnitude of an Ehrlich-Schwoebel barrier ([3,4]).

1.2 Characterization of the first layer morphology

The morphology of the surface is determined by the interplay between deposition, desorption and diffusion of a flux Φ of molecules ($molecules/(s \cdot cm^2)$); the latter two phenomena can be described by energy values, E_{des} and E_{dif} which one can calculate experimentally.

1.2.1 Desorption

An effect competing with deposition is desorption which means that some atoms deposited on the surface leave the surface itself. The desorption probability depends on how strongly the atom is bounded to the crystal surface.

The usual procedure for measuring the lifetime of a deposited molecule or atom is to measure the average time τ spent by the atom on the surface from deposition to desorption. Often, it is found ([5]) τ to obey the Arrhenius law:

$$\tau(T) \sim exp(E_{des}/kT) \tag{1.1}$$

From this equation, one can understand that the real value to be considered is not the value of E_{des} but, instead, its relation with kT (which at RT is equal to $\sim 26meV$). Specifically, if we have $E_{des} \gg kT$ we will have weak desorption, while, on the other hand, if $E_{des} \ll kT$, we will have a strong desorption.

For our data analysis in Chapter 7 we will make use of an equivalent equation, not related to τ but to the measured flux of molecules in case desorption can not be neglected:

$$\Phi(T) \sim exp(E_{des}/kT) \tag{1.2}$$

This expression relates the measured flux to the temperature T of the substrate. As can be seen, if one increases T, the QCB will measure a decrease in the flux due to desorption.

1.2.2 Surface diffusion

In Molecular Beam Epitaxy (MBE) the deposited atoms diffuse on the crystal surface, searching for the energetically most favourable position. Surface diffusion is an activated process: for an atom on the surface, to diffuse to the next lattice position, it must overcome the lattice potential existing between two neighbouring positions.

The average number of jumps in a unit time interval has an exponential temperature dependence, given by the Arrhenius law ([5]):

$$N \sim exp(-\frac{E_{dif}}{kT}) \tag{1.3}$$

More often, the diffusion constant D (for admolecules on the substrate) is taken into account. This parameter appears in Fick's law ([6]) and the following relation holds true for a square lattice:

$$D \sim exp(-\frac{E_{dif}}{kT}) \tag{1.4}$$

D is correlated with the average distance l between the point of adsorption and the point of desorption (the diffusion length) by the following expression:

$$l = \sqrt{D\tau} \sim exp(\frac{E_{des} - E_{dif}}{2kT}) \tag{1.5}$$

In Paragraph 1.2.4 the method which we will use to calculate E_{dif} in Chapter 7 is presented.

1.2.3 Thermodynamic driving forces

The relevant thermodynamic quantity concerning the formation of a new nucleus, let's say a j-cluster (an island made of j molecules), is the gain in free energy which is given by ([1]):

$$\Delta G = -j\Delta\mu + j^{2/3}X \tag{1.6}$$

where $\Delta\mu$ is the chemical potential difference (or supersaturation) while X is a geometrical factor dependent on the system shape.

Depending on the shape of the crystal, the surface energy terms, and the supersaturation, there exists a value of j for which the free energy is at maximum and therefore **the attachment of one more molecule will make the crystal stable**. The size of the island corresponding to this maximum is known as the **critical island size**, denoted by i^*.

This formalism has been continued by Verlaak ([7]) for the case of several important organic semiconductors (pentacene, tetracene and perylene) grown on inert substrates. **In ([7]), it is shown that**:

- no growth takes place if the supersaturation $\Delta\mu$ is lower than zero

- only 3D growth will be observed if the supersaturation is (positive and) lower than the critical value $\Delta\mu_{cr} = \Psi_{mol-mol} - \Psi_{mol-sub}$, where $\Psi_{mol-mol}$ is the strength of the interatomic interaction potential in the direction normal to the surface and $\Psi_{mol-sub}$ is the strength of the interaction potential between a molecule and the substrate ($\Psi_{mol-sub} = 0$ for a perfectly inert substrate)

- 3D plus 2D growth will happen when $\Delta\mu_{cr} < \Delta\mu < 2\Delta\mu_{cr}$

- there will be only 2D growth when, instead, $\Delta\mu > 2\Delta\mu_{cr}$ then, in a first approximation ([7]), only growth conditions below the dotted lines will give rise to continuous films
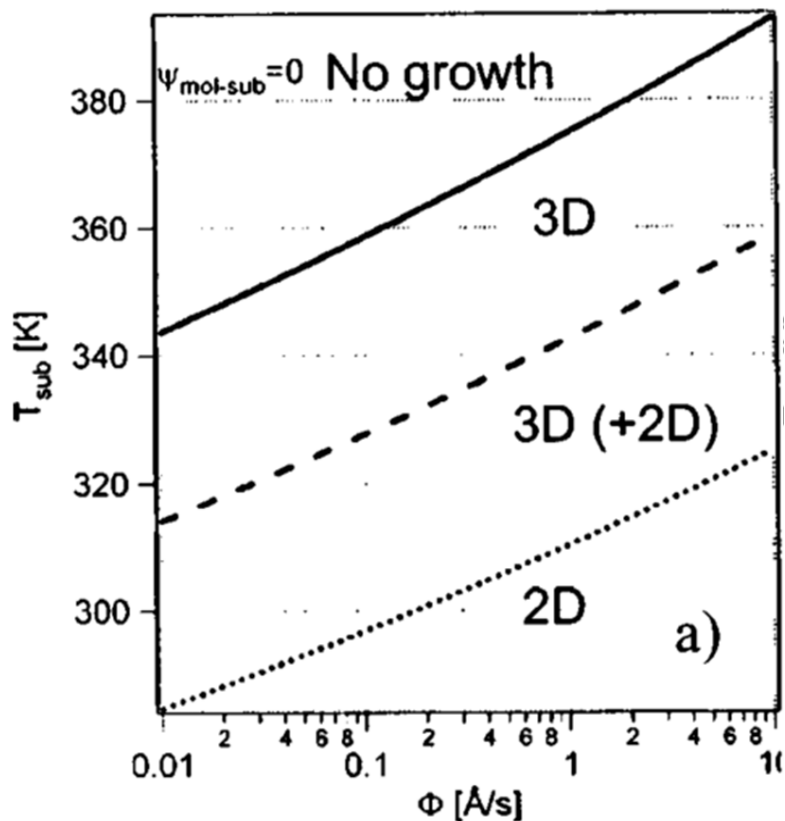

Figure 1.2: Growth modes for pentacene assuming a perfectly inert substrate ($\Psi_{mol-sub} = 0$). Depending on substrate temperature and flux of molecules, different kinds of growth are possible.

1.2.4   Atomistic rate equations

The classical nucleation theory ([6]) starts from rate equations for the island density n_1 for monomers and n_s for islands with size $s \geq 2$. **Several assumption are made in the beginning and the results will be influenced by them:**

- **the flux of molecules, Φ, is constant**

- **only the monomers can diffuse**

- **when one molecule meets another, they form an immobile cluster**

- **if one molecule meets an island, it sticks to its edge and becomes immobile**

- **when an atom arrives on the top of an existing island it will continue diffusing, eventually falling down if it reaches the edge of the island, or, due to the Ehrlich-Schwoebel barrier, the atom may not leave the upper terrace**

- **the aggregation process is irreversible, which means that it is not considered the probability that a monomer can detach from the edge of an island, or that a dimer can break**

The rate Γ_s, which is the rate to form islands of size $s + 1$ from islands of size s, is given by ([8]):

$$\Gamma_s = \sigma_s D n_1 n s - \gamma_{s+1} n_{s+1} \tag{1.7}$$

where σ_s is the capture number and γ_s is the rate at which monomers detach from an island of size s. D is the surface diffusion constant for the monomers, see subsection 1.2.2.

The change of the monomer density, is given by ([8]):

$$\frac{dn_1}{dt} = \Phi - \frac{n_1}{\tau} - 2\Gamma_1 - \sum_{s \geq 2} \Gamma_s \tag{1.8}$$

where τ is the residence time on the substrate of the molecules due to desorption. Depending on whether desorption is strong or not we can distinguish two regimes:

- desorption is relevant: this is called **incomplete condensation regime**. τ is small compare with n_1 and so, the second term in Equation 1.8 cannot be ruled out

- desorption is negligible: this is the **complete condensation regime and is often true for the growth conditions used in OTFT fabrication**. The residence time τ is big and the second term can be excluded.

Finally, the change of the island densities with size s is given by:

$$\frac{dn_s}{dt} = \Gamma_{s-1} - \Gamma_s \qquad (1.9)$$

The solution of this set of differential equations for n_1 and n_s, can be found in ([9]). In Figure 1.3, a log-log plot of the densities of monomers (n_1) and total stable nuclei ($n = \sum_{s\geq2} n_s$) is plotted versus the total coverage for a specific ratio R of the diffusion constant and the rate:

$$R = \frac{D}{\Phi} \qquad (1.10)$$
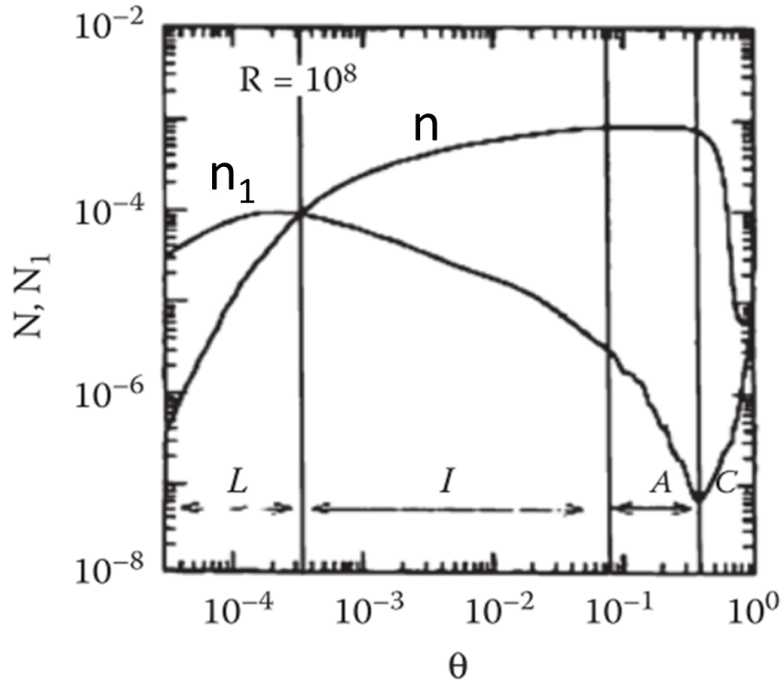
Figure 1.3: Comparison of the densities of monomers and stable nuclei as a function of coverage showing the different growth regimes ([9]).

As can be seen, **there are four distinct regions that correspond to a low coverage (L), an intermediate region (I), an aggregation region (A) and**

a coalescence region (C). In the low coverage regime, there are few stable nuclei, but many monomers diffusing on the surface. In the intermediate region, the island density and island size are increasing, which leads to a decreasing population of monomers: monomers still nucleate new islands but also start aggregating into existing ones. **The aggregation regime represents the stage where the number of stable nuclei remains constant: here there is no nucleation of new islands leading to scaling relations for the islands size distribution and island separation at different coverages**. In the coalescence regime, the number of islands begins to decrease as they merge, thus allowing monomers to diffuse around on top of the first layer and increasing their density.

In the case of the aggregation region, previously described, the (total) island density $n = \sum_{s \geq 2} n_s$ can be written as

$$n \sim \theta^{\frac{\chi}{i}} (R)^{-\chi} exp[\frac{E^{'}}{kT}] \tag{1.11}$$

which can be written also as:

$$n \sim \theta^{\frac{\chi}{i}} (\Phi)^{\chi} exp[\frac{E}{kT}] \tag{1.12}$$

Here, T refers to the temperature of the sample during growth, θ is the total coverage, χ is the scaling exponent, typically dependent on the critical nucleus size i^*, and $E^{'}$ and E are energies which depend on the desorption energy, the diffusion energy and the binding energy of the critical cluster.

There are several behaviours to be underlined checking this expression:

- the formula takes the form of a **scaling relation** $n \sim R^{-\chi}$, where D and Φ represent the diffusion and deposition process, competing with each other. In fact, the larger the flux, the less time the deposited molecules will have to diffuse before meeting another molecule on the surface. **Due to the scaling relation, we expect to obtain a system similar to the original if we change D and/or Φ, without changing R** ([5])

- **Provided sufficient (SPM) data is available, a plot of $\ln(n)$ vs $\ln(\Phi)$ allows the extraction of the critical nucleus i^* from the slope χ**

- **Plotting $\ln(n)$ vs (1/T), instead, one can extract again from the slope the energy parameter E**

Regarding the scaling exponent χ and E, the following Figure 1.4 shows all the possibilities. The main observation is the dependence from the growth mechanism (2D or 3D) and the disappearance of the desorption energy, called E_a in this table,

in the case of complete condensation regime.

Regime	3D islands	2D islands
Extreme incomplete	$p = 2i/3$ $E = (2/3)[E_i + (i+1)E_a - E_d]$	i $[E_i + (i+1)E_a - E_d]$
Initially incomplete	$p = 2i/5$ $E = (2/5)[E_i + iE_a]$	$i/2$ $[E_i + iE_a]$
Complete	$p = i/(i+2.5)$ $E = (E_i + iE_d)/(i+2.5)$	$i/(i+2)$ $(E_i + iE_d)/(i+2)$

Figure 1.4: Regimes of condensation: complete and incomplete. Depending on the scaling exponent, different energies dependence of the cluster density should be taken into account.

To conclude, also the average island size is an important parameter. Being n the total island density excluding monomers, the average island size is:

$$< s >= \frac{\sum_{s \geq 2} s n_s}{\sum_{s \geq 2} n_s} = \frac{\theta - n_1}{n} \tag{1.13}$$

From this relation and Equation 1.11, we can deduce the relation of the average island size with the flux of molecules:

$$< s > \sim \Phi^{-\chi} \tag{1.14}$$

which means that, due to a low flux of molecules, one has to expect bigger islands.

1.3   Characterization of multilayer morphology

1.3.1   Rms roughness

As already said, when studying a multilayer morphology, it helps to consider the layer occupancies with which, one can obtain the roughness parameter. To see this, we first define the surface to be the set of particles in the aggregate that are highest in each column. Then we can introduce:

- the **mean height** of the surface $\overline{h}$, is defined by

$$\overline{h}(t) = \frac{1}{L} \sum_{i=1}^{L} h(i,t) \tag{1.15}$$

where $h(i,t)$ is the height of column i at time t. From this one can define:

- the **roughness** of the surface, is defined by the root mean square (rms) fluctuation in the height

$$\sigma(L,t) = [\frac{1}{L} \sum_{i=1}^{L} (h(i,t) - \overline{h}(t))^2]^{1/2} \tag{1.16}$$

A typical plot of the time evolution of the surface roughness has two regions separated by a crossover time t_c, see Figure 7.14:
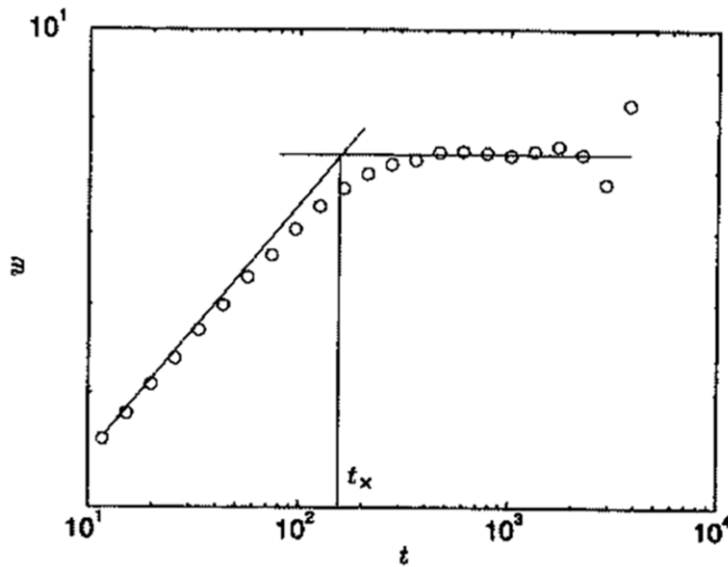

Figure 1.5: Roughness (w) vs. time (t) plot. t_x is the critical time t_c.

- Initially, the rms increases as a power of time

$$\sigma(L,t) \sim t^\beta \quad t \ll t_c \tag{1.17}$$

The exponent β, which is called the **growth exponent**, characterizes the time dependent dynamics of the roughening process.

- The power law increase in rms does not continue indefinitely, but is followed by a saturation regime during which the rms reaches a saturation value, σ_{sat}. In Figure 1.6 four different curves correspond to the time evolution of the rms obtained by simulating systems with four different system sizes L. As L increases, the saturation rms increases as well, and the dependence also follows a power law

$$\sigma_{sat} \sim L^{\alpha} \qquad t \gg t_c \tag{1.18}$$

  The exponent α, called the **roughness exponent**, is a second critical exponent that characterizes the rms of the saturated surface.

- The crossover time t_c at which the interface crosses over the two previous regimes, depends on the system size

$$t_c \sim L^z \tag{1.19}$$

  where z is called the **dynamic exponent**.
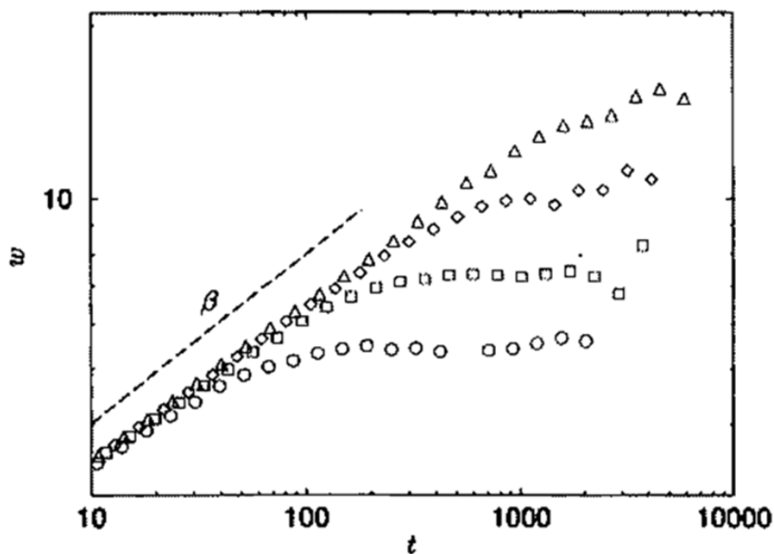
Figure 1.6: The roughness time evolution of different size L sample. Circles: L small, triangles: L large.

1.3.2 Layer occupancies

The most fundamental information on the vertical structure is provided by the distribution of coverages θ_j, also known as layer occupancies, for various layers j.

By convention $j = 0$ denotes the top layer of the substrate (so $\theta_0 = 0$). The total coverage or thickness (in monolayers [1]) of the deposited film equals $\theta = \sum_{j \geq 1} \theta_j = Ft$, for deposition flux F, and deposition time t in the absence of desorption. It is important to introduce the quantities, P_j, giving the exposed coverage of layer j, or the fraction of surface atoms of height j. Also, we let σ denote the root mean square (rms) roughness of the interface. Then one has:

$$P_j = \theta_j - \theta_{j+1} \tag{1.20}$$

$$\sum_j P_j = 1 \tag{1.21}$$

$$\theta = \sum_j j P_j \tag{1.22}$$

$$\sigma = [(j - \theta)^2 P_j]^{1/2} \tag{1.23}$$

Two extremes of behaviour are as follows (see Figure 1.7):
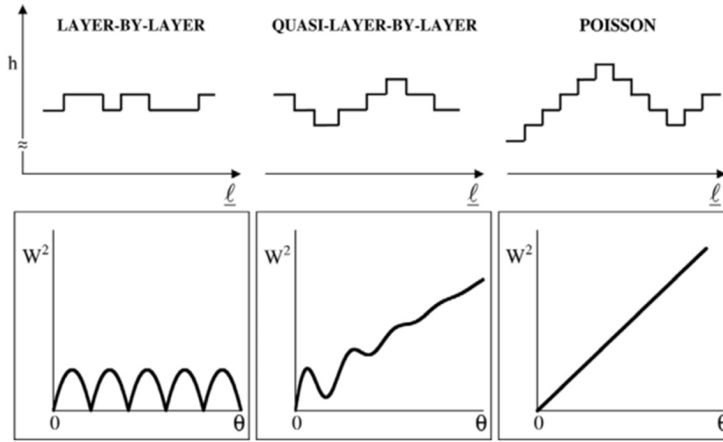
Figure 1.7: Picture of the height profile and evolution of the rms for layer by layer growth, quasi layer by layer growth and Poisson growth.

(i)**Layer by layer growth**. If $\theta = k + \delta\theta$, with $k = 0, 1, 2, 3..$, and $0 < \delta\theta \leq 1$, then the only non zero P_j are

$$P_k = 1 - \delta\theta \quad and \quad P_{k+1} = \delta\theta \tag{1.24}$$

---

[1]a coverage of one Monolayer (1 ML) is defined as the amount of material needed to cover the substrate with one layer of molecules having the backbone perpendicular to the surface

so $\sigma = [\delta\theta(1-\delta\theta)]^{1/2}$. Generally, all quantities vary periodically in this growth mode with a period of 1ML.

(ii)**Poisson growth**. For models of deposition in a simple cubic geometry with on top adsorption sites and no interlayer transport, the P_j are described by the Poisson distribution

$$P_j = exp(-\theta)\theta^j/j! \tag{1.25}$$

so $\sigma = \theta^{1/2}$. This growth mode is typically associated with low temperature deposition in the complete absence of thermal diffusion. It applies more generally for any degree of intralayer diffusion (but no interlayer transport), and might apply during the formation of mounds due to a large step edge barrier.

More generally, **kinetic roughening during multilayer growth** is described by the behaviour

$$\sigma \sim \theta^\beta \tag{1.26}$$

where β is the kinetic roughening or growth exponent.

For **quasi layer by layer growth**, involving slow kinetic roughening, σ will display damped oscillations about a slowly increasing time average curve. In these cases, one might attempt to fit P_j by the quasi-adiabatic form:

$$P_j \sim \sigma^{-1}f[(j-\theta)/\sigma] \tag{1.27}$$

with

$$\int f(y)\,dy = 1, \ \int y^2 f(y)\,dy = 1, \ and \ \int yf(y)\,dy = 0 \tag{1.28}$$

where f gives the shape of the film height distribution. Often, f is assumed to be Gaussian even if, for realistic growth models, non Gaussian behaviours are expected.

Regarding how to determine the layer occupancies, additional information about the surface evolution is required. The most common approach is to construct a deterministic, parameterized model for the evolution of coverages $\theta_n(t)$. Such models take the form of coupled, differential equations:

$$\frac{d\theta_n}{dt} = f(k_j, \theta_1, ..., \theta_{n-1}, \theta_n, \theta_{n+1}, ..., t) \tag{1.29}$$

where the function f represent the additional information imposed on the system, and k_j are some parameters typical of the system.

A large variety of models of this form have been developed over the last several decades. It is convenient to categorize these models according to how much they attempt to incorporate atom-level kinetics. Models by Kariotis ([10]), Trofimov ([11]) and Koponen ([12]) draw explicitly on nucleation theory and include additional equations representing the adatom and island densities on each layer. The next simplest

models, most notably those introduced by Cohen ([13]), do not explicitly attempt to model atom-level kinetics, but approximate these kinetics in the upper form. For example, the **distributed growth model**, see subsection 1.3.6, includes a mean field representation of the step density of a layer as a function of the total coverage, which in turn controls the amount of downhill interlayer diffusion ([13]). Finally, Braun ([14]) have developed a version which attempts, explicitly, to avoid modeling atomistic kinetics. Rather, the equations are coupled via intermediate functions chosen to be as simple as possible consistent with producing physically reasonable results for the functions $\theta_n(t)$.

Depending on the model, roughness will evolve with time, or θ_{TOT}. Here we will consider the following models (for simplicity, desorption will not be included):

- Perfect layer growth

- Non diffusive growth

- Diffusive growth

- Distributed growth

1.3.3   Perfect layer by layer growth

At one extreme every atom deposited goes into the topmost unfilled layer until that layer is completed. In this case, until the first layer is full one has:

$$\theta_0 = 1, \ \theta_1 = t/\tau, \ \theta_n = 0 \ for \ n > 1 \tag{1.30}$$

This gives a roughness of $rms = [(t/\tau)(1-t/\tau)]^{1/2}$ which is periodic, zero when one layer is completed, 50%ML when the coverage is half of each layer. Coverages and roughness are plotted in the following figure:
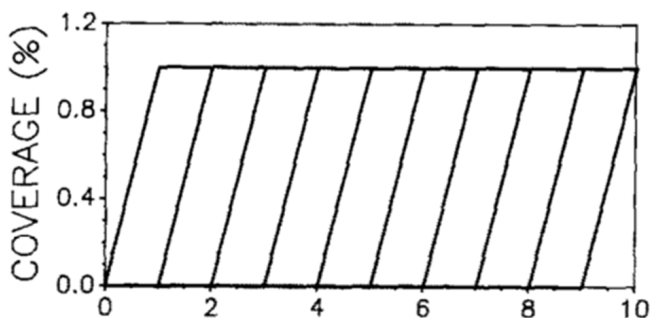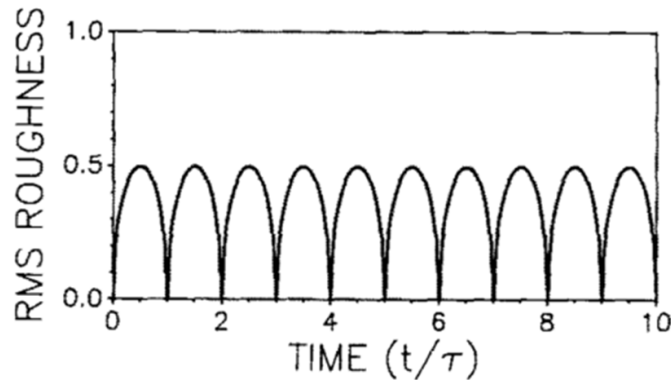
Figure 1.8: The coverages and rms roughness evolution with time corresponding to
a perfect layer by layer growth.

1.3.4   Non diffusive growth model

At the other extreme, once an atom impinges onto an exposed portion of a layer, the
adatom is confined to that layer. It is not allowed to cross a boundary defined by
a step edge. This model might approximately hold for growth at low temperature
or at high rates. After a cluster is formed, a smaller cluster could grow on top,
and than on top of that, until the surface becomes very rough. In this case, the
fundamental equation describing the growth mode is:

$$\frac{d\theta_n}{dt} = (1/\tau)(\theta_{n-1} - \theta_n) \tag{1.31}$$

$$\theta_0 = 1 \tag{1.32}$$

$$\theta_n(0) = 0 \tag{1.33}$$

Here, $\theta_{n-1} - \theta_n$ is the fraction of the area of the nth layer that is unfilled. This is a
birth-death model, since the growth on an unfilled layer is rapid, while the growth
of a nearly completed layer is slow. These equation can be solved in:

$$\theta_n(t) = 1 - e^{-t/\tau} \sum_{j=0}^{n-1} \frac{(t/\tau)^j}{j!} \tag{1.34}$$

In this model, where there is no inducement for layers to fill in, the surface becomes
progressively rougher with $rms = \sqrt{t/\tau}$, as can be seen by the following figure.
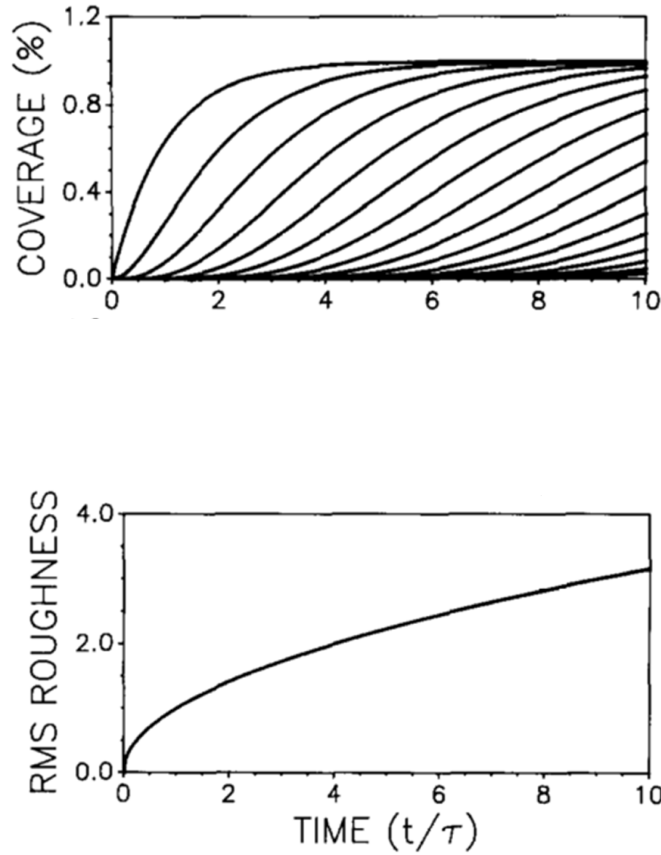
Figure 1.9: The coverages and rms roughness evolution with time corresponding to a non diffusive growth.

1.3.5   Diffusive growth model

Adding the possibility that an atom can jump to a lower level gives models intermediate between perfect layer by layer growth and non diffusive growth. Schematically the differential equation would be:

$$\frac{d\theta_n}{dt} = (1/\tau)(\theta_{n-1} - \theta_n) + jumps \; (n+1 \to n) - jumps \; (n \to n-1) \quad (1.35)$$

A variety of models could be used for the last two terms. In keeping with the birth-death approach, **we assume a jump rate in going from, for example, $n+1$ to n, that is proportional to the product of the available space on level n and the uncovered area on the level $n+1$.** The reasoning is that once an atom is covered it is not able to diffuse to an edge. Then eq. 1.3.5 becomes

$$\frac{d\theta_n}{dt} = (1/\tau)(\theta_{n-1}-\theta_n)+k(\theta_{n+1}-\theta_{n+2})(\theta_{n-1}-\theta_n)-k(\theta_n-\theta_{n+1})(\theta_{n-2}-\theta_{n-1}) \quad (1.36)$$

k is the only parameter of the model. The coverages and rms roughness can be evaluated numerically, subject to conditions $\theta_0 = 1$, $\theta_n = 0$ and $\theta_\infty = 0$. The results have a typical form like in Figure 1.3.5.
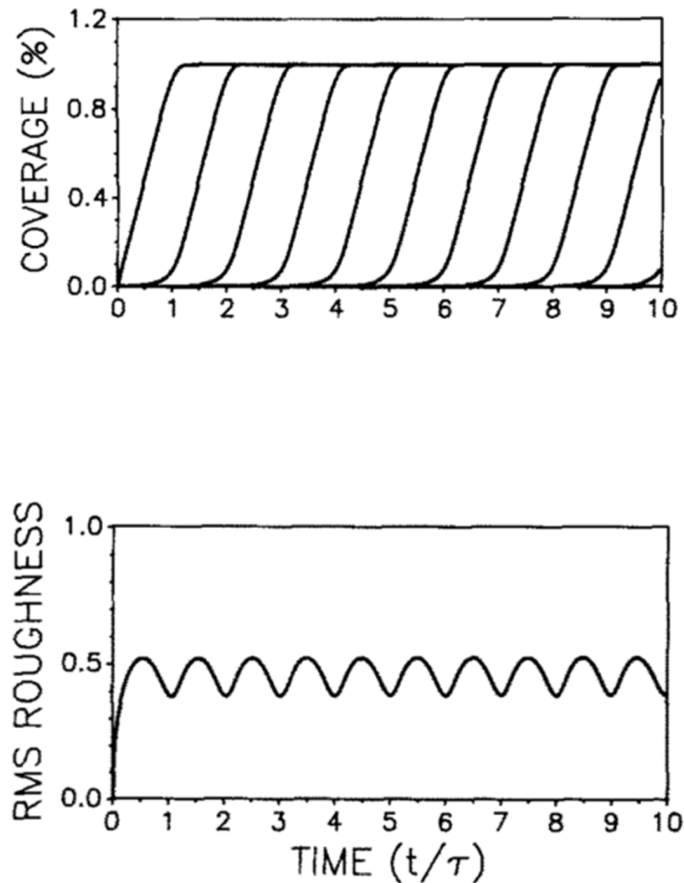

Figure 1.10: The coverages and rms roughness evolution with time corresponding to a diffusive growth.

1.3.6   Distributed growth model (DGM)

In a second model for treating the transfer between layers, we explicitly take into account the lateral structure in the plane by distributing adatoms among the layers according to the number of reactive sites available, which means the free perimeter. **Of the $(\theta_n - \theta_{n+1})/\tau$ atoms per unit time arriving on the top of the nth layer, a fraction α_n transfer to the nth layer and a fraction $1 - \alpha_n$ remains on top of the nth layer.**
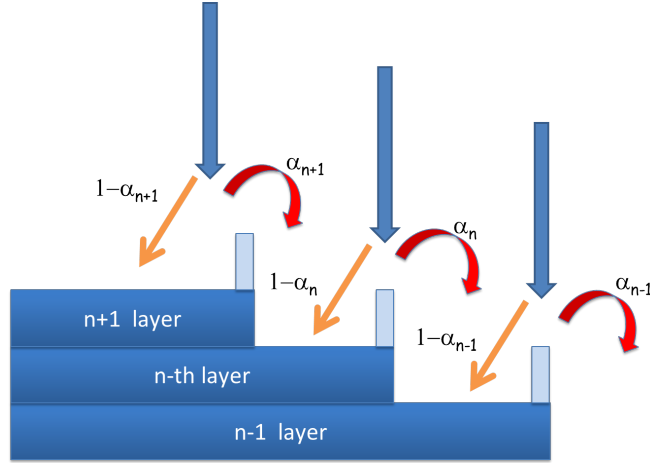
Figure 1.11: Picture of the molecules fractions of the incident flux reaching the $(n+1)th$ layer, the nth and the $(n-1)th$. The step-barriers depict the Ehrlich-Schwoebel barrier of each layer.

Eq.1.3.5 then becomes the set of coupled differential equations

$$\frac{d\theta_n}{dt} = (1/\tau)(\theta_{n-1} - \theta_n) + \frac{\alpha_n}{\tau}(\theta_n - \theta_{n+1}) - \frac{\alpha_{n-1}}{\tau}(\theta_{n-1} - \theta_n) \qquad (1.37)$$

subject to the initial conditions $\theta_0 = 1$, $\theta_n = 0$ and $\theta_\infty = 0$.

These equations become non linear when we put the physics into the dependence of the α_n on coverages. A difference between this model and the diffusive one, is in the number of layers that are in direct communication. For the diffusive model it is five layers, whereas here it is just three.

Let us assume that the distribution of the incoming adatoms is according to the number of reactive sites, such as step sites or cluster edges. Let $d_n(\theta_n)$ be the perimeter of the nth layer and

$$\alpha_n = A_n \frac{d_n(\theta_n)}{d_n(\theta_n) + d_{n+1}(\theta_{n+1})} \qquad (1.38)$$

where $\alpha_n = 0$ if $d_n = 0$, even if $d_{n+1} = 0$. A_n and d_n are the free parameters of this model. If $A = 1$ this model gives a perfect layer by layer growth and if $A = 0$ it gives non diffusive growth. In this mean field approach there is considerable flexibility in the model depending upon how the perimeter is related to the coverage.

Assuming that for a less than half filled surface there is a fixed number of cluster, each with the same perimeter, and that for a more than half filled surface there is a

fixed number of holes, each with the same perimeter, we could generally choose:

$$
d_n = \begin{cases} \theta_n^{p_1} & \theta_n < \theta_c \\ (1 - \theta_n)^{p_2} & \theta_n > \theta_c \end{cases}
$$

with

$$
\theta_c^{p_1} = (1 - \theta_c)^{p_2} \tag{1.39}
$$

as a matter of continuity, being θ_c the critical coverage at which coalescence happens.

The choice $p_1 = 1$ corresponds to the maintenance of cluster size while the number increases, as illustrated in Figure 1.12
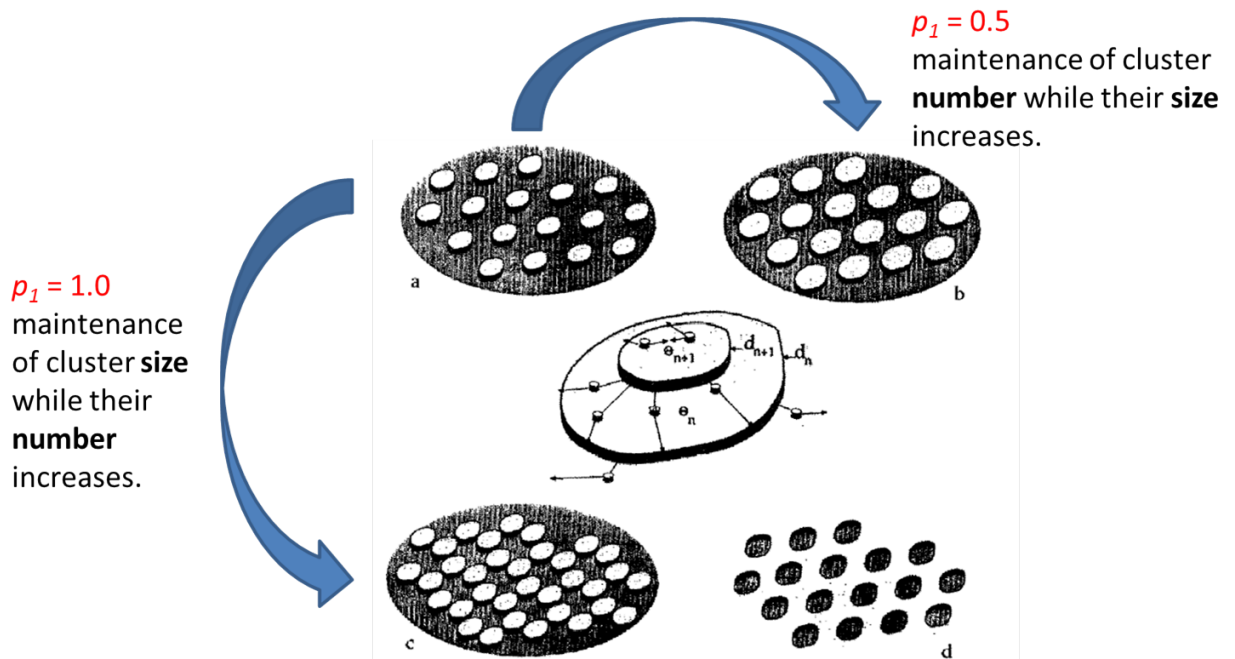

Figure 1.12: Schematic of the ideas underlying the distributed growth model. The growth between panels a and b assumes no additional nucleation. The growth between panels a and c assumes nucleation but no change in size. Panel d represents the holes in an almost filled layer.

1.4   Roughening transition and Ehrlich-Schwoebel barrier

What happens if an atom diffuses on an island and approaches its edge from above? The answer is that there is an additional potential barrier at the edge of the island that the atom must pass to jump off. This barrier results in a probability of the atom to be reflected that is higher than the one for it to jump down.

The microscopic origin of this energy barrier can be understood referring to Figure 1.13. For this we count the existing bonds an atom has before it jumps off. The dotted atom in Figure 1.13 must break its bond with the atom on its left before jumping down the step, but there is no atom on its right to help the diffusion process in that direction. The resulting asymmetry in the lattice potential generates a higher probability of moving to the left (being reflected) than to the right.
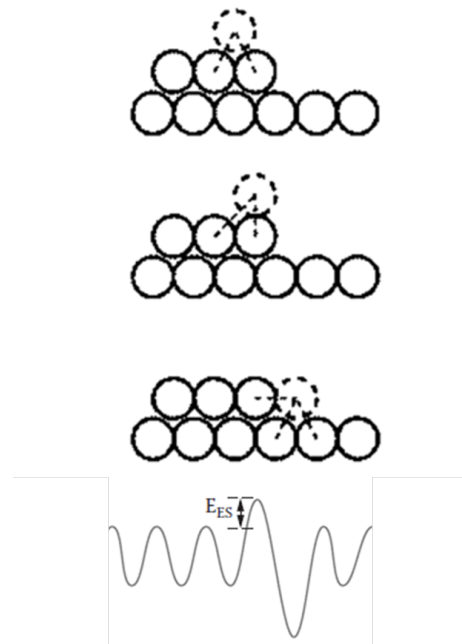
Figure 1.13: Cross-section of a monoatomic step in a surface and the lattice potential associated with the diffusion of an atom over the step. Diffusing to the right, in the intermediate position the atom has two bonds, but there is a missing bond to the right. The absence of this bond generates a further increase in the lattice potential, as shown in (d). In position (c) the atom forms three bonds with the neighbors, corresponding to a deep minimum in the lattice potential.

The difference between the step edge barrier and the diffusion energy E_{dif} is nowadays called **the Ehrlich-Schwoebel barrier** ([3,4]), and like in inorganic epitaxy it is considered the reason for mound formation in organic thin films.

Several methods have been found to estimate this barrier ([15,16]), among them we will follow ([16]): here, the Distributed Growth Model (see Section 1.3.6) is used to simulate the growth dynamics of the thin film. From this simulation, with a best fit of the rms evolution $vs.$ time, the probabilities of jump from the $(n+1)th$ to the nth layer are obtained. Since in our in-situ real time experiment we are in front of a 2D+3D growth with a roughening transition at the third layer, then the idea is to make the following guess for the probability p_3 of jump from the top of the third layer to third layer itself, $p_3 \sim exp(-E_{ES}/kT)$. From here the energy barrier E_{ES} can be obtained.

1.5 Issues specific to organic thin film growth

While the considerations presented above apply to inorganic as well as organic thin film systems, there are a few issues specific to organics, which can lead to quantitatively and qualitatively different growth behaviour.

- **Organic molecules are extended objects and thus have internal degrees of freedom**
  (i) The orientational degrees of freedom which are not included in conventional growth models can give rise to new phenomena, such as the change of the molecular orientation during film growth. Also, even without considering a transition during the growth, the distinction of lying-down and standing-up films is only possible for molecular systems.
  (ii) The vibrational degrees of freedom can have an impact on the interaction with the surface as well as the diffusion behaviour.

- The interaction potential (molecule-molecule and molecule-substrate) is generally different from the case of atomic adsorbates, and van der Waals interactions are more important
  (i) The response to strain is generally different. Potentially, more strain can be accommodated and in those systems, where the build up of strain leads to a critical thickness (before the growth mode change), this thickness can be greater for softer materials. The different softer interactions with the substrate and the corrugation of the potential have also been discussed in terms of 'van der Waals epitaxy' and 'quasi-epitaxy'.

- The size of the molecules and the associated unit cells are greater then that of typical inorganic substrates

  (i) The effective lateral variation of the potential is smeared out, i.e. averaged over the size of the molecule, making the effective corrugation of the substrate as experienced by the molecule generally weaker than for the atomic adsorbates.

Generally, most of the above points directly or indirectly impact the interactions and thus also the barriers experienced during diffusion. Thus, not only the static structure, but also the growth dynamics exhibit differences compared to inorganic systems.

1.6   Bibliography

[1] I. V. Markov. *Crystal growth for beginners.* World Scientific (2003)

[2] J. A. Venables. *Introduction to Surface and Thin Film Processes.* Cambridge University Press (2000)

[3] G. Ehrlich. *The Journal of Chemical Physics*, **44**, 1039 (1966)

[4] R. L. Schwoebel. *Journal of Applied Physics*, **37**, 3682 (1966)

[5] A.-L. Barabasi and H. E. Stanley. *Fractal Concepts In Surface Growth.* Cambridge University Press (1995)

[6] R. W. Balluffi, S. Allen and W. C. Carter. *Kinetics of Materials.* Wiley (2005)

[7] S. Verlaak, S. Steudel, P. Heremans, D. Janssen and M. Deleuze. *Physical Review B*, **68**, 195409 (2003)

[8] H. Sitter, C. Draxl and M. Ramsey. *Small organic molecules on surfaces.* Springer (2013)

[9] J. Amar. *Physical Review B*, **50** (1994)

[10] R. Kariotis and M. G. Lagally. *Surf. Sci.*, **216**, 557 (1989)

[11] V. I. Trofimov, V. G. Mokerov and A. G. Shumyankov. *Thin Solid Film*, **306**, 105 (1997)

[12] I. Koponen. *Nucl. instrum. Methods Phys. Res. Sect. B*, **171**, 314 (2000)

[13] P. I. Cohen, G. S. Petrich, P. R. Pukite, G. J. Whaley and A. S. Arrott. *Surface Science*, **216**, 222 (1989)

[14] W. Braun, B. Jenichen, V. M. Kaganer, A. G. Shtukenberg, L. Daweritz and K. H. Ploog. *Surf. Sci.*, **525**, 126 (2003)

[15] C. Teichert, G. Hlawacek, A. Winkler, P. Puschnig and C. Draxl. **173**, 79 (2013)

[16] A. C. Mayer, R. Ruiz, H. Zhou, R. L. Headrick, A. Kazimirov and G. G. Malliaras. *Physical Review B*, **73**, 1 (2006)

Chapter 2

Atomic Force Microscopy

Atomic Force Microscopy (AFM) is a technique that allows us to see and measure surface structures with unprecedented resolution and accuracy. For example, arrangement of individual atoms in a sample or structures of individual molecules have been obtained by AFM ([1]). Very small images only 5 nm in size, showing only 40-50 individual atoms, can be collected to measure the crystallographic structure of materials, or images of 100 micrometers can be measured, showing the shape of tens of living cells at the same time ([2–4]). Because of this, since its invention in the 1980s AFM has come to be used in all fields of science such as chemistry, biology, physics, material science, nanotechnology and more.

An AFM is rather different from other microscopes, because it does not form an image by focusing light or electrons onto a surface, like an optical or electron microscope. An AFM physically feels the sample's surface with a sharp probe, building up a map of the height of the sample's surface.
It was not the first instrument to work in this way however. The predecessor of the AFM was the **stylus profiler**, which used a sharp tip on the end of a small bar, which was dragged along the sample surface. This profiler, for instance described by Shmalz in 1929, utilized an optical lever to monitor the motion of the sharp probe mounted at the end of a cantilever. A common problem with stylus profiler was the possible bending of the probe from collision with surface features leading to probe damage or sample damage. This is why, in 1971, Young demonstrated a non-contact type of stylus profiler where the electron field emission current between a sharp metal probe and a conductive sample is very dependent on the probe-sample distance. The probe was mounted directly on a piezoelectric ceramic element which was used to move the probe in the vertical direction above the surface. An electronic feedback circuit was then used to drive the z-axis piezoelectric element and thus keep the probe-sample distance at a fixed value. Then, with the x and y piezos, the probe

was used to scan the surface in the horizontal dimensions. By monitoring the x-y and z position of the probe, a 3D image of the surface was constructed. The resolution of Young's stylus profiler was limited by the instrument's vibrations.

In 1981 Binnig and Rohrer, working at IBM, were able to improve the vibration isolation of an instrument similar to Young's stylus profiler such that they were able to monitor electron tunneling instead of field emission between the tip and the sample. This instrument was the first **scanning tunneling microscopy (STM)** ([5–7]). The reason the STM was much more successful than the stylus profiler is that electron tunneling is much more sensitive to tip-sample distance than field emission, so the probe could be scanned very close to the surface. The results of these early experiments were astonishing; Binnig and Rohrer were able to see individual silicon atoms on a surface. Without the STM, attaining this kind of resolution required a transmission electron microscope (TEM), which weighs thousands of kilograms and fills a room. For the STM invention Binnig and Rohrer later shared the Nobel Prize for physics in 1986. Although the STM was considered a fundamental advancement for scientific research, it had limited applications, because it worked only on electrically conductive samples. This immediately led the inventors to think about an instrument that would be able to image not only metals and semiconductors, but also insulating samples. In 1986 Binnig, Quate and Gerber published a paper entitled "**Atomic Force Microscope**" ([8]).
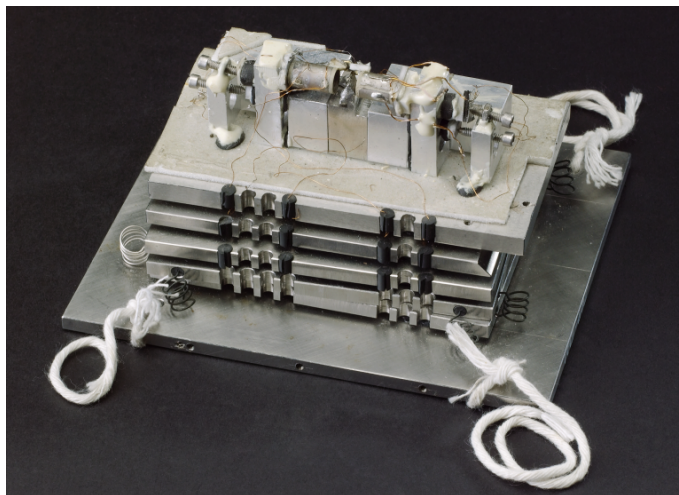

Figure 2.1: The first AFM instrument built by Binnig, Quate and Gerber in the Science Museum, London.

2.1 AFM instrumentation

We can draw the general design of an AFM like in Figure 2.2. Its working principle can be explained as follow: the force transducer measures the force between the probe and surface; the feedback controller keeps the force constant by controlling the expansion of the z piezoelectric transducer. Maintaining the tip-sample force at a set value effectively also maintains the tip-sample distance fixed. Then, the x-y piezoelectric elements are used to scan the probe across the surface in a raster-like pattern. **The amount the z piezoelectric moves up and down to maintain the tip-sample distance fixed is equal to the height topography, previous calibration of the piezo**. In this way, by monitoring the voltage applied to the z piezo, a map of the surface shape, a height image, is measured.
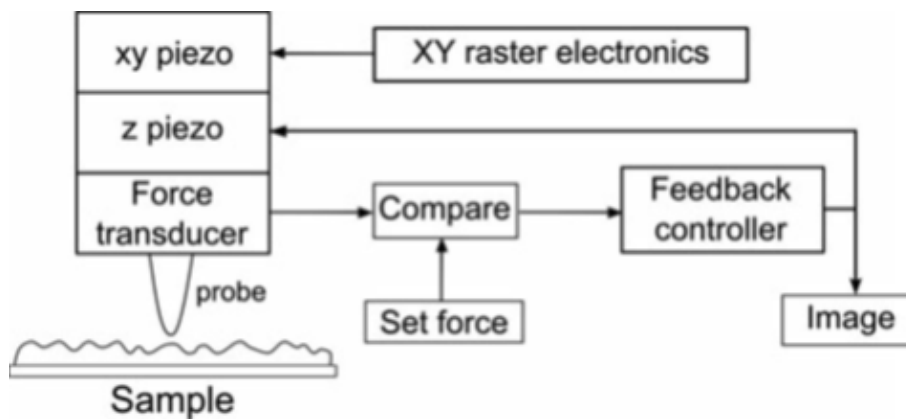
Figure 2.2: General AFM block diagram.

To be more detailed and better understand the working principle of an AFM, let's start from its main components which are **the microscope stage, the control electronics and a computer**.

- The microscope stage contains the x-y-z piezoelectric scanners (the mechanism for moving the AFM tip relative to the sample in the x-y-z directions), a coarse approach mechanism which can move the AFM scanner towards the sample, the sample holder and a force sensor, to hold and monitor the AFM tip. Often, there is an x-y positioning stage which is useful for positioning the feature for

imaging under the probe and the stage is supported on a vibration isolation platform to reduce noise.

- The control electronics usually takes the form of a large box interfaced to both the microscope stage and the computer. The electronics are used to generate the signals used to drive the scanner and any other motorized components in the microscope stage. They also digitize the signals coming from the AFM so that they can be displayed and recorded by the computer. The feedback between the signals coming out and going back into the AFM stage is handled by the control electronics, according to parameters set via the computer.

- Software in the computer is used by the operator to acquire and display AFM images, in our case we used the **software Matrix** ([9]) by Omicron. The user operates the software program, and the relevant acquisition parameters are passed onto the control electronics box. The computer usually also contains a separate program to process and analyse the images obtained, in our case **Gwyddion** 2.37 ([10]), see Section 2.6.

2.1.1 The AFM stage

x-y-z scanners: Piezoelectric materials are electromechanical transducers that convert electrical potential into mechanical motion. In other application they can also be used in the opposite sense. Typically, the expansion coefficient for a single piezoelectric device is on the order of 0.1 nm/V. Thus, if the voltage used to excite the piezomaterial is 2 volts, then the material will expand approximately 0.2nm, which is approximately the diameter of a single atom. It is the ability to accurately control such tiny movement that makes piezoelectric materials so useful for AFM. Indeed, they are used to control the motion of the probe as it is scanned across the sample surface.

The most common types of piezoelectric materials in use for AFM scanners are amorphous lead barium titanate or lead zirconate titanate. These ceramics may be hard or soft; this affects how much they can expand, versus the applied voltage, as well as the linearity of the relationship between applied voltage and expansion. Hard ceramics have smaller coefficients of expansion, but are more linear. Soft ceramics have more non-linearities and have greater expansion coefficients. After fabrication, piezoelectric ceramics are polarized. Polarization can be lost by elevating the piezos to a temperature above their critical temperature or by applying too high voltage. Electronically, piezos act as capacitors and store charges on their surfaces. Capacitances of ceramics may be as large as 100 microfarads. The piezoelectric ceramic

changes geometry such that the volume is preserved during extension (due to mass conservation). One possible configuration is a disk which gets longer and narrower when a voltage is applied. Another one is a tube, with electrodes on the inside and outside. This configuration gives a lot of motion and is very rigid. Currently, the tube scanner is the most widely used: it is very compact, allows very precise movements especially at small scan ranges. It is also particularly convenient to engineer an AFM with a tube scanner because there is a clear optical path down the centre of the tube (like in the VT SPM microscope, see Chapter 5).
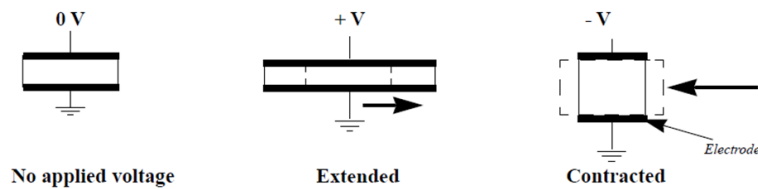
Figure 2.3: Graphical explanation of the working principle of a piezoelectric scanner.
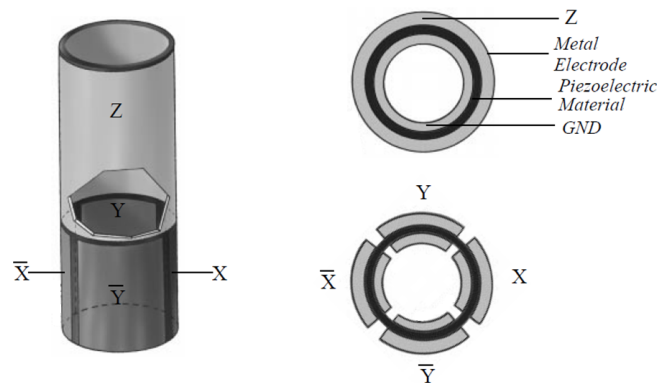
Figure 2.4: Configuration of a common AFM tube scanner.

Ideally, the piezoelectric ceramics would expand and contract in direct proportion to the driving voltage. Unfortunately, this is not the case, and all piezoelectric materials show non linear behaviour. They show two primary non-ideal behaviours: **hysteresis and creep**. Hysteresis, derived from the word history, causes the ceramic to tend to maintain the shape that it was in previously. As the ceramic is

expanding, there is a negative shaped non-linearity, and as the material is contracting, there is a positive shaped non-linearity. Hysteresis causes a bending distortion in the images obtained, unless corrected. Creep occurs when the ceramic is subjected to a sudden impulse such as a voltage step function, continuing to move in the same direction as the offset, even after the voltage has stopped changing.
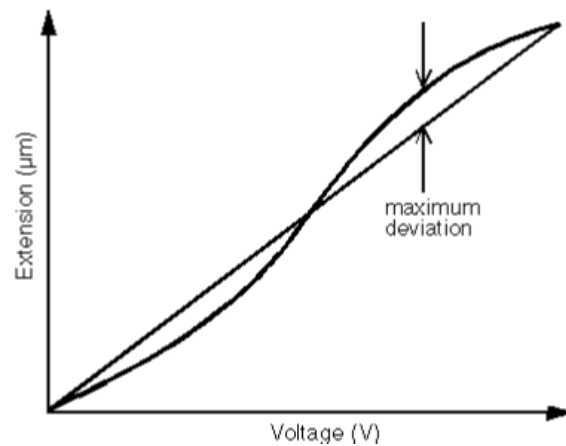

Figure 2.5: Intrinsic non linearity of a scanner.

Correcting the non-ideal behaviours of piezoelectric ceramics is essential to make accurate AFM images. Due to the different ways the axes are operated- x and y in a raster pattern, z moved by the feedback control- the required corrections are different for the x-y axes and the z axis. Also, hysteresis and creep make it difficult to scan the AFM very quickly, and maintain accuracy.

Coarse approach mechanism: An important challenge in AFM design is making a motion control system that permits the approach of the probe to the surface before scanning. This must be done such that the probe does not crash into the surface and break. The problem is analogous to fly from the earth to the moon in 60 seconds and stop 38 meters from the surface without overshooting or crashing.

In the AFM stage there are two separate motion generation mechanism in the z axis: the first is a stepper-motor-drive mechanism with a dynamic range of a centimeter and a resolution of a few microns. The stepper motor is typically driven by an 80 turn per inch screw which can be attached to a motor to get an automated first-motion. The second motion generation mechanism is the already seen z piezoelectric element which has a dynamic range of about 10 microns or less and a resolution of less than 0.5 nm. While stepper motors have the range and speed to

approach the surface from a great distance in a short time, they have neither the resolution nor fast response time to put the tip into feedback safely. On the other hand, the piezo driver is sensitive enough to safely go into feedback, but can only move short distances.
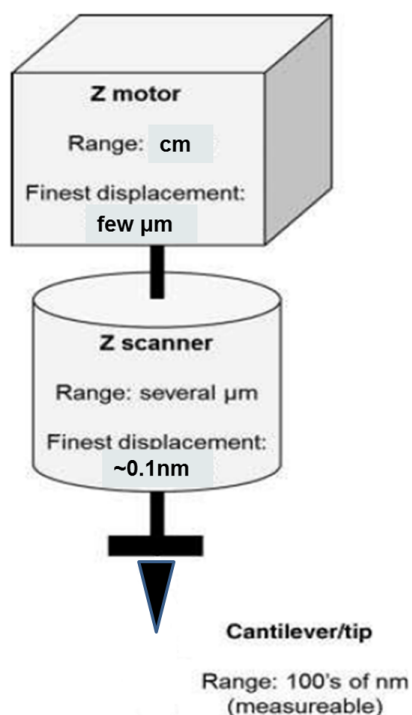
Figure 2.6: Serie relationship between z motor, z scanner and the cantilever/tip system.

Typically, probe approach is achieved with a woodpecker method (shown in Figure 2.7). In this method, the stepper motor is stepped a small increment, say 1 micron. Then the z piezo is extended 5 microns, of its maximum extension, to see if the surface is detected. The z piezo is then retracted, the stepper motor extends one more micron, so on and so on. A key component here is that when the probe encounters the surface, the feedback is turned on immediately. In this way, the AFM can approach the surface from several hundreds of microns, without risk of crashing the tip.
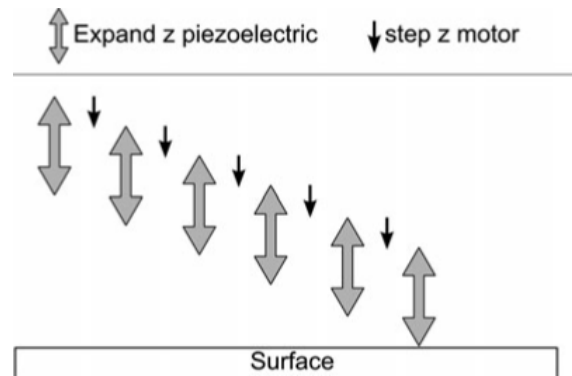
Figure 2.7: Woodpecker probe approach method.

Force sensor: The force between an AFM probe and a surface is measured with a force transducer. They may be constructed that measure forces as low as 10pN, this is a typical order of magnitude of forces occurring between tip and sample, but, another reason for being able to detect such small forces is to protect the tip. If we calculate, indeed, the pressure acting on the tip as the ratio of force by area, being the contact area of some nm^2, the force must be small enough to obtain reasonable pressures.

With the advent of microfabricated cantilevers the optical lever AFM has become the most widely used design for the force sensor in an AFM. The principle of the optical lever is shown in Figure 2.8.
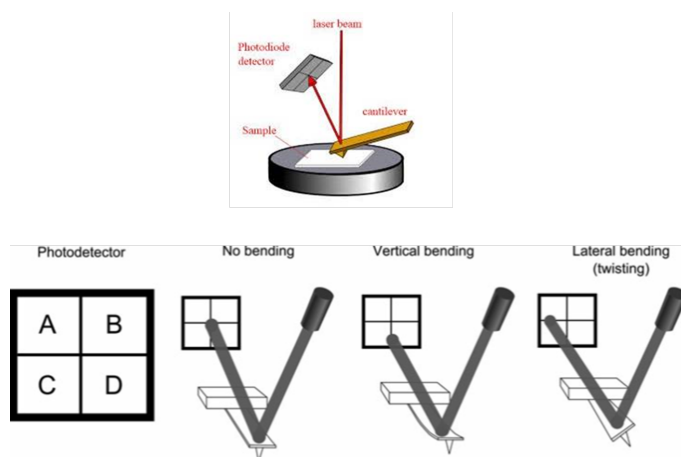
Figure 2.8: The optical lever sensor and an illustration of how the photodetector detects vertical and horizontal bending of the cantilever.

The lever consists of a laser focused to a spot on the back of a reflective cantilever; the beam is then reflected onto a split photodetector, which measures the position of the laser spot. The optical lever magnifies a small movement of the cantilever, to create a large movement at the photodiode. The chief advantage of this system is that it is highly sensitive to very small movements of the cantilever and it is quite simple to build. The design of an optical lever AFM sensor has a laser beam reflected by the back side of a reflective cantilever onto a four-segment photodetector. If a probe, mounted on the front side of the cantilever interacts with the surface, the reflected light path will change. The force is then measured by monitoring the change in light detected by the four quadrants of the photodetector. Specifically, the difference in signal between the top two and bottom two segments, i.e. (A+B)-(C+D) gives the vertical deflection (measured in volts or amps) and the difference between the rightmost two segments and the leftmost two segments gives the lateral deflection, i.e. (B+D)-(A+C).

The optical lever AFM force sensor requires alignment each time the probe is changed. Typically, alignment is accomplished by first positioning the laser beam onto the cantilever, and then confirming that the light is reflected onto the centre of the photodetector by looking at the photodetector signal.
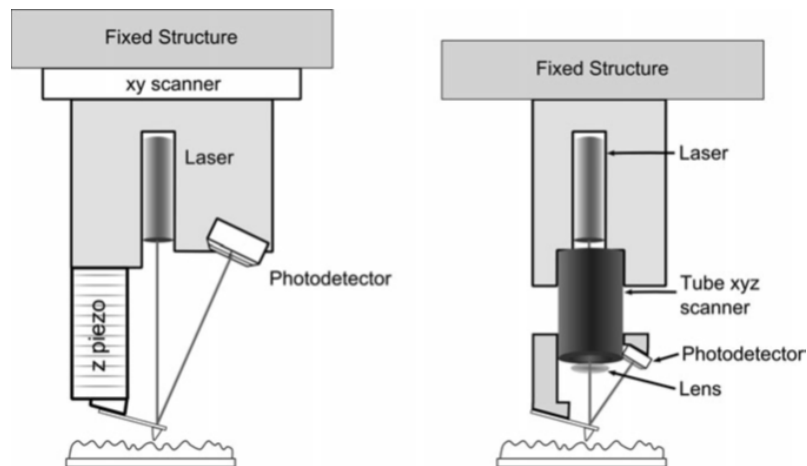

Figure 2.9: Designs for AFM with optical lever sensor. Left: the laser is scanned with the cantilever. Right: the laser is fixed and the cantilever is scanned, a lens keeps the laser light focused on the cantilever.

2.1.2   AFM electronics

x-y rastern pattern: The AFM electronics drive the x-y scanners in a type of raster pattern, as shown in Figure 2.10. The x scanner moves across the first line of the scan and back. It then steps in the y direction to the second scan line, moves across it and back, then to the third line, and so forth. AFM data are collected in only one direction - commonly called the fast scan direction - to minimize line to line registration errors that result from scanner hysteresis. The y direction is called the slow scan direction. While the x scanner is moving across a scan line, the image data are sampled digitally at equally spaced intervals. The spacing between the data points is called the step size. The step size is determined by the full scan size and the number of data points per line (pixels). The number of lines in a data set usually equals the number of points per line. Thus, the ideal data set is comprised of a square grid of measurements.
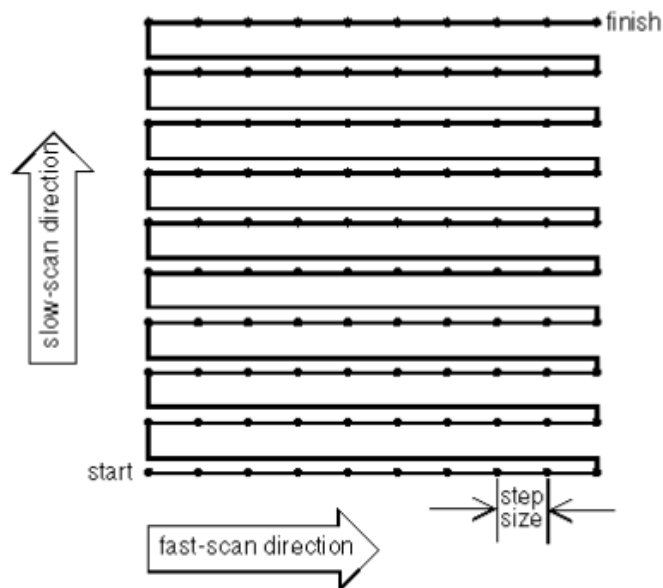
Figure 2.10: x-y scanners motion during data acquisition.

Feedback control: The reason an AFM is very sensitive is that feedback control is used to maintain a set force between the probe and the sample. The control electronics take the signal from the force transducers, and use it to drive the piezo-electrics so as to maintain the probe-sample distance, and thus the interaction force at a set level. For instance, if the probe registers an increase in force, because while scanning the tip encounters a particle on the surface, the feedback control causes

the piezoelectrics to move the probe away from the surface. Conversely, if the force transducers registers a decrease in force, the probe is moved towards the surface. The type of feedback control used in AFM is called a proportional-integral-derivative controller (PID).

2.1.3 AFM cantilever and tip

Cantilevers with a probe at their ends are considered disposable component of the AFM. In principle, an AFM probe should last forever; however, in practice the probe tip is often blunted when it touches a surface. The geometry of the probe is critical to the quality of images measured with an AFM. All AFM images are a convolution of probe geometry and surface. As an example, in Figure 2.11, if the probe cannot reach the bottom of a surface pit, or track the sides of a particle, the image will not indicate the correct geometry of the sample.

In order to make handling simple, the cantilevers are attached to a chip (or substrate). By industry convention, these are normally 3.5 x 1.6 mm in size, and about 0.5 mm thick. Figure 2.12 shows a cartoon of the design of a typical chip/cantilever/probe system.
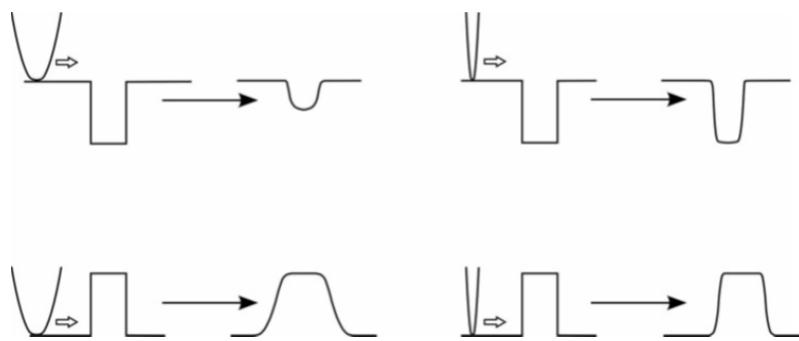
Figure 2.11: Comparison of image profiles obtained with a dull (left) or sharp (right) probe on a concave feature (a pit) or a convex feature (a step).

AFM requires not only sharp tips, but also cantilevers with optimized spring constant - lower than the spring constants between atoms in a solid, which are on the order of 10N/m. The spring constant of a cantilever depends on its shape, its dimension and the material from which it is fabricated. The cantilevers are small, generally between 50 and 300 microns long, 20-60 microns wide, and between 0.2 and 1 micron thick. V-shaped and rectangular shaped cantilevers are the two typical

cantilever's geometries.
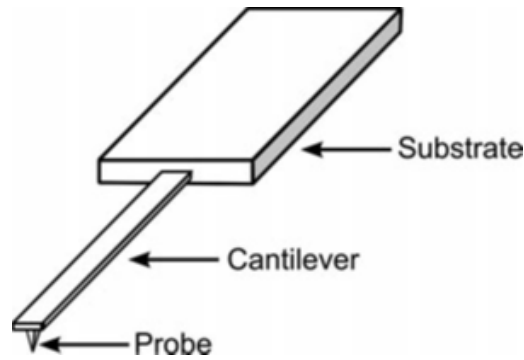
Figure 2.12: Chip/cantilever/probe system.

Thicker and shorter cantilevers tend to be stiffer and have higher resonance frequency, indeed for a rectangular cantilever, for example, it can be calculated the spring constant to be $k = Ewt^3/4L^3$, where E is the Young modulus of the cantilever's material and w, t and L are the width, thickness and length of the cantilever, respectively.

AFM manufacturers offer microfabricated tips in three geometries: pyramidal, tetrahedral and conical. Conical tips can be made sharp, with high aspect ratios (the ratio of tip length to tip width). Pyramidal tips have lower aspect ratios but they are more durable. AFM tips are fabricated from silicon (Si) or silicon nitride (Si_3N_4). The fabrication process is different for the two materials. Silicon conical tips are made by etching into the silicon around a silicon dioxide cap.
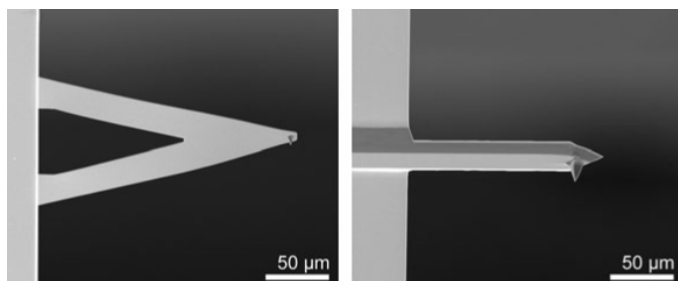
Figure 2.13: Examples of cantilever's shapes: V-shaped and rectangular ones

The high aspect ratio of conical tips makes them suitable for imaging deep, narrow features but they may break more easily than the pyramidal or tetrahedral geometries. Silicon also has the advantage that it can be doped, so that tips can be made electrically conducting. Silicon nitride tips are fabricated by depositing a layer of silicon nitride over an etched pit in a crystalline silicon surface, as illustrated in Figure 2.14. This method produces the pyramidal or thetrahedral tip geometry. The tips are broader than conical silicon tips making them less suitable for imaging deep features. On the other hand, silicon nitride is a harder material than silicon, which also makes silicon nitride tips more durable than silicon tips.
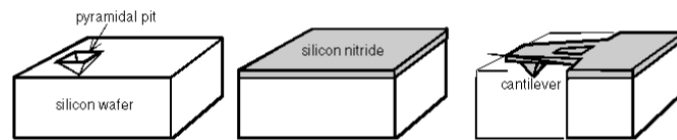
Figure 2.14: Fabrication procedure of a silicon nitride tip.

	tip geometry	structure	aspect-ratio	resonance frequency	cantilever lenght	AFM mode
Si_3N_4	pyramidal tetrahedral	durable	low	low	long	CM
Si	conical	brittle	high	high	short	oscillating mode

In Figure 2.15 one can find a typical datasheet of a NT-MDT ([11]) semicontact/non-contact probe.
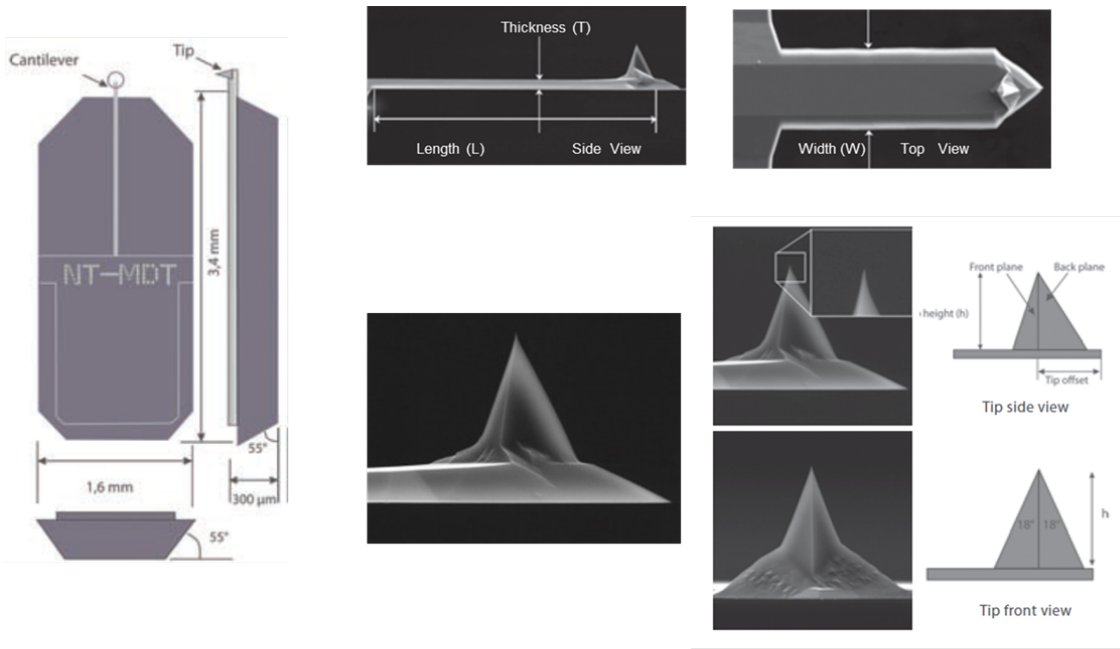
Cantilever specification

Cantilever leight, L±10 µm	Cantilever width, L±5 µm	Cantilever thickness, L±0.5 µm	Resonant frequency, kHz			Force constant, N/m		
			min	typical	max	min	typical	max
125	30	2.0	87	150	230	1.45	5.1	15.1

Tip specification

Tip shape	tetrahedral, the last 500 nm from tip apex is cylindrical
Tip height	14 – 16 µm
Curvature radius	typical 6 nm, guaranteed 10 nm
Tip offset	5 - 20 µm
Tip aspect ratio	3:1 – 7:1
Front plane angle	10°± 2°
Back plane angle	30°± 2°
Side angle (half)	18°± 2°
Cone angle at the apex	7° - 10°

Figure 2.15: NT-MDT typical probe with datasheet

2.2   Interactions in AFM

Of the four fundamental forces in nature, the electromagnetic interaction is the one most contributing to the deflection of an AFM cantilever, specifically, it is the so called **van der Waals force**, a term which, incidentally, applies to any dipole-dipole interaction: dispersion or London forces, Keesom forces and Debye forces. London forces regard fluctuating dipoles and is the type of van der Waals force which we will refer to, the second is an interaction between permanent dipoles (such as the molecule CO) and Debye forces refer to dipoles induced by other atoms or molecules that are charged or permanent dipoles. In the case of London forces, upon bringing together two perfectly inert, spherical atoms, fluctuating electronic charge distribution (i.e. instantaneous dipole moments) begin to exhibit correlations in their orientations. The electron of one atom tend to repel the nearest electrons of the other atom such that at any instant, a net dipole, on one atom induces a net dipole on the other atom and vice versa. Averaged over time, there is a nonvanishing correlation in the orientations of these dipoles. These correlating dipoles tend to attract each other with a force that falls off as distance to the seventh power (which means a sixth power in the potential). In order to complete the description of London forces we have to think about what is contact at the atomic level. As is well known, if we continue to push two atoms together, quantum mechanics ultimately would resist the process due to the Pauli exclusion principle. A more common and practical representation of this repulsive force gives a decrease with distance to the thirteenth power (a twelfth power in the potential), which, once added to the attractive London force described before, brings us to the so called **Lennard-Jones potential** or "6-12" potential, see Figure 2.16.

$$V_{LJ}(r) = \epsilon[(\frac{\sigma}{r})^6 + (\frac{\sigma}{r})^{12}] \tag{2.1}$$

where ϵ is basically the depth of the potential well and σ is the finite distance at which the potential is zero.

Force microscopy experiments usually deal with ensembles of atoms or molecules. The net van der Waals force is the result of adding all the individual dipole interactions between the tip and surface atoms. One of the most common approximation to describe an AFM interface is the sphere-flat geometry. The tip-sample ensemble is simulated by a sphere (tip) and a flat sample. Several studies have shown that this geometry is a reasonable approximation to the tip-sample geometry. Long-range attractive forces, for distances larger than a_0 (the interatomic distance where second derivative of the potential changes sign), are derived from the non-retarded van
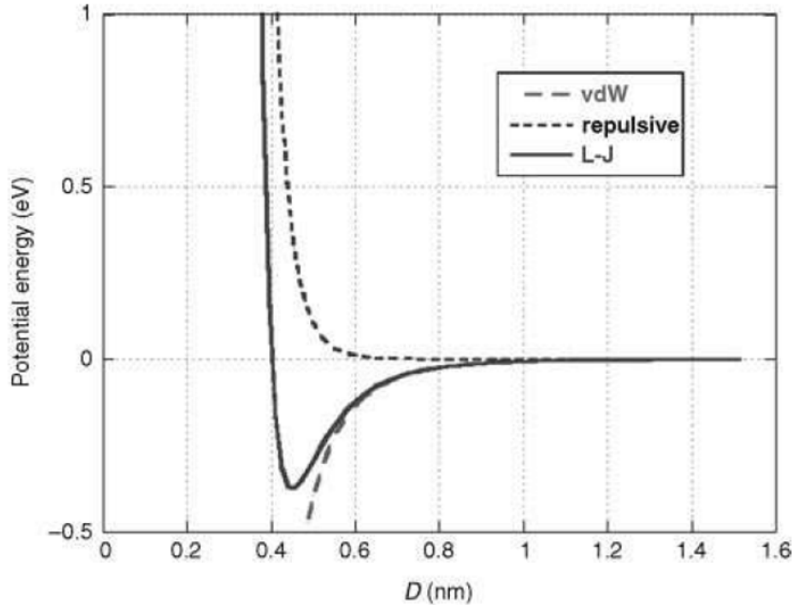
Figure 2.16: Distance dependence of Lennard-Jones potential.

der Waals energy for two atoms in vacuum. Assuming additivity, for a sphere-flat geometry the van der Waals force is ([12,13]):

$$F_{ts}(z_c, z) = -\frac{HR}{6(z_c + z)^2} \tag{2.2}$$

where H is the Hamaker constant and R the tip radius. For convenience, the tip-sample instantaneous separation D is calculated as the sum of the tip-sample rest distance, z_c, and the instantaneous tip position z ($d = z_c + z$). The origin of the z coordinate is the tip's rest position.

For distances smaller than a_0, instead, the repulsive force between the tip and the sample is simulated by the indentation force derived from Hertz's model ([12,13]):

$$F_{ts}(z_c, z) = -\frac{HR}{6a_0^2} + \frac{4E\sqrt{R}}{3 - 3\nu^2}(a_0 - z - z_c)^{3/2} \tag{2.3}$$

where E and ν are the Young's modulus and Poisson's coefficient of the sample, respectively.

2.3   AFM modes

The range of available AFM modes is at the heart of modern AFM and makes it a versatile, powerful tool. Initially the only mode available was contact mode and this limited the types of samples that could be examined. Now there are a very large

number of possible modes of operation of AFM. For example, in 1999, Friedbacher *et al.* attempted to list the names of all the SPM modes and arrived at more than 50 terms ([14]). In this section we will describe just the main topographics and non topographics ones.

A variety of topographic modes have developed with time, which can be divided into those modes which measure the static deflection of the AFM cantilever and those that measure the dynamic oscillation of the cantilever. The differences between the modes lead not only to different experimental procedures, but to differences in the information available and even to differences in the interpretation of the data.

AFM	SNOM
Contact mode	Aperture (ASNOM)
Non-contact mode (NC-AFM, close contact mode, FM-AFM)	Non-aperture SNOM (NA-SNOM)
	Evanescent field SNOM (EF-SNOM)
Intermittent Contact mode (IC-AFM, AM-AFM, Tapping)	Transmission SNOM (T-SNOM)
	Collection SNOM (C-SNOM)
Chemical Force Microscopy (CFM)	**STM**
Lateral Force (LFM, FFM))	Scanning Tunnelling Spectroscopy (STS)
Electric Force (EFM)	Topography (STM)
Force Spectroscopy	Alternating Current STM (AC-STM)
Nanoindentation	Ballistic electron emission microscopy (BEEM)
Magnetic Force (MFM)	Scanning Tunnelling Optical Microscopy (STOM)
Kelvin Probe (KPM, SKPM)	
Scanning Thermal Microscopy (SThM)	
Nano oxidation Lithography	
Dip-pen Nanolithography (DPN)	

Figure 2.17: Summary of some SPM-based techniques.

2.3.1 Contact mode

Contact mode AFM was the first mode developed for AFM. It is the simplest mode conceptually, and was the basis for the development of the later modes. Contact mode is capable of obtaining very high resolution images. It is also the fastest of all the topographic modes, as the deflection of the cantilever leads directly to the topography of the sample, so no summing of oscillation measurements is required which can slow imaging.

In order to understand the way AFM modes work, it is necessary to use the so called force-distance curves. A carton of a simple force-distance curve is shown in Figure 2.18.
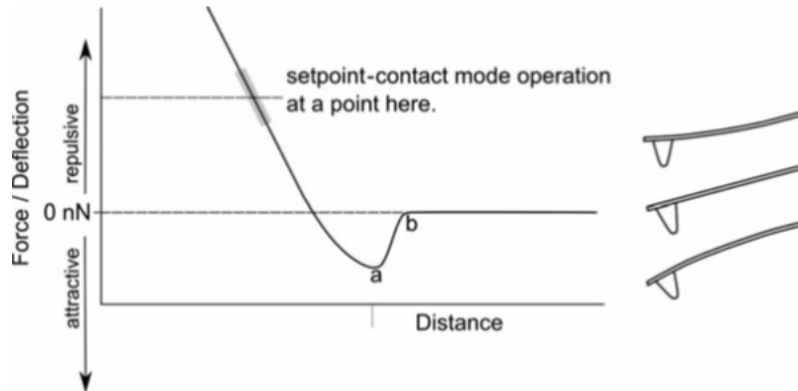
Figure 2.18: Simplified force-distance curve showing contact scanning regime (repulsive region). Right: illustration of probe bending in each regime: repulsive force regime, zero deflection regime and attractive force regime.

Such a curve is calculated from a deflection-distance curve which is easily measured by monitoring the deflection of the cantilever as the piezo is used to move the tip towards the sample. Considering the approach curve shown in Figure 2.18, when the tip is far from the sample surface, the cantilever is considered to have zero deflection; as the tip approaches the surface, it normally feels first an attractive force, and a snap in occurs, as the tip becomes unstable and jumps into contact with the surface. As the instrument continues to push the cantilever towards the surface, the interaction moves into the repulsive regime. It is within the repulsive regime that contact-mode imaging usually occurs, for example at the point labelled set-point in Figure 2.18. This has the following important implications: as a result of the repulsive force between the tip and the sample, the sample may be damaged, the tip could also be damaged and as the tip and sample are constantly in contact with each other as the tip moves along the sample, in addition to the normal force they apply to each other, lateral forces are experienced by both probe and sample.

The basis of contact-mode AFM is that the microscope feedback system acts to keep the cantilever deflection at a certain value determined by the instrument operator. This point is known as the set-point. The set-point is one of the important control parameters that the operator must adjust to optimize imaging.

The imaging mode described so far is known as **constant-force contact-mode AFM**. If the user turns off the feedback while imaging, then she is effectively using

constant-height contact-mode AFM. Because constant-force mode is by far the most widely used mode, in general any reference to contact-mode AFM will mean constant-force mode unless specified otherwise. **In constant-height mode, with no feedback active, the image signal comes entirely from cantilever deflection, rather than from the voltage applied to the z piezo** (which would be typically set at a constant value). Constant-height mode AFM does have some specific applications: it can be useful in conditions where scanning is carried out so fast that the feedback system cannot cope ([15]).
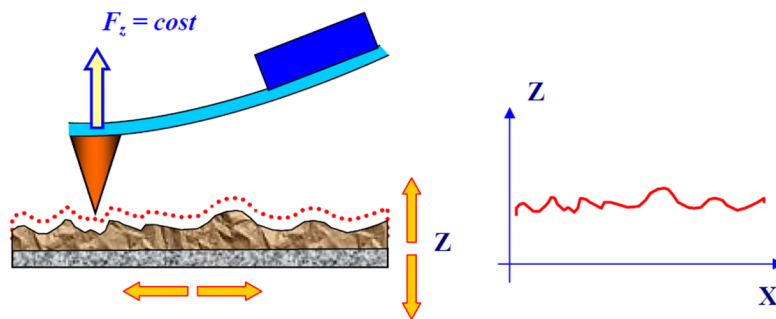

Figure 2.19: AFM image acquisition in constant force mode.
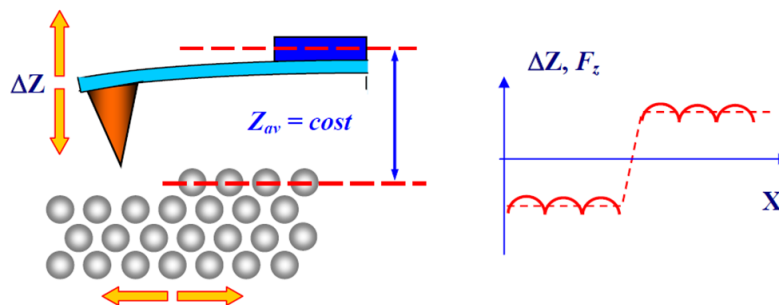
Figure 2.20: Scheme of constant height mode set up.

Contact mode AFM has a really wide range of potential applications. Probably the best reason to use it is its high resolution. Some dynamics modes can also

achieve extremely high resolution, but compared to, for example, tapping mode, the resolution of contact mode is potentially extremely high. **What keeps it from being used more widely is that the applied normal force leads to a high lateral force applied to the sample as well; this can lead to problems of sample distortion, damage, or even removal from the substrate. Moreover, in ambient conditions, a capillary layer of water will form between the tip and the surface. One effect of this is to strongly pull the AFM tip onto the surface**. In water these forces do not exist, so it is easier to image. For this reason, and due to some complications of imaging in dynamic modes in liquids, imaging in liquid is a strong point of contact mode.

Here we resume the main points of contact mode AFM:

- Contact mode AFM operates monitoring the change in cantilever deflection with a photodiode detector

- A feedback loop maintains a constant deflection between the cantilever and the sample by vertically moving the z scanner at each (x,y) data point to maintain a set-point deflection

- By maintaining a constant cantilever deflection, the force between the tip and the sample remains the same

- The force is calculated from Hooke's law: $F = -k*x$ where k is the spring constant and x the cantilever deflection

- Force constants usually range from 0.01 to 1.0 N/m, resulting in forces ranging from nN to μN in an ambient atmosphere

- The distance the z scanner moves vertically at each (x,y) data point is stored by the computer to form the topographic image of the sample surface

- Operation can take place in ambient and liquid environments

- High scan speeds

- Capable of obtaining very high resolution images

- Lateral (shear) forces can distort features in the image

- The forces normal to the tip-sample interaction can be high in air due to capillary forces from the adsorbed fluid (capillary) layer on the sample surface
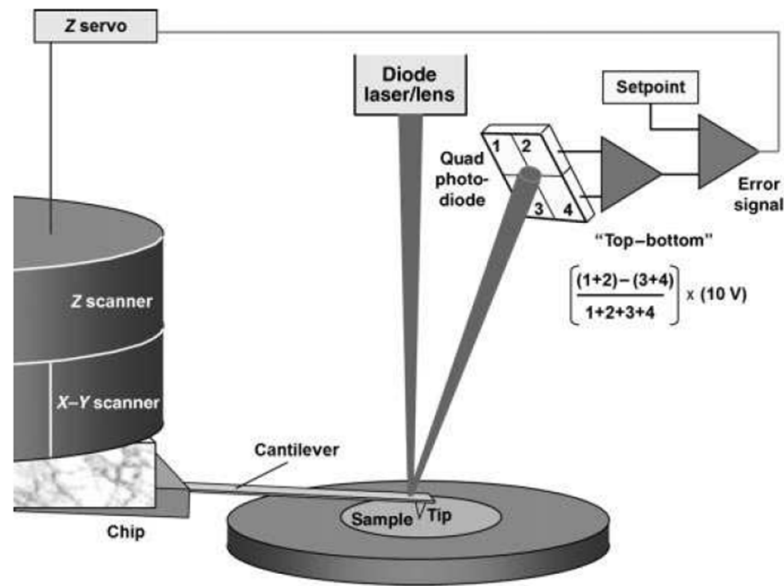
Figure 2.21: Scheme of contact mode AFM set up.

2.3.2   Oscillating modes

Oscillating or dynamic AFM methods offer three main advantages with respect to static (contact) AFM. First, the tip motion is sensitive to both forces and force gradients. Second, in contact AFM the tip sample interaction is measured following the cantilever's deflection. In dynamic AFM the oscillation amplitude, the frequency, and the phase shift, as well as the cantilever's deflection, may be recorded. This opens several channels for simultaneous data acquisition, each of them describing a different sample property. Third, dynamic AFM may substantially reduce the sample damage.

There are now a large number of dynamic modes of operation, and even more names for them. However, all of these modes are variations on a theme. The cantilever is oscillated, usually with an additional piezoelectric element, and typically at its resonant frequency. When the oscillating probe approaches the sample surface, the oscillation changes due to the interaction between the probe and the force field from the sample. The effect is a damping of the cantilever oscillation, which leads to a reduction in the frequency and amplitude of the oscillation. **The oscillation is monitored by the force transducer and the z scanner adjusts the z height via the feedback loop to maintain the probe at a fixed distance from the sample**, just as in contact mode AFM. The only real difference between the various oscillating modes available are in the amplitude of the oscillation applied to

the probe and the method used to detect the change in the oscillation. The choice of small or large amplitude has a considerable practical effect, as is illustrated in Figure 2.22. Using a small oscillation amplitude (denoted by the arrow A), it is possible to maintain the cantilever in the attractive regime only. This technique is sometimes known as **non-contact AFM**. This technique has some advantages due to the low tip-sample forces involved. On the other hand, it can be seen that if a large oscillation amplitude is applied, then the probe will move from being far from the surface where there is no tip-sample interaction, through the attractive regime, into the repulsive regime, and back, in each oscillation cycle (arrow B). This technique involves large tip-sample forces, so can be more destructive, but is easier to implement. This technique is known as **tapping mode AFM**.
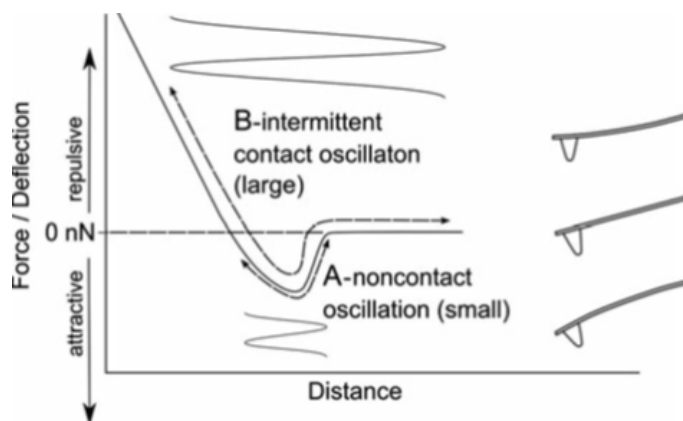
Figure 2.22: Different operating regimes for oscillating AFM modes. A: with a small amplitude of oscillation, the probe can be kept in the attractive regime (non contact mode). B: with a larger oscillation the probe moves through non-interacting, attractive and repulsive regimes, resulting in tapping mode.

Tapping mode

The fact that the tip-sample interaction moves through all three regimes has several important implications:

- there is tip-sample repulsive interaction leading to the possibility of sample or tip damage, however:

- due to the movement of the tip perpendicular to the surface, lateral forces are almost eliminated

- the tip passes through the contamination layer typically present in ambient conditions

The second and the third point above explain the popularity of tapping mode. The lateral forces which can cause great problems in contact mode AFM do not affect tapping mode. On the other hand, the fundamental instability of non-contact AFM in air (due to operation in the attractive regime and the presence of the capillary layer, see next section) is overcome. Moreover, since the equilibrium separation between tip and sample is smaller than the oscillation amplitude, the tip strikes the sample once each cycle. Large amplitudes, up to 100 nm, provide the cantilever with enough energy to overcome adhesion forces.

The operating principles of tapping mode can be described in the following way. The probe is oscillated with a large amplitude, typically in the range of 1-100 nm ([16]) and the feedback is usually based on amplitude signal. Often, in addition to the amplitude signal, the delay in the phase of the probe oscillation with respect to the drive signal is recorded. See subsection 2.4.1 for more detail.

The main points of tapping mode are:
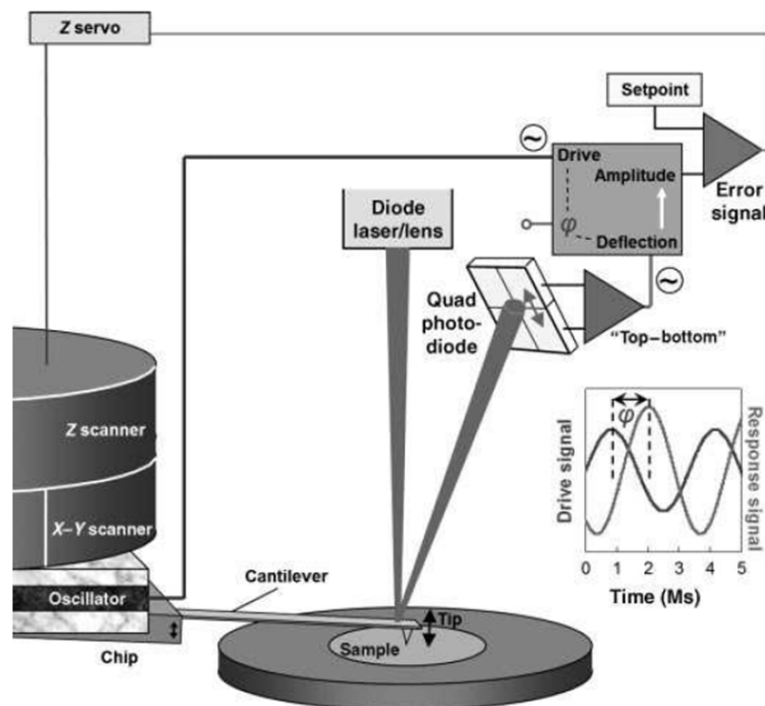
Figure 2.23: Schematic representation of a tapping mode set up.

- the cantilever is oscillated at its resonance frequency with an amplitude ranging typically from 1 nm to 100 nm.

- the feedback loop maintains a constant oscillation amplitude

- the vertical position of the z scanner at each (x,y) data point in order to maintain a constant set-point amplitude is stored by the computer to form the topographic image of the sample surface

- by maintaining a constant oscillation amplitude, a constant tip-sample force is kept constant

- operation can take place in ambient and liquid environments

- due to the movement of the tip perpendicular to the surface, lateral forces are almost eliminated

- when imaging in air, the typical amplitude of the oscillation allows the tip to contact the surface through the adsorbed fluid layer without getting stuck

Non-contact mode

To achieve non-contact AFM the tip must be close enough to the sample surface to achieve high sensitivity, without passing into the repulsive regime used for contact mode AFM. Indeed, as explained before, non-contact AFM is carried out in the attractive regime (van der Waals force). By using a highly stiff cantilever (resonance frequency between 300 kHz and 400 kHz) and monitoring the change in oscillation, it is possible to maintain the cantilever very close to the surface without jumping to the repulsive regime. It is possible to observe changes in the oscillation amplitude and phase in this regime. See subsection 2.4.1 for more detail. As with all dynamic modes of operation, scanning speed is usually lower than in contact mode. When used in Ultra High Vacuum (UHV) conditions, frequency modulation is usually used. See subsection 5.1.2. One of the limiting factors for non-contact mode in air is the capillary layer present on the surface.

To wrap up, non-contact AFM is described by the following points:

- the cantilever is oscillated at a frequency slightly above the cantilever's resonance frequency typically with an amplitude of a few nanometers (<10 nm)

- the cantilever's resonance frequency is decreased by the van der Waals forces, which extend from 1 nm to 10 nm above the adsorbed fluid layer. The decreasing in resonant frequency causes the amplitude of oscillation to decrease

- the feedback loop maintains a constant oscillation amplitude or frequency by vertically moving the z scanner at each (x,y) data point until a set-point amplitude or frequency is reached

- the distance the z scanner moves vertically at each (x,y) data point is stored by the computer to form the topographic image of the sample surface

2.4 AFM theory

We treat the tip/cantilever system as an equivalent point mass m^* attached to a spring of stiffness k_0, a simple harmonic oscillator swinging toward and away from sample at its resonance frequency

$$\omega_0 = \sqrt{k_0/m^*} \tag{2.4}$$

The force on the tip are the sum of the cantilever's restoring force, $F_{cantilever}$ and the tip-sample interaction force $F_{tip-sample}$. The cantilever force is obviously given by the Hooke's law

$$F_{cantilever} = -k_0(z - z_0) \tag{2.5}$$

where $z - z_0$ is the tip displacement from the equilibrium position z_0 (undeflected cantilever state, zero force). For convenience, we take the zero of the z axis to be corresponding to the point where $F_{tip-sample}$ is zero. The tip-sample interaction force is the one considered at the end of Section 2.2, a combination of relatively weak attraction at longer distances and steep, strong repulsion at short distances. Thus, we can say the total force acting on the tip-cantilever system to be

$$F_{total} = F_{cantilever} + F_{tip-sample} \tag{2.6}$$

2.4.1 Damped, forced harmonic oscillator

When we come to oscillating modes AFM, the cantilever behaves as a driven harmonic oscillator with damping. The driving signal is a sinusoidal force vibration $F = F_0 cos(\omega t)$ applied to the base of the cantilever. The damping of a freely (no

tip-surface forces, so far) oscillating cantilever is primarily due to the fluid medium, air or liquid, equivalent to a damping coefficient b (i.e., a damping force proportional to the velocity of the tip, $F = -bv = -b\dot{z}$).

The mathematical description of a damped, driven harmonic oscillator is a classic undergraduate physics problem, solving Newton's second law of motion. The resulting linear, second order differential equation is:

$$m\ddot{z} = F_0 cos(\omega t) - \frac{m^* \omega_0}{Q}\dot{z} - k_0 z \tag{2.7}$$

where the useful dimensionless parameter Q is the quality factor, given by

$$Q = \frac{m^* \omega_0}{b} \tag{2.8}$$

It quantifies the sharpness of the resonance curve and, importantly, is inversely related to the strength of damping. Its value can be approximately determined from the ratio of resonance frequency divided by the full width of the amplitude peak at $\sim 70\%$ of its peak value.

The solution of 2.7 is made up of an initial transient term, which we will not consider here, and a steady-state particular solution for the case of underdamped motion ($\omega_0 > b/2m^*$, the relevant case for AFM). This solution describes the frequency dependence of the amplitude and phase shift of the sinusoidal motion of the tip relative to the driving wave, see Figure 2.24.

$$A = \frac{A_{drive}Q}{\sqrt{(\frac{\omega}{\omega_0})^2 + Q^2(1 - (\frac{\omega}{\omega_0})^2)^2}} \tag{2.9}$$

$$\phi = arctan[\frac{\frac{\omega}{\omega_0}}{Q(1 - (\frac{\omega}{\omega_0})^2)}] \tag{2.10}$$

where A_{drive} is the amplitude of the drive signal.
As can be seen, the frequency functional relations with amplitude and phase shift are given by Lorentzian (similar to a Gaussian-shape) and arctangent functions, respectively.
One can also notice that if we excite the cantilever at its resonance frequency ω_0 the oscillating amplitude will become

$$A = A_{drive}Q \tag{2.11}$$

while the phase shift will reach the value of $90°$.
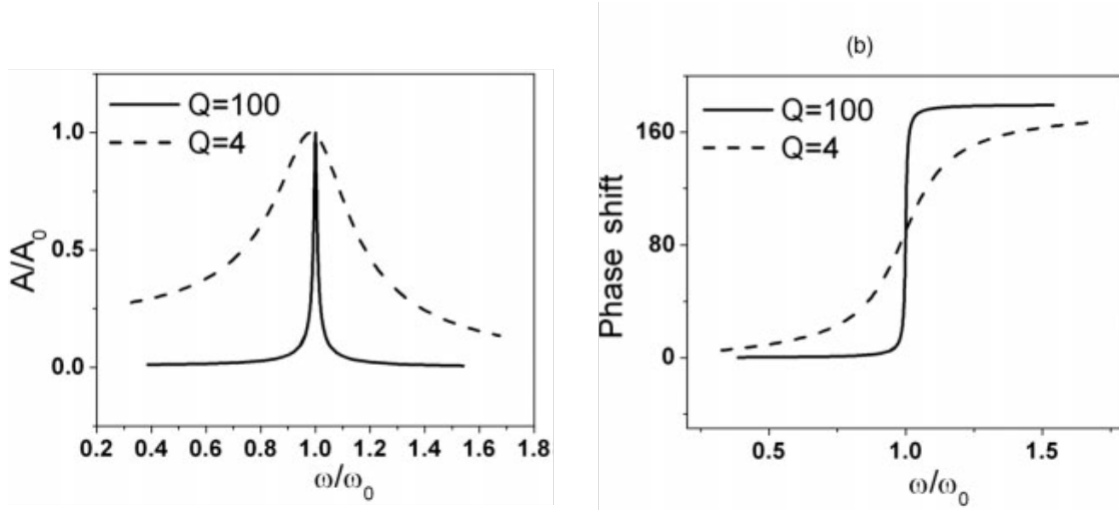
Figure 2.24: Frequency response of the amplitude of oscillation and of the phase shift.

There is a peak in amplitude when the driving frequency ω is equal to the resonance frequency ω_0 of the cantilever.

Two important remarks should be done in conclusion and they deal with the limitations of the forced harmonic oscillator with damping. Indeed:

- **Equation 2.7 considers the cantilever tip system as a point mass spring, which means that the higher flexural modes of the cantilever are ignored. In Multifrequency AFM they are taken into account, instead. For instance, in bimodal AFM, the cantilever is simultaneously excited by two driving forces which are tuned to match two of the flexural eigenmodes of the cantilever, usually the first and the second ones ([17]).**

- **in Equation 2.7 the Q factor is independent of tip sample separation, which means that changes in the hydrodynamic damping of the cantilever during its motion are neglected. This is not always true ([18]).**

2.4.2 Dynamics of a weakly perturbed harmonic oscillator

Let us assume that the cantilever-tip system is oscillating under the influence of tip surface forces (see Section 2.2). For small displacements with respect to the equilibrium position of the cantilever, which we assume to be at z=0, the tip surface

force can be expressed by a simple Taylor first order expansion:

$$F_{ts}(z) \sim F(0) + (\frac{dF_{ts}}{dz})_0 z \tag{2.12}$$

In this approximation, the gradient of the force is the relevant factor that influences the tip motion. Then, being the gradient linear in z, the interaction can be characterized by an effective spring constant $k_{ts} = -(dF_{ts}/dz)_0$. By substituting the last expression in the second Newton's law, we recover the full equation of a driven damped harmonic oscillator affected by an interaction force:

$$m\ddot{z} = F_0 cos(\omega t) - b\dot{z} + F_{ts}(0) + F'_{ts}(0)z - k_0 z \tag{2.13}$$

with an effective spring constant $k_{eff} = k_0 - F'_{ts}(0) = k_0 + k_{ts}$. Then, the new effective resonant frequency is obtained as $\omega_{eff} = \sqrt{k_{eff}/m^*}$ and the difference $\Delta\omega = \omega_{eff} - \omega_0$ can be approximated ($k_{ts} << k_0$) by

$$\Delta\omega \sim \frac{\omega_0 k_{ts}}{2k_0} \tag{2.14}$$

which can be written also as:

$$\frac{\Delta\omega}{\omega_0} \sim -\frac{1}{2}\frac{F'_{ts}(0)}{k_0} \tag{2.15}$$

The above equations shows that, whenever the interaction force can be approximated by its linear term, the tip-cantilever system still behaves as an harmonic oscillator with a shifted resonance frequency. Due to this, we can immediately write also the phase shift which will resemble Equation 2.10:

$$\phi = arctan[\frac{\frac{\omega}{\omega_{eff}}}{Q(1 - (\frac{\omega}{\omega_{eff}})^2)}] \tag{2.16}$$

This expression can be usefully developed further. Indeed, if we write it as:

$$\phi = arctan[\frac{\omega\omega_{eff}}{Q(\omega_{eff}^2 - \omega^2)}] \tag{2.17}$$

then, making use of $tg^{-1}(x) + tg^{-1}(1/x) = \pi/2$, we can say:

$$\phi = \frac{\pi}{2} - arctan[\frac{Q(\omega_{eff}^2 - \omega^2)}{\omega\omega_{eff}}] \tag{2.18}$$

Therefore, if now we set $\Delta\Phi = \Phi - \pi/2$, one has:

$$\Delta\phi = -arctan[\frac{Q(\omega_{eff}^2 - \omega^2)}{\omega\omega_{eff}}] \tag{2.19}$$

Since $\omega_{eff} \sim \omega \sim \omega_0$, then:

$$\omega_{eff}^2 - \omega^2 \sim 2\omega_0 \Delta\omega \sim -\omega_0^2 \frac{F_{ts}'}{k_0} \qquad (2.20)$$

where we have here made use of Equation 2.15. Inserting the last expression in Equation 2.19, one has

$$\Delta\phi = arctan[\frac{Q\omega_0}{\omega_{eff}} \frac{F_{ts}'}{k_0}] \qquad (2.21)$$

Finally, if we assume, as before, $\omega_{eff} \sim \omega_0$, and we use the Taylor expansion $tg^{-1}(x) \sim x$ (since $k_{eff} \ll k_0$), then we end up with

$$\Delta\phi = \frac{Q}{k_0} F_{ts}' \qquad (2.22)$$

which is an important formula, widely used in the so called **Phase-EFM**.

Coming back to Equation 2.13, it is important to keep in mind the assumptions behind it:

- **the tip-surface forces induce a frequency shift and not an energy transfer**

- **the force gradient was assumed independent of the separation between the tip and the surface**

- $F_{ts}'(0) \ll k_0$

Several experiments violate at least one of the above points. A quantitative discussion on the limitations of the harmonic approach to interpret dynamic AFM is provided by Holscher ([19]).

The dependence of the amplitude on the excitation and effective resonant frequencies provides the first mechanism to explain the dependence of the oscillation amplitude with the strength of the interaction force, or in other words, with the tip-surface distance.

Let us assume that the tip is excited at its resonance frequency; approaching the tip toward the surface will modify the resonance frequency that in turn implies a modification of the oscillation amplitude. The actual oscillation amplitude will be given by the value of the new resonance curve at the excitation frequency of the oscillator ω_0. As a consequence, the new oscillation amplitude will be smaller than the free amplitude (both for $F' > 0$ and $F' < 0$).

Specifically, if we are dealing with an interaction region where $F' > 0$, then k_{ts} will be negative inducing a smaller ω_{eff} with respect to ω_0. This, as shown in Figure 2.25, will cause a shift toward smaller frequencies of the resonance amplitude curve and so **the new oscillation amplitude correspondent to the resonance frequency $\omega = \omega_0$, will be reduced**. Regarding the phase shift, a similar discussion can be done, obtaining, as a result of the interaction, again a shift of the phase resonance curve toward smaller frequencies. This effect, in this case, will set **the new phase shift to a bigger value than the $90°$ typical of a free oscillating cantilever**. Opposite conclusion can be obtained if we consider the case $F' < 0$.
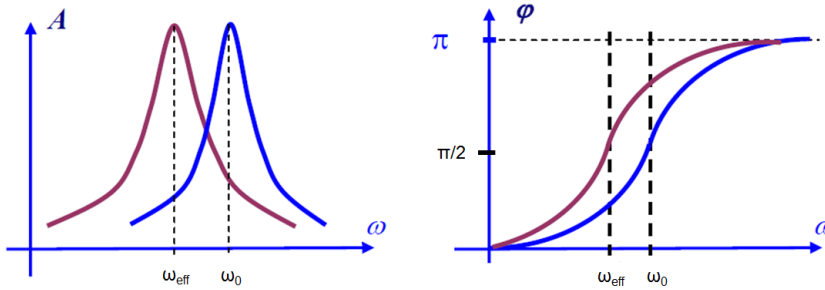

Figure 2.25: The effect of a weak interaction (attractive regime) on the amplitude and phase resonance curve.

2.4.3 Phase shift: attractive and repulsive regimes

The previous analysis of the tip motion has been done referring to a weak linear perturbation directly connected with the first derivative of the force between the tip and the sample. If we make the assumption that the interaction under investigation can be described by a Lennard-Jones potential, like in Section 2.2, then we can introduce two regimes of interactions: the attractive and repulsive ones. The attractive regime deals with $F' > 0$ and corresponds to the region where the force is increasing; on the other hand, the repulsive regime corresponds to $F' < 0$ which represents regions where the force is decreasing.

As already presented in 2.2, the real interaction between a non mono-atomic tip and the sample is different from a pure Lennard-Jones interaction. If we now make the assumption that the real interaction is described by the formulas 2.3 and 2.2, the attractive and repulsive regimes definition changes into a more appropriate one dealing with the average force acting on the tip in a cycle. Indeed, Garcia ([20])

showed that an AFM operated in amplitude modulation feedback has two regimes of operation. **In the first, the attractive regime, a net attractive force dominates the amplitude reduction while in the other, the repulsive regime, a net repulsive force controls the cantilever dynamics**. The operating regime is defined to be attractive when the average force in one oscillation is negative. **With this definition both regimes may involve long range attractive forces as well as short range repulsive forces**. The transition between the two regimes is reflected in the tapping mode parameters. To use amplitude curves to determine experimentally the operating regime may be time consuming. **The phase shift, instead, allows to easily identify whether the operating regime is attractive or repulsive**.

In most situations, the amplitude decreases with the tip sample distance. However, a sharp jump in the amplitude curves has been reported by experiments and simulations. This jump has been attributed to the beginning of the repulsive regime, i.e. the oscillation switches from a purely non contact (long range attractive forces) to tapping mode (attractive and repulsive). However, it is shown that a step like discontinuity in the amplitude curve is not an exclusive characteristic of the non contact to tapping mode transition. It can be due also to the existence of two oscillation states.

Following Garcia's work, the transition between the attractive and repulsive regime may be smooth or step like, depending on free amplitude and material properties. **The combination of stiff materials and small free oscillation amplitudes usually gives rise to discontinuities**. In Figure 2.26, it is shown a numerical simulation for silicon dioxide and a cantilever tip system with a resonance frequency of 350 kHz, see[20] for more detail. The following conclusion can be drawn:
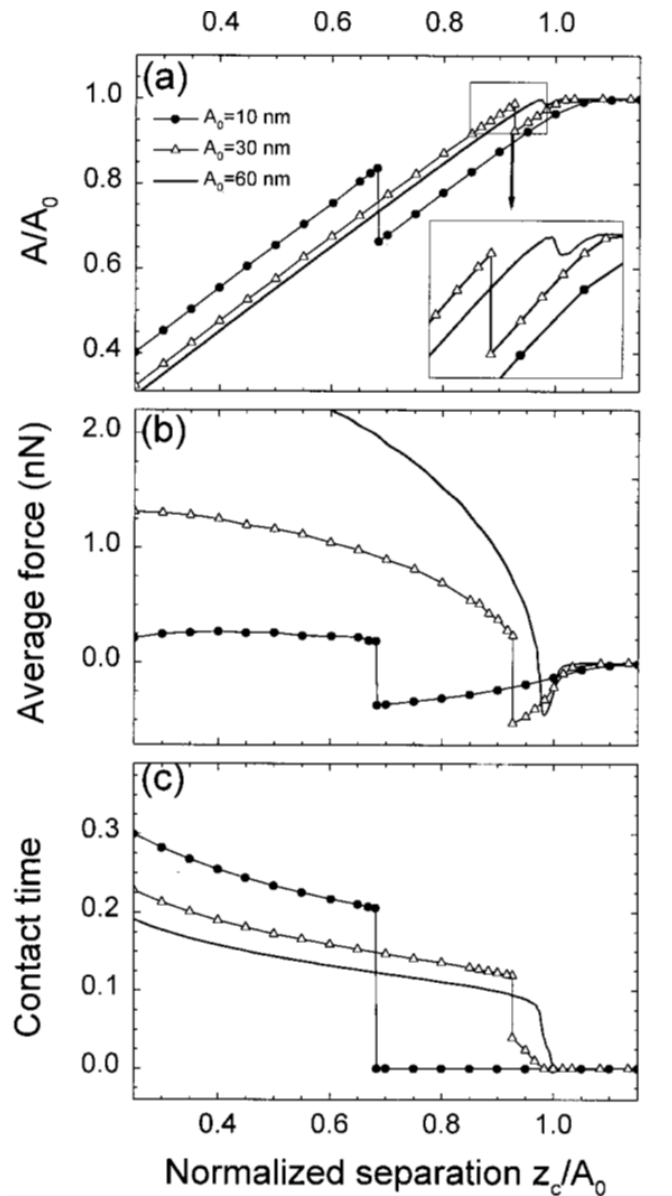
Figure 2.26: (a) Amplitude, (b) average force, (c) normalized contact time dependence on tip sample separation for three free amplitudes: 10 nm (black points), 30 nm (white triangles) and 60 nm (continue black line). The four different interaction regions (1), (2), (3) and (4) are explained in the text.

- **Amplitude**:
  for the three different free amplitudes A_0=10, 30 and 60 nm we have four different regions, (1), (2), (3) and (4), as we approach the sample. First, in region (1), there is a flat behaviour where the effect of attractive force is negligible. Second, in part (2), the cantilever starts to feel the attractive forces. This usually reduces the amplitude of oscillation. Third, there is a
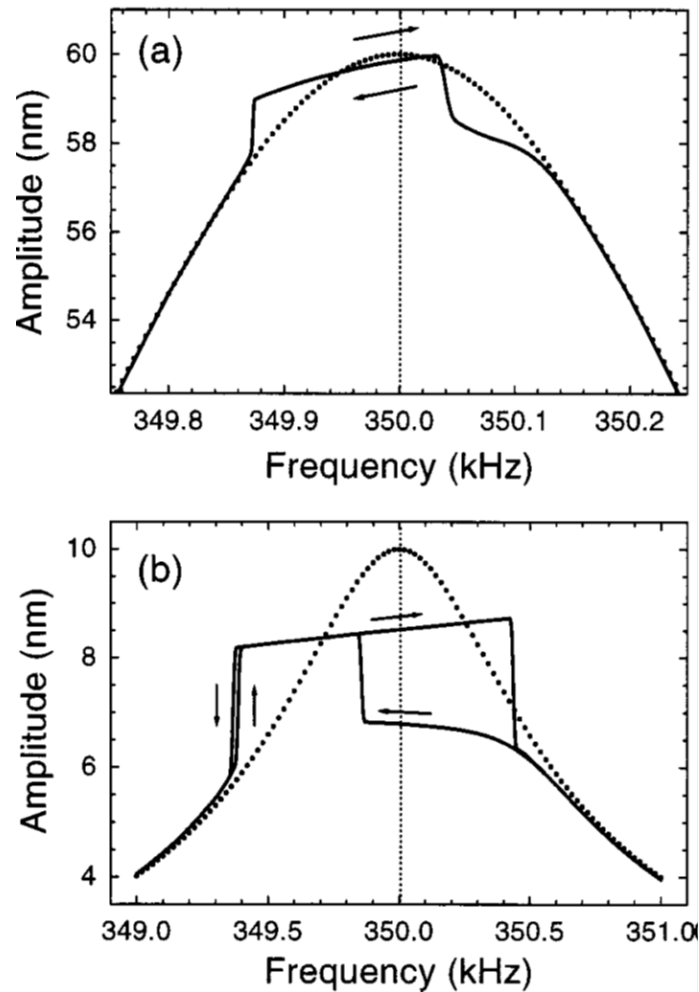
Figure 2.27: Amplitude plot as a function of the driving frequency. The free oscillating case is plotted by a dotted line. (a) A_0 =60nm. (b) A_0= 10 nm. The arrows indicate the direction of the frequency sweeps.

transition region (3) where the amplitude shows an increase. Fourth, after the transition the amplitude decreases again in part (4). The shape of the transition curve depends on the free amplitude. For 10 and 30 nm, indeed, a step-like discontinuity is observed, while for 60 nm the transition is continuous. In all the three studied cases, the amplitude curves by itself does not reveal if its reduction is due to attractive interaction or repulsive, or a combination of both.

- **Average force**:
  In plot b of Figure 2.26, the average force experienced by the tip during a symmetric cycle is plotted. For A_0=10 nm, at large z, the average force is negative (attractive). It increases in absolute value as z decreases until a
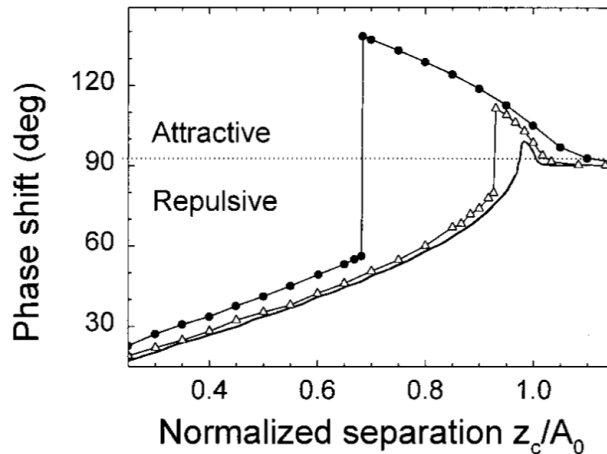
Figure 2.28: Phase shift dependence on tip sample separation.

sudden change of sign is observed. From there on, the average force remains positive (repulsive). A similar behaviour is observed for $A_0=30$ nm. However, for 60 nm the force shows a continuous change with z.

The comparison of the amplitude and average force, shows a correspondence between the changes observed in the amplitude and in the the force curve. **The average force curves allow us to define two regime of operation, attractive and repulsive**.

- **Frequency**:
  As can be seen by the amplitude-frequency plots, Figure 2.27, for small free amplitudes two steady states for the amplitude are possible. A higher amplitude state, that implies tip sample contact and a lower amplitude state, that may or may not imply tip sample contact. The jump marks the transition between one state to the other. This is also known as **the bistable behaviour**. The system will reach one state or the other depending on the starting conditions. The bistability depends on the sample properties, free amplitude, tip sample distance, and working frequency.

- **Phase**:
  To use amplitude curves to determine experimentally the operating regime may be impractical. As shown in Figure 2.28, **the phase shift, instead, allows to identify whether the operating regime is attractive or repulsive without possible contradictions. The attractive regime is characterized by phase shifts $\Phi > 90°$ while in the repulsive regime Φ is always below $90°$.**

Experimentally, in order to have a good quality AFM image, it is important to keep the tip always in the same regime, or attractive or repulsive, and this can be understood visualizing the phase shift during the scan. A phase shift always bigger or smaller than $90°$, in each scanned line, will be the fingerprint of a good interaction between the tip and the surface atoms. It is an established practice in SPM to attribute noisy or unstable data to a contaminated or bad tip shape. Here we have seen that a non linear dynamics analysis shows that in many cases noisy or unstable data only reflect the intrinsic structure of the tip motion.

2.5   Measuring AFM images

Like all techniques, AFM requires some skill and practice to operate well. In this section we discuss the procedures that can make measuring AFM images easier.

2.5.1   Scan conditions: contact mode

Once the probe and optical alignment are done, and the probe approach completed, one has to start the image and optimize the scanning parameters for the best possible AFM image. Often, standard parameters are used initially for the approach, and such numbers might be provided by the instrument's manufacturer. However, these value will rarely be suitable to obtain good images. That is why one needs a method to optimize the scanning parameters which is, basically, an iterative method. The parameters are changed one at a time, until the tip is properly following the surface. It can be very useful to show both forward and backward scanning lines. Since they measure almost the same parts of the sample the two height traces should coincide. Large differences in the forward and backward lines are an immediate indication that something is going wrong. The most common reason for these kind of problems is that imaging parameters (gain, setpoint, scanning speed) are not yet optimized. In Figure 2.29 the effect of different feedback settings on a simple sample are shown. Before coming to the set of the best parameters for imaging, an important detail has to be underlined. Since in contact mode AFM we are working with a constant deflection of the cantilever due to a constant interaction with the substrate, a specific procedure has to be followed in order to have the maximum signal from the photodiode during the scan. Indeed, if after the laser alignment we set a constant deflection with the setpoint, during the whole imaging the laser spot will not be anymore in the centre of the photodiode. This can decrease the quality of the image. The way to overcome this problem is **to centre the laser not in the middle of**

the photodetector but slightly down in order to compensate the constant shift we will have in normal force during the scan.

The general procedure to use to adjust scanning parameters, instead, is as follows:

1. increase feedback gain step by step, observing for the start of feedback oscillation

2. when feedback oscillation occurs, reduce the gain again, until it disappears. **The optimal value is the highest gain setting one can use without adding feedback noise to the image**

3. when gain is optimized, adjust the setpoint. Ideally, **we would use the minimum value to keep the probe on the surface, in order to reduce probe wear**

4. gain may need to be optimized again to account for the change in set-point

5. adjust scan speed if desired

6. gain and set-point may need adjusting once more to take into account of change in scanning speed
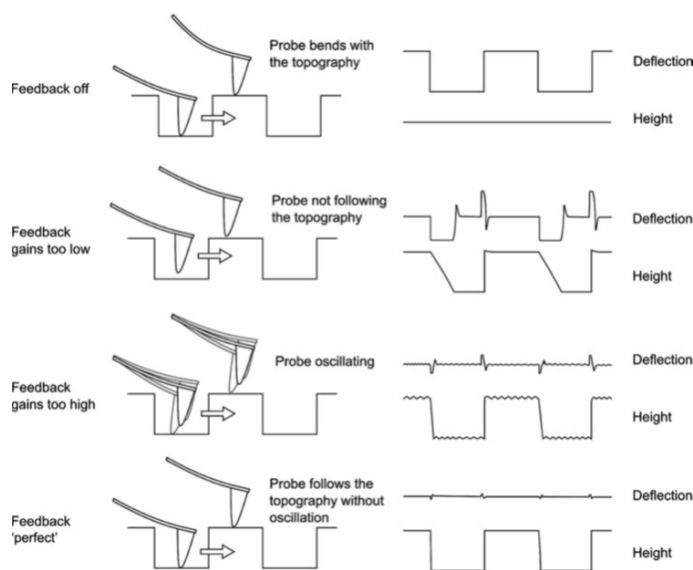
Figure 2.29: The effect of different feedback settings on the height topography.

2.5.2 Scan conditions: oscillating modes

Measuring images in oscillating modes is in general very similar to contact mode, with just a few differences. Firstly a non contact/tapping probe is usually with a much higher resonance frequency. One practical consideration, instead, is that oscillating modes probes are even more fragile and easy to break than contact probes, so more care must be taken with them.

The optical alignment procedure is identical to contact mode. When the alignment is achieved, the operating frequency must be selected. This is often done automatically. Automated routines sweeps the oscillating frequency of the driving piezo up and down over a fixed frequency range and displays the amplitude of oscillation at each point. Within this range, the cantilever's oscillation should be visible as a single, strong peak. **The presence of multiple peaks in the frequency spectrum in unexpected positions, is an indication of a not ideal behaviour of the cantilever. The probe could be damaged or not fixed correctly in the probe holder**. Once the peak is located, typically the user should zoom into the relevant part of the frequency spectrum to visualize the peak more clearly. The instrument often shows not only oscillation amplitude vs frequency, but also phase shift (with respect to the driving piezo signal) vs frequency. The resonance frequency represent the point at which the amplitude is maximum and the phase shift is 90°. A better explanation of the physics behind cantilever's oscillation is given in Section 2.4.1. An example of amplitude/frequency and phase shift/frequency are shown in Figure 2.24.

Having selected the operating frequency, the amplitude of the driving piezo oscillation is adjusted to give the desired oscillation amplitude to the cantilever.

In most AFM systems, an amplitude setpoint is then chosen. **For contact mode AFM, the setpoint is a deflection value, which means that increasing the setpoint leads to greater forces between the tip and the sample. However, for tapping mode, feedback is based on a decrease in amplitude, so a lower setpoint means a greater tip-sample interaction force**. Once the oscillation frequency and amplitude setpoint are chosen, the approach can be made. Having approached successfully, scanning and optimization of parameters are very similar to contact mode.

2.6   AFM image processing and statistical analysis by Gwyddion

Gwyddion open source software ([10]) is a multiplatform modular software for Scanning Probe Microscopy (SPM) data processing and analysis. The functionality of Gwyddion is described in its User guide, which can be downloaded from the Gwyddion web site, and here we just want to give an overview about all the main tools one can find in Gwyddion.

2.6.1   Processing AFM images

Data representing the morphology of a sample/AFM image are collected as a matrix of points corresponding to z values in a square array. The purpose of processing an AFM image is to make it easier to measure and observe the features on the measured sample. However, processing steps always change the AFM data, so one must be careful. This is why, **if more than one image has to be processed and then statistically analyzed/compared, the same processing procedure should be followed**.

For our images, the common processing procedure was the following:

- take the raw AFM image

- plane fitting

- remove scars

- correct lines

- 2:2 polynomial fitting

- remove features which are **clearly** errors (due to a fake tip-sample interaction for instance) or which are **clearly** not desired (like crystals whenever one is looking at the thin film phase of the organic semiconductor under investigation). This operation can be done selecting by threshold these bad features (Data Process $\rightarrow$ Grains $\rightarrow$ Mark by threshold) and then removing them with Data Process $\rightarrow$ Correct Data $\rightarrow$ Remove data under mask. Eventually, even fake deep spikes can be present in the image; for these it is convenient to select - invert height - option during the threshold selection and remove them with the same previous procedure

- color range option

- select all the important features on the substrate by threshold and execute a plane fitting, a correct lines and a 2:2 polynomial fitting only on these marked regions

- Data Process → Level→ Fix zero in order to select the lowest pixel of the AFM image as the z=0 origin of the z axis

Levelling

Levelling is usually the first processing operation carried out on the data. AFM images usually measure sample height. If the background in the image has considerable tilt in it, the change in height of the background will mask the changes in height associated with the sample. For example, imagine a $20\mu m$ x $20\mu m$ image which contains some 50 nm nanoparticles which the user would like to examine. If the substrate is tilted by only 1°, the height change from one side to the other of the substrate will be about 350 nm, enough to mask all the nanoparticles.
In addition to tilting in the image a common problem in AFM images is scanner bow and this artefact leads to a curve in the image. There are a number of different methods that can be used for image levelling, and these are discussed below.

- Fix zero (Data process → Level → Fix zero) :
  The simplest module that is connected with data levelling is Fix zero that simply sets the minimum height of the sample to zero

- Polynomial fitting:
  a very common method for levelling AFM images is by polynomial fitting, or line-by-line levelling. In this routine, each line in the image is fit to a polynomial equation. Then, the polynomial shape is subtracted from the scan line. Typically each horizontal line of the image is processed in this way, although the process can also be carried ut on vertical lines. It is usually better to do this horizontally, because the horizontal axis is usually the fast scan axis. The order of the polynomial equation can vary from 0 to 3 or more, as shown in the following table.

  For many images, a first order fit will suffice. If scanner bow is present in the image, a second order fit will usually be appropriate to remove the artefact. Orders higher than third level are possible. **It is worth noting that**

Order	Effect
0	Only sets the height offset of each scan-line to the same value.
1	Fits a straight line equation to each scan-line, and does an offset.
2	Fits a quadratic equation to each scan-line, and does an offset.
3	Fits third order polynomial to each scan-line, and does an offset.

Figure 2.30: Effects of different polynomial levelling orders.

line-by-line fitting procedures are particularly prone to causing levelling artefacts, and so feature exclusion is often required.

- Two-dimensional plane fitting:
  this procedure tries to automatically fit a flat plane to the image, and subtracts the best fit plane; it works well where the background is really flat, and does not include any curvature or scanner bow. The automatic routine will usually assume the whole image is to be fitted; this means that it can be subject to errors as large height features will reduce the accuracy of the fit to the background. Plane fitting does not introduce the kind of errors mentioned above with the line-by-line fitting. It is therefore a rather conservative levelling procedure, as although it is not very efficient with many images, it does not introduce any errors.

- Three points fitting:
  this procedure is similar to the previous one, but is a rather more manual approach. In this method, the AFM user identifies three points on the image. These points define a plane which is then subtracted from the image. The advantage of this method over the automatic plane removal is that if the user can distinguish the substrate from the sample features, he can ensure the three points are on the substrate only, and this often leads to a better fit. However, because a flat plane is fitted, it is still only suitable for images with no curvature or scanner bow. It is particularly appropriate for samples with terraces. An example, showing the effect of different levelling algorithms on an image with a large terrace, is shown in the following figure:

- Exclusion of points from fit:
  with the most common type of levelling, polynomial line fitting, the presence of raised features on the substrate will cause a levelling artefact. This occurs
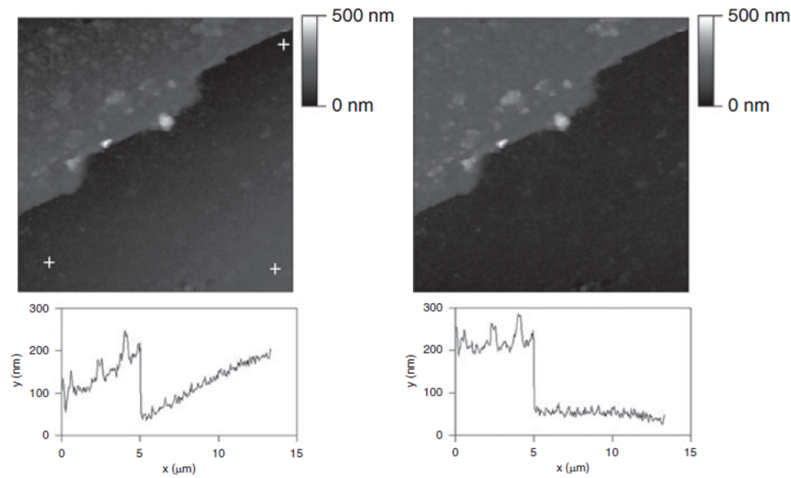
Figure 2.31: Left: result of plane fitting to an image with two distinct levels. The global plane fit does not give a good result, as it assumes the entire image to be on the same plane. A global polynomial fit would not work well either. Right: result of three points plane fitting using three points indicated by crosses in the left image. The result is a much flatter background(see profiles).

because the algorithm fits the entire line, and sets it to the same level as all the other lines in the image. Thus, where large features occur on a line, the substrate becomes artificially lowered, and the image ends up with what look like shadows behind any large features. **This problem is easily overcome by simply excluding the features from the fitting procedure**.
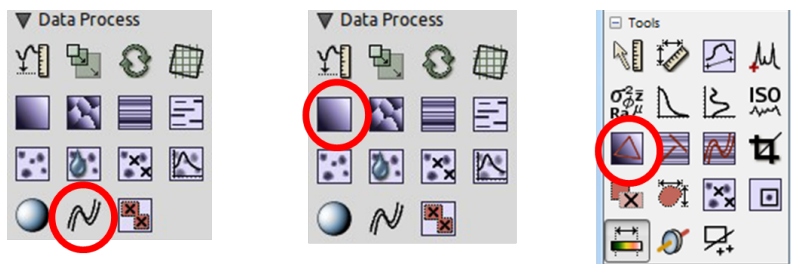

Figure 2.32: Illustration of the positions the above options can be found on the Gwyddion main window. From left to right: Polynomial fitting, Plane fitting, Three points fitting.

Data correction

AFM images often contain errors, which typically result from unwanted interactions of the tip with the sample, such as sample movement under the tip, or strong tip

sample forces leading to vibration or streaking in the images. If it is not possible to acquire a new image without the errors, the user may wish to remove them. This can be achieved by specific routines in the AFM processing software. These sorts of corrections should be used with great caution as the correction process will change the data. For example, data that was subjected to error correction will exhibit lower roughness values after treatment, and these values do not reflect the true roughness of the surface.

- Remove spots:
  The Remove spot tool can be used for removing very small parts of the image that are considered a scanning error, dust particle or anything else that should not be present in the data.

- Remove scars:
  Scars (or stripes, strokes) are parts of the image that are corrupted by a very common scanning error: local fault of the closed loop. Line defects are usually parallel to the fast scanning axis in the image. This function will find and remove these scars, using neighbourhood lines to fill in the gaps.
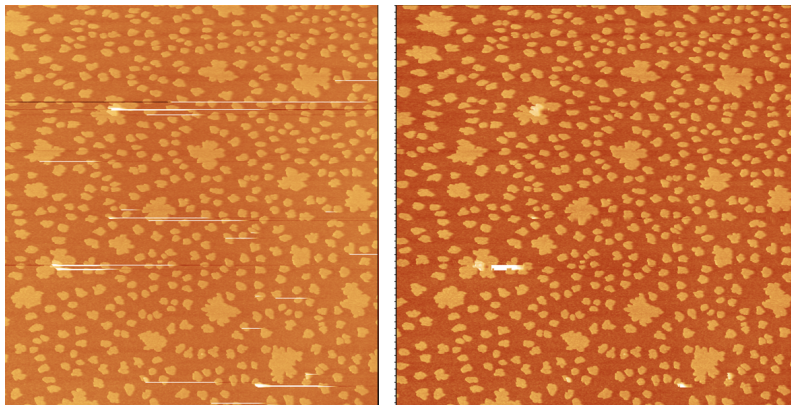

Figure 2.33: Illustration of the Remove scars tool. Left: original image. Right: corrected image.

- Remove data under mask:
  This function substitutes the data under the previously selected mask by the solution of the Laplacian equation. The data values around the mask defines the boundary conditions.

- Line correction:

  Profiles taken in the fast scanning direction (usually x axis) can be mutually shifted by some amount or have slightly different slopes. The basic Line correction functions deal with this type of discrepancy. Several functions can be used. One of the most common is the Median Difference Line Correction (Data Process → Correct data → Median Difference Line Correction) which shifts the lines so that the median of differences (between vertical neighbour pixels) becomes zero. Therefore it better preserves large features while it is more sensitive to completely bogus lines.
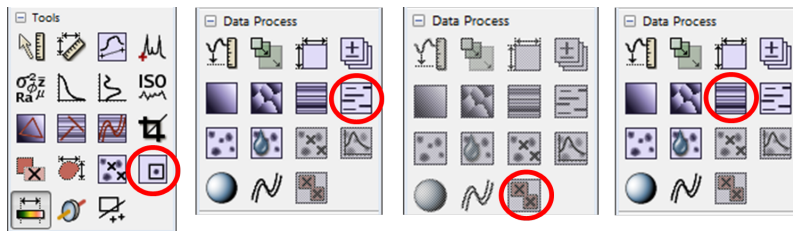

Figure 2.34: Positions of the above options on the Gwyddion main window. From left to right: Remove spots, Remove scars, Remove data under mask, Line correction.

2.6.2   Analysing AFM images

Several ways can be followed in order to statistically characterize the morphology of a sample analyzed by AFM. This should be done with a small number of quantities, sampling independent, which means quantities that are intrinsic properties of the surface. Two classes of quantities can be used to characterize a surface: first order statistical quantities and second order statistical quantities. **Roughness and fractal dimension** are examples of the first class, **autocorrelation function (ACF), power spectra density function (PSDF) and height-height correlation function (HHCF)** are examples of the second class.

Here we will introduce only the first class parameters since they will be used in Chapter 7 and not the others. Details on the second class quantities can be found in standard text books.

Roughness

There are a number of different ways to measure roughness which are all listed in the Gwyddion User guide. The most commonly used roughness parameter is the **root**

mean square roughness (RMS), which means the standard deviation of the z height probability distribution. Still, this is not a complete characterization of the morphology of a sample since several height profiles can be found, quite different in appearance, but with the same RMS. **Skewness and kurtosis** try to fill this gap, even if other quantities can still be found to have more details on the topography. Skewness is a measure of the asymmetry of the distribution of heights. Random variations in morphology will give rise to a skewness value of 0. Positive values indicate the presence of height values considerably above the average, while negative values indicate the presence of height values considerably below the average. Kurtosis, instead, describes the peakedness of the distribution of height values. High kurtosis means a small number of extreme heights (very high peaks or very low valleys), while a lower, or negative, kurtosis value means many moderate height features. Mathematically, skewness is the third moment of the height distribution, while, kurtosis, the fourth.

In Gwyddion one can find all these height distribution parameters using the - Statistical quantities tool -, see Figure 2.35, otherwise the - Calculate row/column statistical functions - is available. Averaging on each row or column of the single line RMS is typically done.
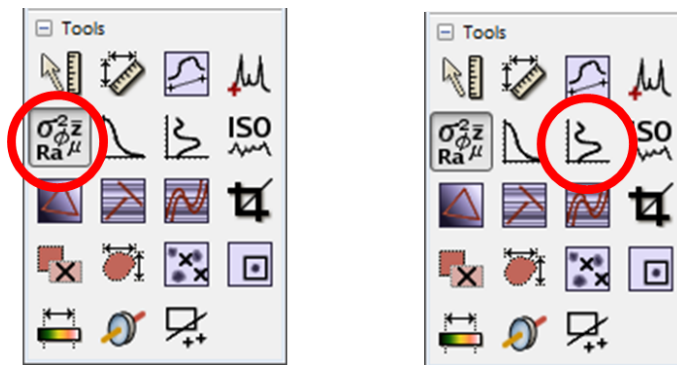
Figure 2.35: Statistical quantities tool (left) and Calculate row/column statistical functions tool (right) on the Gwyddion main window.

Fractal dimension

Surfaces created by some technological processes are expected to have fractal properties ([21]). Fractal analysis of the AFM data usually concentrates on determining the fractal dimension D_f of a given surface, which is the basic quantity used for

characterizing self-similar and self-affine objects.

Generally, the concept of fractal dimension can be explained in the following way. Suppose that we have an object embedded in a space of Euclidean dimension D_e. The volume $V(l)$ of this object cabe measured by covering it with D_e-dimensional spheres of radius l and volume going as l^{D_e}. Then, we need $N(l)$ spheres to cover the object and to measure its volume by means of spheres as:

$$V(l) = N(l)l^{D_e} \tag{2.23}$$

Usually, the relation $N(l) \sim l^{-D_e}$ is valid for changing the size l of the spheres used as measures. However, **it can happen that the relation $N(l) \sim l^{-D_f}$ where $D_f < D_e$ is valid. Objects having this property are called fractals and have fractal dimension D_f.**
Consequently, we can determine the fractal dimension as:

$$D_f = \lim_{l \to 0} \frac{ln\ N(l)}{ln\ (1/l)} \tag{2.24}$$

In fact, many methods of fractal dimension determination are just an implementation of the above relation.

Within Gwyddion, there are different methods of fractal analysis implemented by Data Process $\to$ Statistics $\to$ Fractal analysis. One of the most used is the cube counting method.

Cube counting method: it is derived directly from a definition of box counting fractal dimension. The algorithm is based on the following steps: a cubic lattice with lattice constant l is superimposed on the z expanded surface. Initially l is set as X/2 (where X is length of edge of the surface), resulting in a lattice of 2x2x2=8 cubes. Then *N(l)* is the number of all cubes that contain at least one pixel of the image. The lattice constant l is then reduced stepwise by factor of 2 and the process repeated until l is equal to the distance between two adjacent pixels. The slope of a plot of *log (N(l))* vs *log (1/l)* gives the fractal dimension D_f directly.

Other three methods are available in Gwyddion to calculate the fractal dimension: Triangulation method, Variance method and Power spectrum method. Each one typically gives a different fractal dimension value. A common practise is to take the average between the four values.

In our case, for the fractal dimension calculation involved in the analysis of data collected by in-situ real time AFM experiments (see Chapter 7), we did not used Gwyddion as a reference software but **fractalyse** ([22]).

The method we followed to obtain the fractal dimension was:

- take the raw AFM image and process it by Gwyddion

- make a .jpg of it

- open the .jpg AFM image with ImageJ ([23])

- make a 8-bit image out of it following the path Image $\rightarrow$ Type $\rightarrow$ 8-bit

- execute Image $\rightarrow$ Adjust $\rightarrow$ Threshold

- move the scale indicator in order to select in black only the AFM image's features under investigation. It is fundamental to have previously flatten the AFM image, by Gwyddion, in the best way

- save the image in the .bmp or .tiff format. These are the ones that fractalyse can deal with.

- open the .bmp or .tiff image with fractalyse

- follow Analyse $\rightarrow$ Box (if a box counting method is desired)

- **in our case we decided to fit the plot always with a non linear function of this kind:** $y = a * x^d$ (see Avanced option)

Grain analysis

Another option in Gwyddion is the possibility to count the number of islands lying on the substrate. Unfortunately, we did not find this Gwyddion tool very accurate so we decided to shift to another software, ImageJ ([23]). Here we write the procedure to be followed:

- open the raw .jpeg AFM image

- Image $\rightarrow$ Type $\rightarrow$ 8-bit

- Image $\rightarrow$ Adjust $\rightarrow$ Threshold

- select in black all the desired features on the white substrate

- Analyze $\rightarrow$ Analyze Particles

- select the pixel^2 range within which ImageJ has to count all the black islands. We arbitrarily decided for 9-Infinity range. This selection is a way to rule out from the counting procedure all the noise which is out of that range

- select Show Outlines and mark (or not) the - Exclude on edges - option. Depending on this, islands on the border of the AFM image will be excluded or not. **We made the decision to keep the islands on the border**

2.7   Bibliography

[1] L. Gross, F. Mohn, N. Moll, P. Liljeroth and G. Meyer. *Science*, **325**, 1110 (2009)

[2] M. J. Doktycz, C. J. Sullivan, P. R. Hoyt, D. A. Pelletier, S. Wu and D. P. Allison. *Ultramicroscopy*, **97**, 209 (2003)

[3] T. Schimmel, T. Koch, J. Kuppers and M. Lux-Steiner. *Applied Physics A: Materials Science & Processing*, **68**, 399 (1999)

[4] Y. Sugimoto, P. Pou, M. Abe, P. Jelinek, R. Perez, S. Morita and O. Custance. *Nature*, **446**, 64 (2007)

[5] G. Binnig, H. Rohrer, C. Gerber and E. Weibel. *Physical Review Letters*, **49**, 57 (1982a)

[6] G. Binnig and H. Rohrer. *Helvetica Physica Acta*, **55**, 726 (1982b)

[7] G. Binnig and H. Rohrer. *Surface Science*, **126**, 236 (1983)

[8] G. Binnig, C. F. Quate and C. Gerber. *Physical Review Letters*, **56**, 930 (1986)

[9] 'website Omicron:'. http://omicron.de/en/software-downloads/51

[10] 'website Gwyddion:'. http://gwyddion.net/

[11] 'website ntmdt:'. http://ntmdt.com

[12] I. J. N. *Intermolecular and Surface Forces*. Elsevier (2011)

[13] H. Butt, B. Cappella and M. Kappl. *Surface Science Reports*, **59**, 1 (2005)

[14] G. Friedbacher and H. Fuchs. **71**, 1337 (1999)

[15] A. D. L. Humphris, M. J. Miles and J. K. Hobbs. *Applied Physics Letters*, **86**, 034106 (2005)

[16] R. Garcia and R. Perez. *Surface Science Reports*, **47**, 197 (2002)

[17] R. Garcia. *Amplitude modulation AFM*. Wiley-VCH (2006)

[18] G. Chen, R. Warmack, A. Huang and T. Thundat. *Journal of Applied Physics*, **78**, 1465 (1995)

[19] H. Holscher, U. D. Schwarz and R. Wiesendanger. *Applied Surface Science*,
     140, 344 (1999)

[20] R. Garcia. *Physical Review B*, **60**, 4961 (1999)

[21] A.-L. Barabasi and H. E. Stanley. *Fractal Concepts In Surface Growth*. Cam-
     bridge University Press (1995)

[22] 'website fractalyse:'. http://fractalyse.org/en-home.html

[23] 'Image Processing and Analysis in Java'. http://imagej.nih.gov/ij/

Chapter 3

α-Sexithiophene (6T)

α-Sexithiophene, also known as α-hexathiophene, α-hexathienyl or α-sexithienyl, is an oligothiophene: conjugated organic molecules of different chain length with a five membered sulphur containing aromatic compound as smallest unit. Its chemical formula is $C_{24}H_{14}S_6$. It has a melting temperature of 290°C at normal condition, its chain is typically 2.4 nm long and it belongs to the class of p-type organic semiconductor.
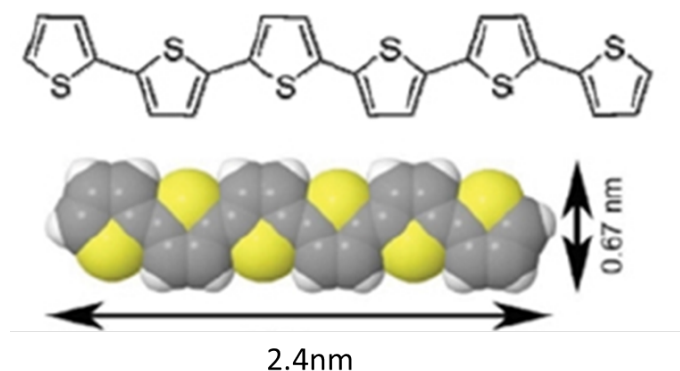

Figure 3.1: 6T molecule representation with its typical dimensions.

6T has been strongly studied as a first organic semiconductor for its rigid-rod behaviour and its morphological properties which brought it to be used for the first OFET employing a small conjugated molecule ([1]). Due to its peculiar self-organization and transport properties it is considered a prototype for studying the physics of molecular devices.

It can be obtained as a pure material and processed as thin film in high vacuum conditions. Its configuration, indeed, has two possible crystalline phases: the thin film and the bulk one. Moulin *etal.* ([2]) saw that the thin film phase evolves with the thickness of the thin film itself. Using X-ray diffraction, the dynamics of formation was followed and the threshold of disappearance of the thin film phase (and the correspondent appearance of the bulk phase), above 6 monolayers, was identified. Indeed, it was found out that the phase that appears for thicknesses superior to 6 MLs (in HV and at a low rate of deposition) shows a periodicity of 2.248 nm which is compatible with 6T molecules tilted by 23°, as is expected for the bulk unit cell proposed by Horowitz ([3]).

Moreover, as investigated by Servet *etal.* ([4]), the thin film phase strongly depends on growth parameters. For instance, Biscarini ([5]) showed roughness scaling properties of 6T thin films as a function of the temperature of the substrate.

Unlike the bulk phase, the thin film phase depends crucially on the underlying substrate. On metal surfaces 6T adsorbs in a so called flat lying orientation with its long molecular axis parallel to the surface, at least in the first layer that, however, acts as a template for further growth. On dielectric surfaces, like silicon oxide, the 6T molecules adsorb in a so called standing orientation with its long molecular axis perpendicular or almost perpendicular to the substrate. Recently, flat lying molecules have been observed also on silicon oxide by several techniques ([6,7]). See Chapter 9 for more details on flat lying molecules.

3.1   Technical details

As written in its datasheet, 6T is not very dangerous but several precautions must be followed when dealing with it, for instance when the crucible has to be refill. 6T can give eye-irritation so proper glasses must be worn. Moreover, a protective mask, gloves and a lab-coat should also be used. Thanks to experience, we can also say that 6T appears as an orange-brown powder which, at the end of its life inside the crucible, after lots of sublimations, tends to be more brown in colour.

Experimentally, the sublimation temperature depends on the amount of 6T inside the crucible and on the crucible itself, since each one has its own heating set up. With our instrumentation, we can report a sublimation temperature ranging from 210°C when the crucible is completely filled, to 290°C when it is almost empty. A bad-behaving flux of molecules, maybe too high or too low, or not increasing with the temperature in the common way, can be taken as a proof that the material inside the crucible is finishing and the crucible must be refill.

Chapter 4

Sample preparation and methods

Native silicon oxide substrate (n-type, phosphorous doped, resistivity 1-10 Ωcm) was manually cut from a wafer properly stocked to avoid any environmental contamination. Then, it was directly put inside the Fast Entry Lock (FEL) of the VT AFM (see Chapter 5) without any chemical treatment.

The substrate was glued to the sample holder with a silver paste in order to have thermal contact even at high temperatures ($< 180°C$). 30 minutes in air, as drying time, are enough to have the substrate properly fixed on the sample holder. During this time, we also put on top of the sample (slightly tilted) a petri in order to partially cover it from dust.

Since small conjugated molecules can be deposited in a much more controlled way than conjugated polymers, their morphology can be better characterized and related to physical properties like grain size and molecular orientation. This is why, for our experiments, alpha-sexithiophene (6T) was chosen as organic semiconductor. Half gram of 6T powder was purchased from SIGMA-ALDRICH (product number: 594687) and half of the Organic Molecular Effusion (OME) cell's crucible was fill with 6T. 5 monolayers of alpha-sexithiophene were sublimated in Ultra High Vacuum (UHV, $\sim 10^{-9}$ mbar) using the OME cell described in Section 5.2, not more than 5ML because of the starting of the bulk phase from there on ([2]). Before the experiment, we followed an outgassing procedure of several hours up to 200°C in order to remove every kind of contaminant.

The typical heating ramp for the substrate, if needed, was chosen in the following way, always waiting one hour after the proper temperature was reached (in order to obtain an homogeneous heating of the whole substrate):

- T(sub)=50°C:
  a Low power was selected in the Temperature Controller-331 (Lake Shore). This allowed to reach 50°C in almost half an hour

- T(sub)> 50°C:
  a Low power, in this case, was found not enough to reach 80°C, 100°C and 120°C. Therefore, to have a slow heating of the substrate as well, we decided to first select low power till 50°C and then increase the power selecting a Medium one till the correct temperature was reached (typically another half an hour)

The heating of the Knudsen cell, instead, was achieved with a Power Supply SM 7020-D (Delta Elektronika). A ramp of not more 1V/minute (see the manual of the instrument) was followed from RT till the proper sublimation temperature was reached. In order to have a smooth heating procedure, for each step, we waited 10 minutes at least to let the temperature stabilize. Since the sublimation temperature was near $270°C$, depending on the amount of material in the crucible, we had to perform ~ 20 steps; this means that the heating procedure took almost 3 hours. Regarding the cooling down procedure, instead, the manual declares a maximum rate of $-10V/min$, and this threshold was respected choosing $-5V/min$.

The flux of molecules was focused on the substrate position thanks to a centering rod, which, once positioned on the final part of OME cell, allowed to see where the molecules reach. **The instrument was not integrated with a Quartz Crystal Balance (QCB)**. Indeed, the flux of molecules was too collimated to have both the substrate and the QCB receiving the material. The only chance was to add to the system a movable QCB, to put in between the flux and the substrate whenever the deposition rate had to be read. Unfortunately, this was not possible, therefore the flux was obtained by AFM, indeed, the time needed for each evaporation was read from a timer and the correspondent coverage calculated from the AFM image by Gwyddion (see Section 2.6).

Since each of the five different substrate temperature experiments had to be done at the same flux of material, an important request to be able to calculate the desorption at each substrate temperature, a calibration at RT was always done before each experiment to obtain the proper sublimation temperature correspondent always to the same low rate of few angstrom/minute. Previous results on desorption of 6T ([8]) were used to get the proper time of deposition. Specifically, we followed this procedure:

- at RT, at a tentative sublimation temperature of almost 250°C, we obtained 4 minutes as the deposition time to have almost 25%ML ($\sim 6A$) of coverage, which was the step-coverage we were looking for. This coverage-time relation corresponds to a rate of $\sim 1A/min$, the desired one, and it was taken as a reference

- since each experiment lasted several hours (see the final part of the paragraph for a quantification), with continuous sublimation, each experiment determined a change in the sublimation temperature for the next experiment. This forced us to repeat a RT calibration before each experiment in order to find always the proper sublimation temperature corresponding to the same flux of few angstrom/minute

- a technical detail had to be faced regarding substrate temperature different from RT. Indeed, due to desorption, an increased amount of AFM images should have been done to reach a total coverage of 5ML. This would have been a problem for two reasons: firstly, the duration of the whole experiment would have increased too much, secondly, there would have been more risk to dirty the tip without being able to conclude the experiment. This is why, we decided to take into account the desorption changing the deposition time and increasing it of an amount equal to the previously estimated percentage of desorption (15% at 50°C, 30% at 80°C and 100°C and 45% at 120°C,[8]). Our results, shown in Section 7.2, do agree with the desorption percentages calculated in ([8])

- a part for the first experiment, performed after a refill of the 6T cell, we did not observe a relevant change in the 6T temperature during the experiment. As already underlined, one experiment was typically 20 hours long, therefore a change (increase) in the 6T sublimation temperature (to be understood by a change in the coverage step measures by AFM images) could be expected. This happened only for the RT experiment since, as noticed even in other experiments, as soon as indeed a little increase in the power of the 6T cell had to be achieved

The Microscope's base pressure was in the range of 10^{-10}mbar at RT (temperature of the effusion cell). During depositions, due to an average temperature over all the experiments of 260°C, the pressure raised of one order of magnitude.

Non contact AFM technique was performed with Nanosensors AFM cantilever (PPP-NCHR-50, n$^+$-silicon, resistivity: 0.01-0.02 Ωcm) with typical resonance frequency of 350kHz. Each 6x6μm^2 AFM image was scanned at a frequency $f = 0.33Hz$ (forward and backward scans), with 600 pixel (1pixel/10nm), therefore each image took 30 minutes.

In conclusion, we can report that each experiment lasted almost 20 hours, indeed:

- $\sim$ 3 hours to heat the Knudsen cell to the proper sublimation temperature

- $\sim$ 2 hours to heat the substrate and let the temperature stabilize

- $\sim$ 2 hours for the deposition (an average deposition time of 5 minutes for 20-25 depositions)

- $\sim$ 12 hours for the AFM images

4.1 Bibliography

[1] G. Horowitz, D. Fichou, X. Peng, Z. Xu, F. Garnier, M. Molrculaires and H. Dunant. *Solid State Communications*, **72**, 381 (1989)

[2] J.-F. Moulin, F. Dinelli, M. Massi, C. Albonetti, R. Kshirsagar and F. Biscarini. *Nucl. Instrum. and Meth. in Phys. Research B*, **246**, 122 (2006)

[3] G. Horowitz, B. Bachet, A. Yassar, P. Lang, F. Demanze, J.-L. Fave and F. Garnier. *Chem. Mater.*, **7**, 1337 (1995)

[4] B. Servet, G. Horowitz, S. Ries, O. Lagorsse, P. Alnot, A. Yassar, F. Deloffre, P. Srivastava, R. Hajlaoui, P. Lang and F. Garnier. *Chemistry of Materials*, **6**, 1809 (1994)

[5] F. Biscarini, P. Samorì, O. Greco and R. Zamboni. *Physical Review Letters*, **1**, 2389 (1997)

[6] M. A. Loi, E. Da Como, F. Dinelli, M. Murgia, R. Zamboni, F. Biscarini and M. Muccini. *Nat. Mat.*, **4**, 81 (2005)

[7] F. Dinelli, C. Albonetti and O. V. Kolosov. *Ultramicroscopy*, **111**, 267 (2011)

[8] A. Straub. *Advanced SPM studies on the growth of ultrathin films of organic semiconductors at metal and dielectric interfaces.* Ph.D. thesis, Alma Mater Studiorum-Universita' di Bologna (2011)

Chapter 5

In-situ AFM: VT AFM XA Series, by Omicron

Following the Variable Temperature (VT) AFM XA Series User's Guide & Service Manual provided by Omicron, we describe the Variable Temperature AFM by Omicron NanoTechnology which we used to perform the in-situ real time studies of 6T growth presented in Chapter 7.
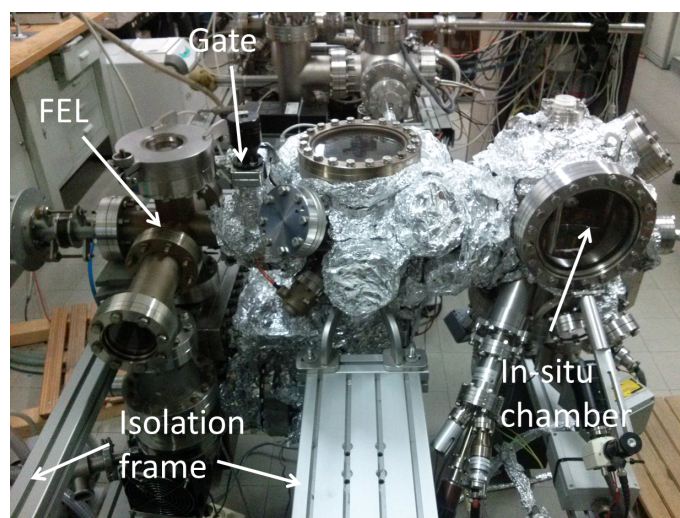

Figure 5.1: A front view of the VT AFM microscope.

This powerful microscope allows both AFM and STM mode and is provided of cooling and heating facilities to cover a temperature ranging from 70 K to 500 K. Two main parts can be seen in Figure 5.1, separated by a gate: the Fast Entry Lock

(FEL) and the in-situ chamber. The FEL is the chamber used to communicate with the ambient and it allows to extract or put old/new samples/SPM tips from the instrument. Due to a primary pump and a turbo pump, the minimum vacuum obtainable in this chamber is an HV. The in-situ chamber, preceded by an intermediate chamber, instead, can reach an UHV due to an ionic pump and a Titanium Sublimation Pump (TSP).

The whole microscope is held up by an isolation frame whose aim is to isolate the system from the environment, cutting external vibration sources which could dramatically change the SPM measurements. The basement elements at the four corners of the whole system are filled by sand to damp acoustic noise. Sand, indeed, is an excellent damping material, due to its granular structure, see Figure 5.2. Moreover, thanks to air cushions it is possible to change the height and the inclination of the whole microscope in order to have it perfectly flat. This is, indeed, an important request to optimize the work of the AFM stage inside the in-situ chamber.
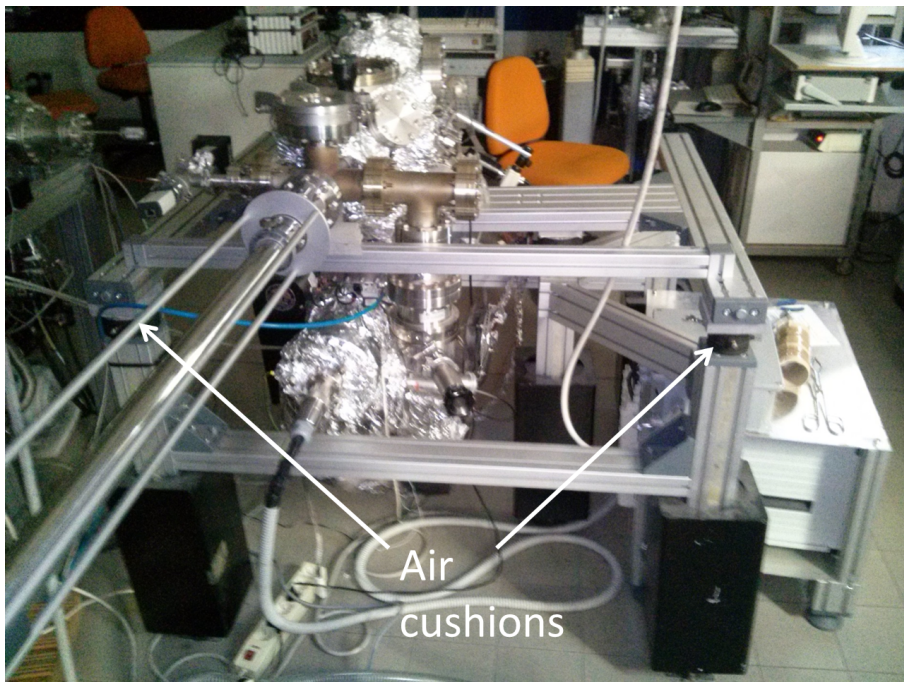

Figure 5.2: A side view of the VT AFM microscope. The isolation frame isolates the whole microscope from external vibrations. The two front air cushions are visible.

5.1 In situ chamber

The in-situ chamber can be seen in Figure 5.3. On the bottom left, the Knudsen cell is visible (see subsection 5.2), while in front one can see the deposition/AFM chamber where molecules are deposited on the substrate and AFM scanning takes place. The AFM stage is inside this chamber, see subsection 5.1.1.

Figure 5.3: The in-situ chamber. The Knudsen cell, on the bottom left part, and the deposition/AFM chamber, in front, are clearly visible.

The heart of the in-situ chamber, where the in-situ (quasi) real time experiment is performed, is shown in Figure 5.4. As one can see the substrate is placed upside-down and the AFM tip can scan from the bottom. **If we scan during deposition, a true real time investigation, we would dirty the tip without being able to conclude the experiment. To avoid shadow effects, then, a quasi real time technique had to be followed**. This simple technique is made up of two steps: the deposition and the AFM scanning. In the first step, the deposition is realized with the tip detached from the substrate. The tip should not be too far
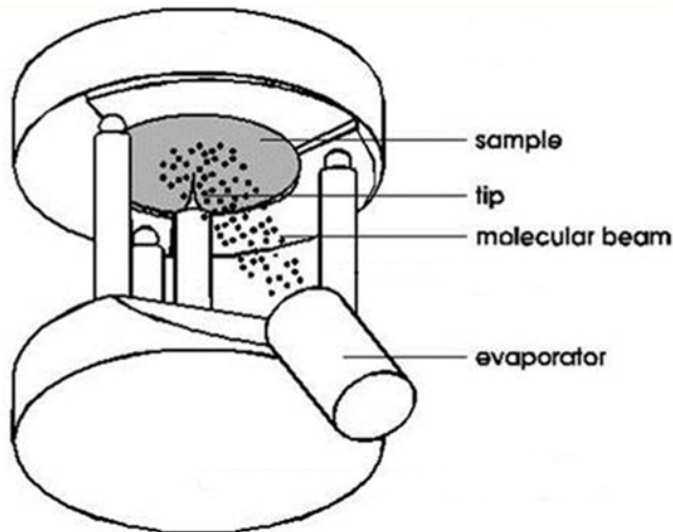
Figure 5.4: Picture of the hearth of the in-situ chamber.

and not too close to the sample. Not too close otherwise we would have the shadow effect, not too far otherwise, after the deposition, we would not be able to approach always the same exact zone. For our experiment, indeed, it is mandatory to scan always the same region of the sample in order to probe, in-situ, the morphological evolution of the same region of the ultra thin film. In our case, we experienced that 50 steps of detaching in the remote box, did not alter the scan region. These 50 steps are almost equal to 500 nm.

The second step, instead, is the AFM scanning which can be achieved in the standard way.
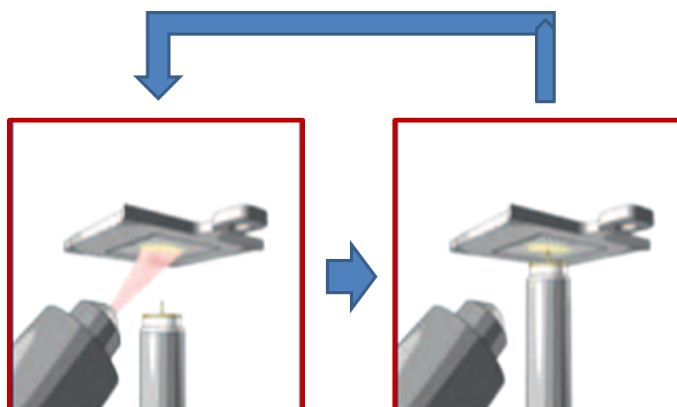
Figure 5.5: The quasi real time technique procedure.

5.1.1 AFM stage: technical description

A view of the AFM stage is shown in Figure 5.6:
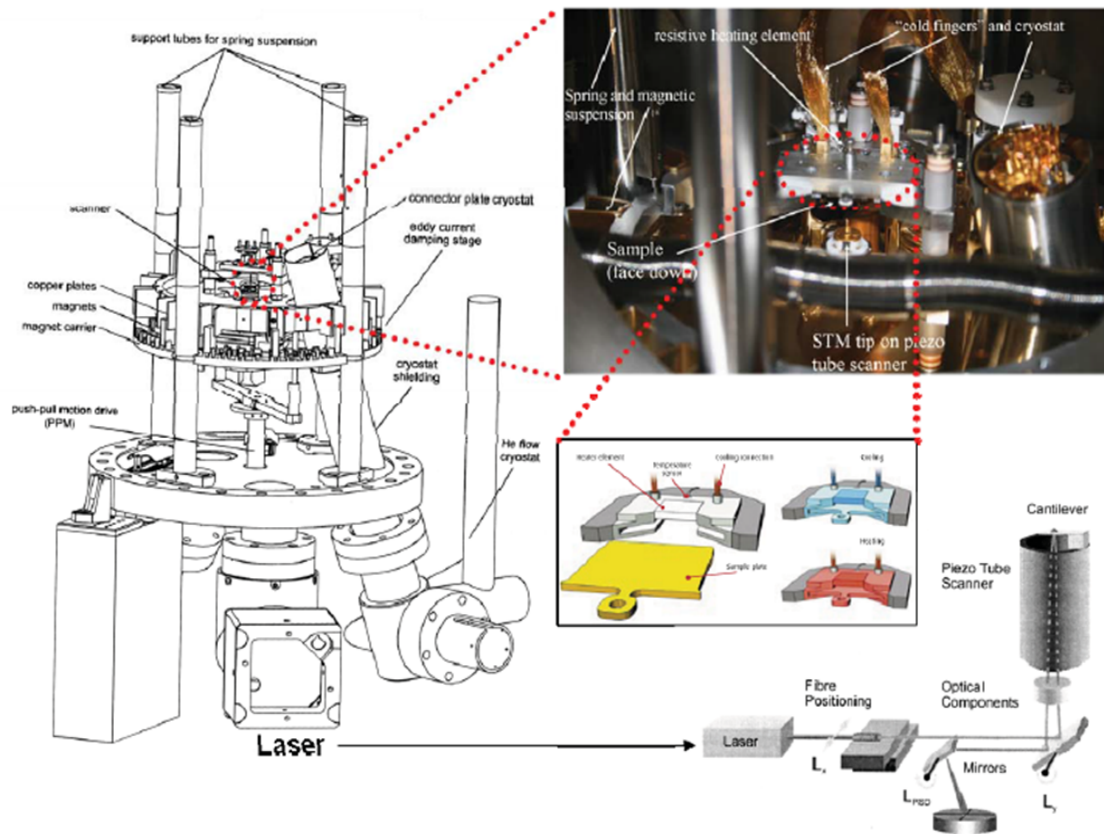
Figure 5.6: Internal layout of the VT AFM showing the two stage vibration isolation system, a magnification of the measurement stage, heating/cooling facility and optical pathway for the compact AFM design.

Here one can find some relevant technical details:

- Spring suspension:
  the microscope is equipped with a high quality vibration decoupling system essential for high resolution scanning probe microscopy. Its base plate is suspended by four soft springs which are protected by columns. Vibrations of the suspension system are intercepted using a nearly non periodic eddy current damping mechanism. For this the microscope base plate is surrounded by a ring of copper plates which come down between permanent magnets.

The spring suspension system can be blocked to allow tip or sample exchange, blocking is achieved using a push-pull motion (PPM) feedthrough, see Figure 5.6. During every scan and deposition, instead, it should be kept floating. By experience, indeed, we noticed that the procedure to block the spring suspension system, during an experiment, can shift the scanning zone of more than 5 μm which is a common scan size. This means that if an in-situ real time SPM experiment has to be carried on, always scanning the same zone, the spring suspension system should not be closed after each scan and then opened after the deposition because this would dramatically change the scan region

- Scanner:
  the microscope uses a single tube scanner with a z-resolution of better than 0.01 nm. Here one can find the specification:

Maximum voltages for x, y and z	± 130 V at T< 40°C
Maximum scan range x,y	nominal $10\mu m$ x $10\mu m$
Maximum scan range z	1.5 μm
Piezo sensitivities x and y	18 nm/V
Piezo sensitivity z	10 nm/V
Piezo capacity	7.5 nF, including the cable in UHV

The shown scanner sensitivities are valid for atomic resolution dimensions only.

- Coarse Motion Drive:

X travel	± 5 mm
Y travel	± 5 mm
Z travel	10 mm
Capacity	1.7 nF

5.1.2   Non contact mode AFM

All the AFM images achieved during the in situ real time experiments described in Chapter 7 were obtained in UHV in non contact mode. In AFM non contact mode, the feedback source is the force gradient measured as the

frequency shift of the cantilever resonance. This frequency shift can be used as feedback signal for a distance regulation z-loop.

In ([1]) one can find:

$$\frac{\Delta f}{f_0} \sim \frac{1}{2k_0}\sqrt{\frac{4k_0 kTB}{2\pi f_0 QA^2}} \tag{5.1}$$

where $B = FM$ detector bandwidth ($\sim 2kHz$) and A = cantilever oscillation amplitude.

As the frequency resolution depends on the Q value, non contact AFM mode is particularly interesting in vacuum. The pressure which can be obtained by pumping the instrument with a turbo pump is sufficient to achieve high enough Q values for a good frequency resolution.

Below one can find the AFM non contact mode function principle.

Regarding the feedback unit, the main part of Figure 5.7 is the *df* Detection unit which uses an intermediate frequency method for frequency evaluation. Specifically:

- the df detection unit generates an output voltage:
  df = -5 mV/Hz (f_{ref} - $f_{cantilever}$ - 455 kHz), where
  f_{ref} = the reference frequency
  $f_{cantilever}$ = the reference frequency of the sensor

- the software df meter shows the frequency deviation corresponding to this voltage. For frequency deviations bigger than 1.5 kHz the frequency detector can no longer work correctly

- in order to adjust *df* ~ 0 for a non interacting cantilever, the reference frequency must reach the value $f_{ref} = f_{cantilever} + 455$ kHz. **This is operationally done, in Matrix ([2]) before the approach of the tip to the sample, with the option: Auto: $\Delta f \to 0$.**
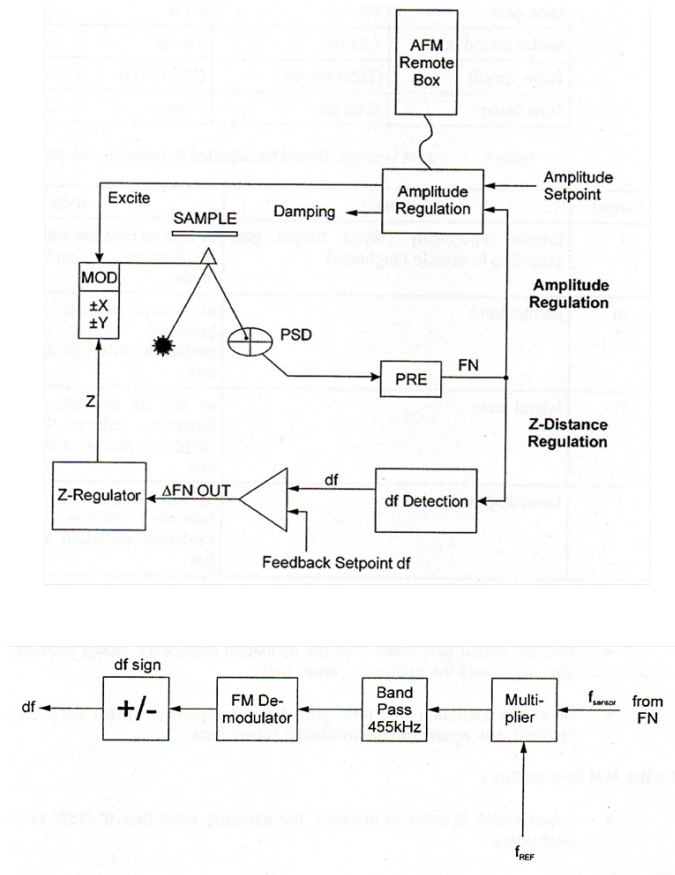
Figure 5.7: VT AFM non contact mode function principle and scheme of the df detection unit.

5.1.3   AFM tips, mounting and fabrication

In order to use cantilevers in UHV conditions, cantilevers must be mounted to the Omicron glueing device using vacuum compatible epoxy cement. The proper procedure is described in the VT AFM XA User's Guide & Service Manual, provided by Omicron, here we will report only the main points.

First the tip holder must be positioned on the Omicron glueing device (Figure 5.8). Then, the cantilever has to be roughly glued on the base of the tip holder with epoxy cement. Before drying in the oven the epoxy, one has to put the cantilever exactly in the proper place which is established by a crosshair on the Omicron glueing device, see Figure 5.8. The precise positioning procedure using an optical microscope guarantees that the laser hits properly the reflective backside of the cantilever and that we obtain the maximal detector signal. Figure 5.8 further shows the designated grooving on the tip holder to be filled with UHV epoxy. Once this is done, one can bake for 20 minutes inside an oven at 120° C the whole Omicron glueing

device, in order, then, to put the tip holder immediately inside the microscope's FEL.
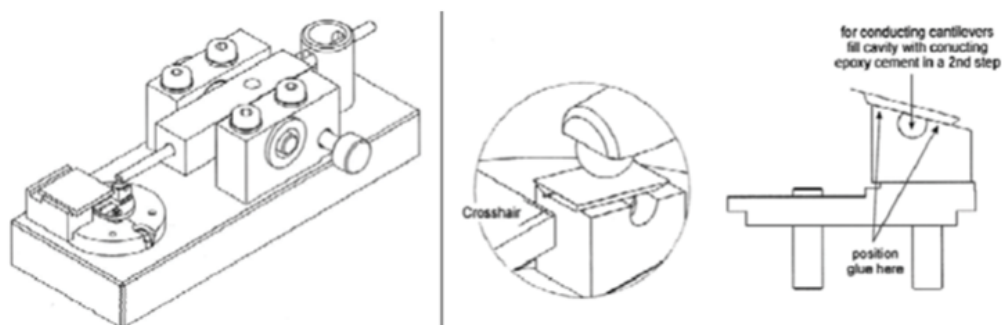

Figure 5.8: (left) Omicron glueing device. (right) Tip positioning and glueing procedure.

5.2 Organic material effusion cell

The main purpose of the organic material effusion (OME) cell with integrated water cooling (Dr. Eberl MBE-Komponenten GmbH, ([3])) is the controlled evaporation or sublimation of suitable materials from the crucible inside the cell within a vacuum chamber under high or ultra-high vacuum conditions (pressures below 10^{-5}mbar).

Technical description

The OME-cell is developed for accurate evaporation or sublimation of high vapour pressure materials like small organics molecules. Therefore the OME-cell is optimized for temperature operation from room temperature (RT) up to 300°C.

The basic features of the OME-cell are shown in Figure 5.9:

As can be seen, a manual rotary (360°) shutter feedthrough (8) can be used to open or close a shutter plate (1). Very important are also connectors (5) for cooling water supply. A picture of the crucible top orifice (2) is shown in Figure 5.10 where one can see that the molecules exit the orifice with a typical angle of 5°, which means that, being the distance orifice-substrate 12 cm, more or less 1 cm of substrate can
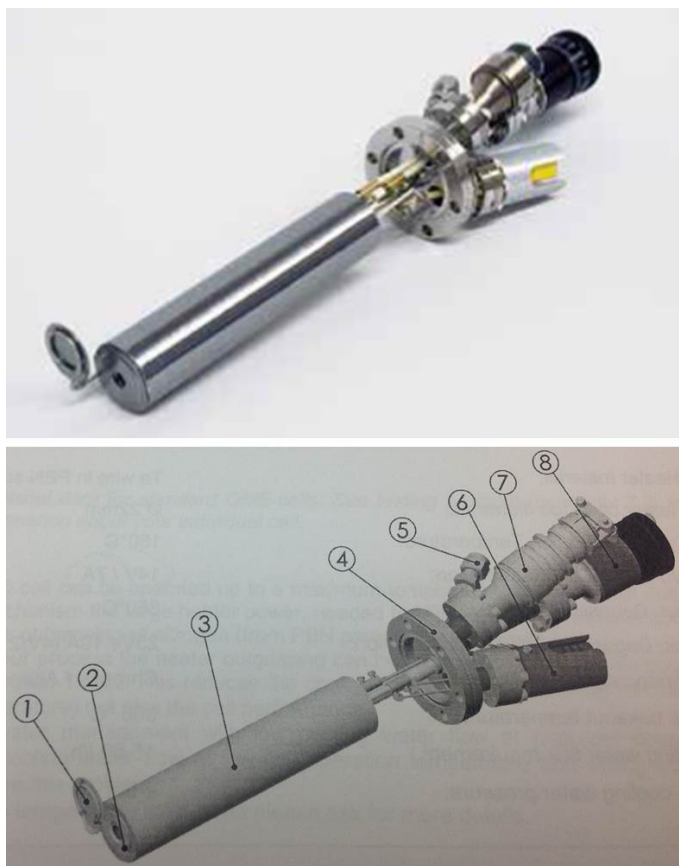
Figure 5.9: Main parts of the organic material effusion cell: (1) shutter plate, (2) crucible top orifice, (3) heat reservoir with crucible and encapsulated heater inside, (4) flange, (5) connectors for cooling water supply, (6) thermocouple connector, (7) power connector, (8) manual rotary shutter feedthrough.

be covered by the flux of molecules. This, indeed, was the typical dimension of our substrates.
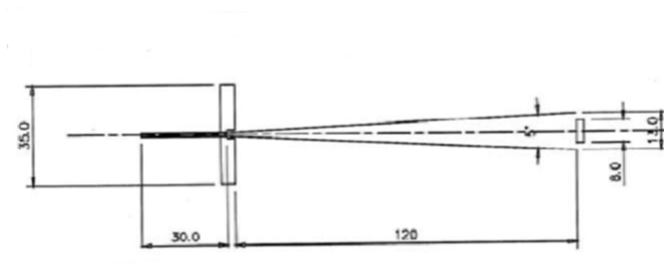

Figure 5.10: Picture of the crucible top orifice with the typical distances involved.

A schematic of the internal construction of the OME-cell, point number (3), is shown in Figure 5.11. This OME cell can achieve a stable temperatures control. This concept also involves a liquid metal used as a thermal conductor that provides direct thermal connection between crucible and heat reservoir without isolating voids. This excellent thermal contact also guarantees a very uniform temperature distribution within the crucible.
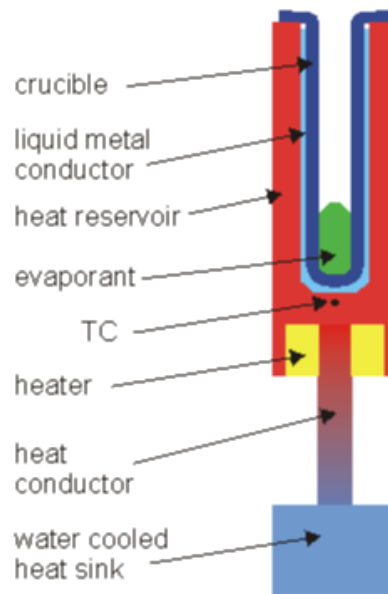

Figure 5.11: Schematic of the internal part of the OME-cell.

5.3 In-situ experiment technical details

In order to perform our experiments in UHV we used the following pumps in serie:

- primary pump: from atmospheric pressure to $\sim 10^{-2} mbar$

- turbo pump: from $\sim 10^{-2} mbar$ to $\sim 10^{-7} mbar$

- ionic pump: from $\sim 10^{-7} mbar$ to $\sim 10^{-9} mbar$

- titanium sublimation pump (TSP): from $\sim 10^{-9} mbar$ to $\sim 10^{-10} mbar$

The base pressure during our experiments, inside the in-situ chamber, was $2x10^{-10} mbar$.

As underlined in the VT AFM manual, after switching on the laser we always waited at least half an hour before scanning. These allows the laser to stabilize.

Each time we did an experiment at a substrate temperature different from RT, we always waited at least one hour before scanning to let the sample-tip system reach thermal equilibrium. Indeed, we waited with the AFM tip already close to the substrate and ready to approach.

Moreover, each time we reached the proper sublimation temperature T, we waited almost 20 minutes to let the temperature stabilize.

Here, one can find a basic guide to perform the whole experiment:

- the substrate was cut from the proper wafer and glued to the sample holder waiting 30 minutes in order to let the paste get dry

- the substrate was put inside the FEL of the microscope, previously left in air

- the FEL was pump, firstly with a primary pump and then with a turbo pump in serie, in order to reach a HV

- once the FEL has reached it minimum vacuum, usually $5x10^{-7} mbar$, the transfer to the in-situ chamber of the sample can be done. (Since the base pressure in the in-situ chamber is $10^{-10} mbar$ the best vacuum in the FEL the minimum pressure difference will be there). The transfer should be done with proper care in order not to move the sample holder from its place

- once reached the in-situ chamber with the vacuum manipulator, with the wobble stick one has to take the sample holder and place it in the proper place in the AFM stage, see subsection 5.1.1. Also this transfer should be done with great care and the sample holder should be positioned inside the AFM stage proper place without pushing, but slightly moving the sample holder in a "zig-zag" way. This procedure should be followed also when unloading the AFM stage place with the sample holder

- now one can do an approach of the cantilever to the sample by eye. The key is to get as close as possible to the sample until the reflex of the tip can be seen on the sample itself. The use of a light can help to see better the reflex
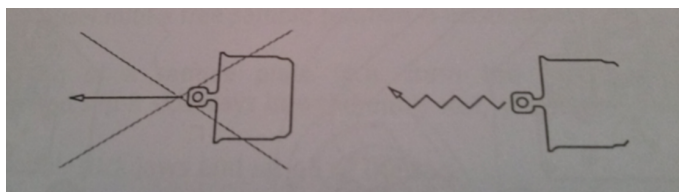
Figure 5.12: "Zig-zag" way to load and unload the sample holder from the AFM stage place.

- the heating of the substrate can now be achieved, if needed, with the Power Supply SM 7020-D (Delta Elektronika). The basic connections can be found in Figure 5.13
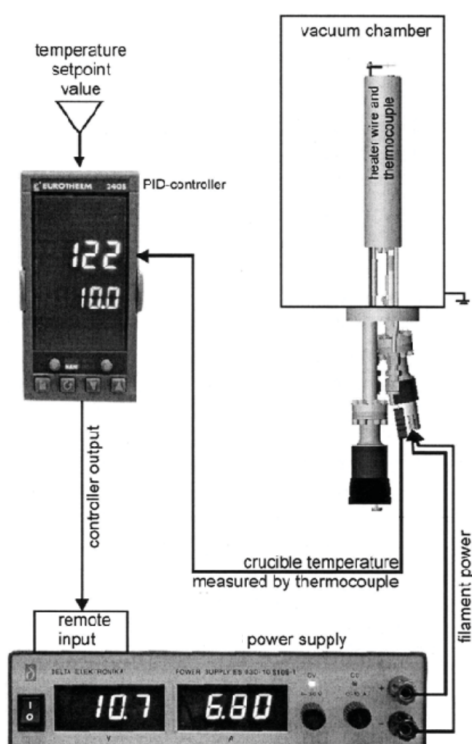

Figure 5.13: Power Supply and the connections to the OME cell and the PID controller.

- once the tip is close to the sample the electronic approach should be done with

Matrix software. By experience, a gain of 25% and a set point of -35 Hz were good choices to obtain the approach in few minutes. Rarely it happened the approach not to be possible. Changing the sample region was always found to be a good way to have the next approach properly done. Follow the VT AFM XA User's Guide & Service Manual to have more detail on the approach procedure

- once the approach has been successfully done, one can center the laser onto the cantilever using the remote box, until an Intensity (in Matrix) between 2.3 V and 2.5 V is reached

- now the oscillation amplitude of the cantilever's driving force can be selected in Matrix ($A - vib$ parameter). Since we performed non contat AFM images, we decided for a small voltage, specifically, always 0.1V

- as described in subsection 5.1.2, $df \rightarrow 0$ should be pressed in Matrix

- finally, the scanning parameter can be selected: gain (typically 10%), set point (typically -30 Hz), points (i.e. pixels), scan speed (the scanning time between two consecutive pixels, typically 2000-2500-3000 μs) and **scan range, in our case, always 6x6 μm^2, a good compromise between a nominal max scan dimension of 10 μm, in reality 7 μm, and the need to have a statistical number of 6T islands for each experiment**

- now the AFM scan can be performed

Chapter 6

Ex-situ AFM: NT-MDT Smena

NT-MDT ([4]) Smena was the ex-situ AFM microscope used to perform the P5-C60 AFM images shown in Chapter 8.

Like the VT AFM microscope described in chapter 5, a spring isolation frame is present to cut all the external noise which could affect the AFM scanning. Moreover, an optical microscope is visible in Figure 6.1: this was used to properly align the laser onto the cantilever and to scan specific parts of the sample which, by eyes, it would not be possible to select.

6.1 Design

The general view of Smena Measurement Head (MH) is shown in Figure 6.2. Base (1) is installed on three adjustable supports (2 a,b). The base accommodates a scanner (3) with a probe holder (4), a tracking and detection device (5 a,b) and an electronic circuit board (6). The cantilever is installed in the holder (4).

- Supports:
  Adjustable height supports (2a,b) are used for setting up the horizontal and height position of MH with regard to the analyzed sample. The tip and the sample should be as much as possible perpendicular between them and this is achieved manually selecting the three height supports. **A too big tilting angle between the tip and the sample can strongly affect the quality of the AFM image**. The rear support (2b) is used for approaching the probe
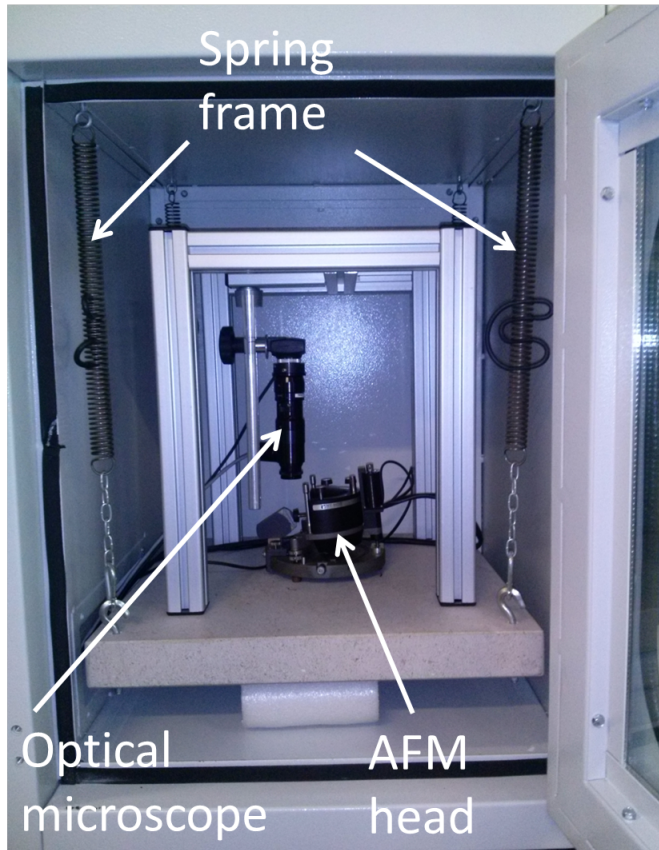
Figure 6.1: The NT-MDT Smena Measurement Head, the spring isolation frame and the optical microscope.
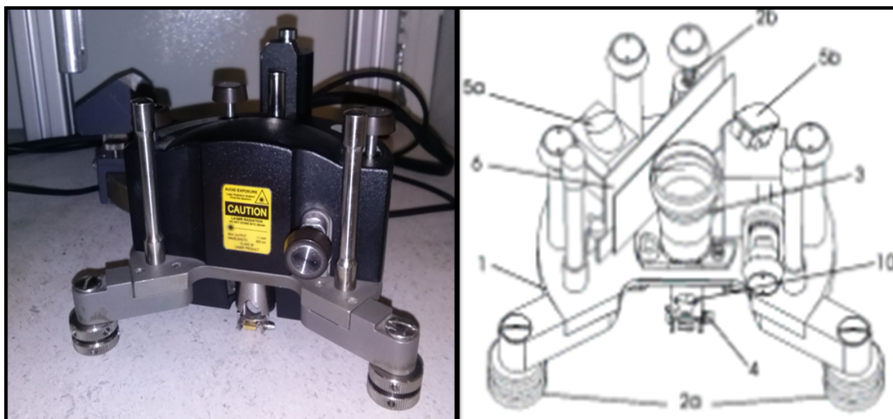

Figure 6.2: Main parts of the Smena Measurement Head.

to the sample by changing the inclination of the head. This is a 0.35 mm pitch thread screw. Rotation of this screw by 1° results in changing the cantilever vertical position with regard to the sample by 0.3 microns, this allows an easy

manual approach of the probe

- Scanner:

  The scanner is designed for the probe movement in direction x,y and z. It consists of 2 concentric piezotubes, one of which is inserted into the other, the tubes are connected at one end. The outer tube ensures the probe displacement along axis z, the inner tube provides for movement in plane x-y. The free end of the inner piezotube has the cantilever holder and scanning mirror attached to it. This mirror is the primary sensing device of the cantilever laser tracking system

- Cantilever holder:

  This is a spring clamp. **It also contains a piezodrive exciting the cantilever oscillations**

- Tracking and detection device:

  This device incorporates a laser with focusing lens, mirror system and a photodetector with a magnifying glass, see Figure 6.3:
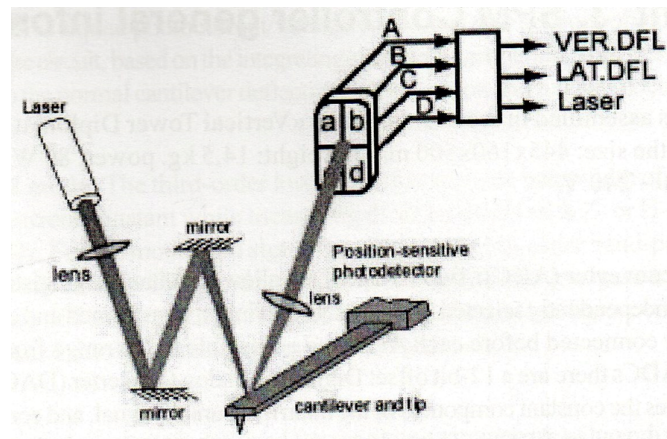

Figure 6.3: Tracking and detection device.

To conclude, here one can find the performance parameters of the NT-MDT Smena Meassurement Head:

Scanning range	90x90x5 μm
Minimum scanning step	0.01 nm
Sample size	unlimited
Overall dimension	115x130x100 mm
Weight	0.7 kg

6.2 Bibliography

[1] S. Morita, R. Wiesendanger and E. Meyer. *Noncontact Atomic Force Microscopy.* Springer (2002)

[2] 'website Matrix:'. http://omicron.de/en/software-downloads/51

[3] 'website OME cell:'. http://mbe-komponenten.de/products/mbe-components/effusion-cells/ome.php

[4] 'website ntmdt:'. http://ntmdt.com

Chapter 7

In-situ real time AFM studies of organic semiconductor growth on silicon oxide

In-situ and real time techniques are increasingly getting accessible to the scientific community and allow unprecedent insights into complex dynamic physical, chemical and biological processes that can not be simply unravelled by common ex-situ measurements. Many technically relevant molecular scale systems, like, for example, the growth of organic semiconductors by Organic Molecular Beam Deposition (OMBD) in Ultra High Vacuum (UHV), are out of equilibrium processes that need to be better understood in order to achieve a reproducible and reliable downscaling of micro and nano electronic devices.

In-situ real time investigation methods that have been so far reported and were applied to investigate dynamic processes involve X-ray scattering, AFM in liquid, photoelectron spectroscopy, X-ray adsorption spectroscopy and electrical characterization of OFETs ([1]).

Surface sensitive diffraction techniques, for instance, provide reciprocal space information on structure, most often Fourier type transforms of adspecies pair correlations for sub-monolayer systems, or height-height difference correlations for multilayer growth. An advantage of these techniques is that they can be performed in-situ during deposition, they automatically provide statistical or ensemble averages over large areas, and they probe both short and long range order.

Scanning Probe Microscopy (SPM) techniques applied to in-situ real time experiments are of particular interest since they provide a real space insight into dynamic processes at surfaces in localized areas down to the nanometer scale. Furthermore, SPM techniques are complementary to the above mentioned in-situ real time tech-

niques that average the measurements observable over larger areas.

The only SPM technique that has so far been applied to elucidate the dynamics of growth phenomena in UHV uses a custom built STM ([2]) combined with Molecular Beam Epitaxy (MBE), however the group's investigations concentrate on the growth of inorganic semiconductors.

So far, the most prominent example of a real space in-situ real time investigation on the growth evolution of an organic semiconductor employed photoelectron emission spectroscopy to study the growth of pentacene on silicon oxide ([3]).

The present work is to our knowledge the first in-situ real time AFM study of the growth process of organic semiconductors during deposition.

7.1   Experimental details

The in-situ real time experiments were achieved using the VT AFM XA series microscope described in Chapter 5. This microscope is also equipped with an Organic Molecular Effusion (OME) cell which allows depositions at a controllable rate of molecules. The OME cell is described in Section 5.2. For all the details regarding materials and methods, refer to Chapter 3.

The idea of the experiments is to perform, in a step-wise manner, depositions of 6T on native silicon oxide at different substrate temperature in order to probe, in-situ real time, the morphological evolution of the organic semiconductor and to obtain temperature dependent morphological parameters, like desorption energy, diffusion energy and the Ehrlich-Schwoebel barrier. The chosen temperatures are: RT, 50°C, 80°C, 100°C and 120°C.

Experimentally, for each temperature, we deposited 5ML of 6T (not more otherwise the 6T bulk phase would start ([4])) in steps of almost 0.25 ML ($\sim 6A$). This coverage step was chosen to have at least three-four clear images for each layer, an important point to be able to have a significant number of measurements describing the evolution of the morphology. After each deposition, following the quasi real time microscopy technique described in Section 5.1, we achieved one non contact AFM image (in UHV), obtaining, in the end, a movie of 20-25 AFM images of the same region, showing the local morphological evolution of the ultra thin film from the bare substrate, to the early stages of growth, to the percolation and then up to the fifth layer.

7.2   Results and data analysis

In Figure 7.1-7.2 and 7.3-7.4, we show the morphological evolution of the 6T ultrathin film at two extremes, 50°C and 100°C, up to the fourth layer (we did not put RT and 120°C degrees because, the first was characterized by a morphology presenting crystals while, the second, by dewetting phenomena, see Section 7.16). All the remaining AFM images can be checked as supporting online material:

https://www.dropbox.com/home/In-situ_real_time_experiment
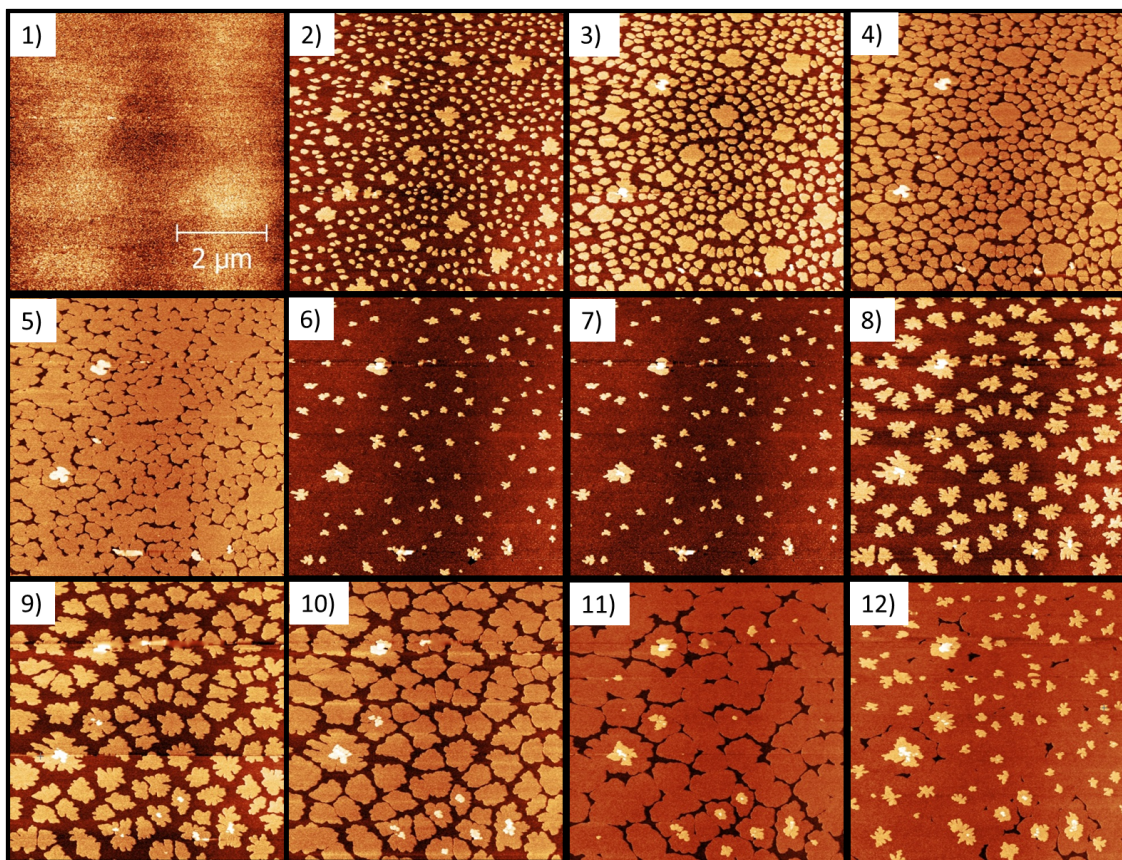
Figure 7.1: Morphological evolution of the 6T thin film on native silicon oxide at 50°C. 1) bare substrate 2) 0.27ML 3) 0.48ML 4) 0.74ML 5) 0.92ML 6) 1.06ML 7) 1.30ML 8) 1.52ML 9) 1.72ML 10) 1.93ML 11) 2.12ML 12) 2.35ML
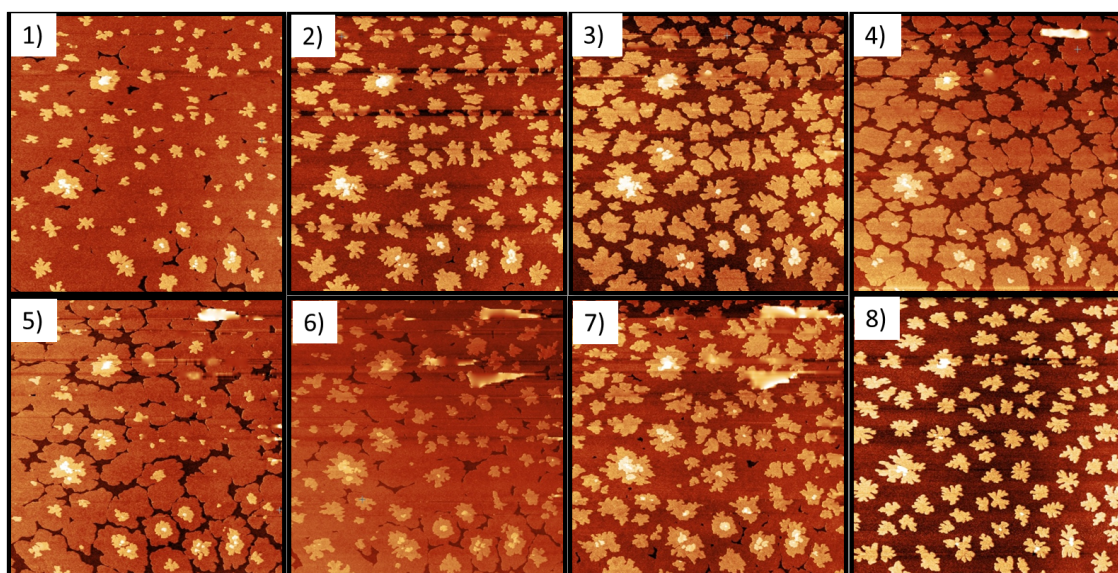
Figure 7.2: Morphological evolution of the 6T thin film on native silicon oxide at 50°C. 1) 2.35ML 2) 2.56ML 3) 2.76ML 4) 2.99ML 5) 3.17ML 6) 3.45ML 7) 3.62ML 8) 3.84ML
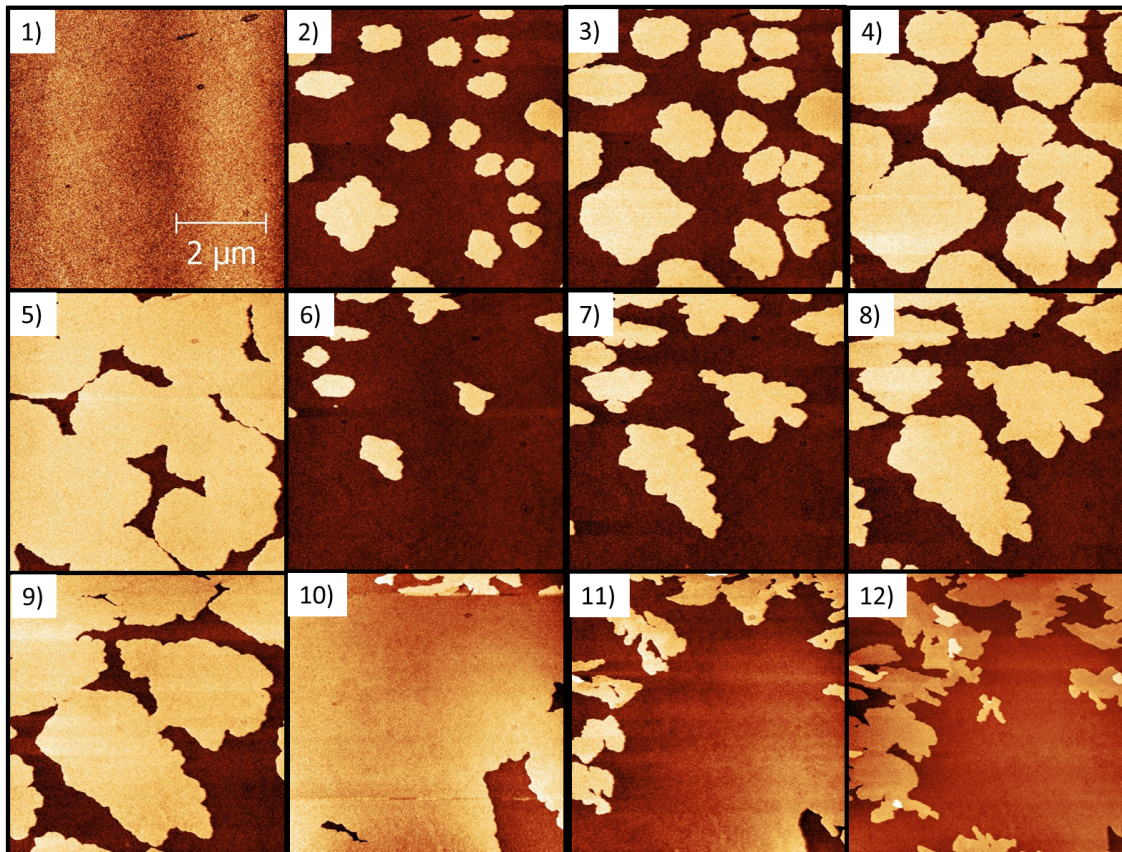
Figure 7.3: Morphological evolution of the 6T thin film on native silicon oxide at 100°C. 1) bare substrate 2) 0.22ML 3) 0.45ML 4) 0.68ML 5) 0.89ML 6) 1.08ML 7) 1.26ML 8) 1.46ML 9) 1.68ML 10) 1.96ML 11) 2.17ML 12) 2.36ML
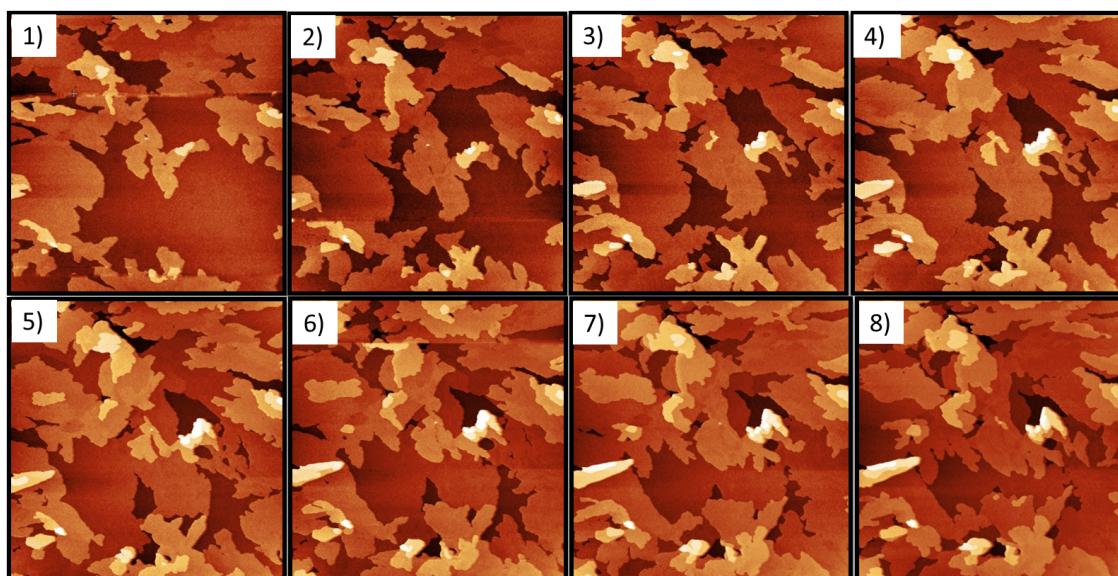
Figure 7.4: Morphological evolution of the 6T thin film on native silicon oxide at 100°C. 1) 2.57ML 2) 2.92ML 3) 3.17ML 4) 3.38ML 5) 3.59ML 6) 3.79ML 7) 4.07ML 8) 4.26ML

Several observation can be done:

1. in both cases, two distinct populations of 6T islands are clearly visible. One distribution has a lower nucleation density but it is characterized by bigger islands, the second one, instead, deals with a higher density population of smaller islands. This effect is due to the shutter of the OME cell (see Section 5.2), which, when closed, actually does not completely close the cell allowing a low flux of molecules to reach the substrate. These molecules are the one forming the low density population of clusters (bigger in size), the other distribution of islands, instead, is the proper one obtained opening the shutter of the OME cell. Following Section 1.2.4 again, this behaviour is in agreement with thin film growth theory in the aggregation regime where, the average island size $< s >$, is inversely related to the flux of molecules

2. at a first glance, the nucleation density is different in the two cases, bigger at 50°C, smaller at 100°C. This is in agreement with thin film growth theory in the aggregation regime, where the nucleation density is related to the exponential of $1/T$ (see Section 1.2.4)

3. in both cases, at 50°C and 100°C, the initial growth (*viz.* $\theta \leq 2ML$) is layer by layer (Figures 7.1 and 7.3): indeed, the second layer coverage, when the first one is completed, is almost negligible and the same holds true for the third layer when the second one is going to be complete. In other words, the nucleation of the second and third layers only starts when the previous layers have been completed. This means that in this growth-thermodynamics condition, the supersaturation is bigger than two times the critical value $\Delta\mu_{cr}$, see subsection 1.2.3. On the other hand, when we observe Figures 7.2 and 7.4, we are in front of a 3D growth: the thin film appears clearly rougher. This is due to a roughening transition ([5]) which is more pronounced at 100°C where the film is even more rougher than at 50°C.
   In conclusion, the total growth mechanism is 2D+3D with a roughening transition at the third layer

4. we notice a drop of the nucleation density from the first layer nucleation to the second and third ones (always in the aggregation regime, i.e. $\theta \sim 0.2ML$). This effect is due to the different nature of the nucleation substrate: silicon oxide for the first layer, 6T for the second and third layer

5. a shape transition for 6T islands can be noticed comparing the one of 6T islands on silicon oxide and the one of 6T islands onto 6T islands. The former

is roundish while the latter is more dendritic or fractal ([6])

6. another shape transition can be seen comparing the evolution of islands of the same layer from small coverages up to coalescence and percolation. The starting islands are always more dendritic then the final ones, which are more roundish

7.2.1   Experimental desorption energy

As described in subsection 7.5, in case of desorption the relation between the total measured flux and the substrate temperature is the following:

$$\Phi(T) \sim exp(E_{des}/kT) \tag{7.1}$$

For the case of our experiments, five different fluxes can be measured, corresponding to five different temperatures and this is enough to obtain a trend. If, indeed, we plot $\ln(\Phi(T)$ vs. $1/T$, the slope will be E_{des}/k, a value from which the desorption energy can be extrapolated.

To start with, then, here on the left of Figure 7.5 we report the behaviour of the total coverage with respect to deposition time, for the five experiments, from which the fluxes can be obtained. As can be seen RT has the biggest flux of molecules, due to no desorption, while the others, necessarily, yield a smaller flux, minimum for 120°C. Regarding this last experiment, as will be shown in Section 7.16, dewetting phenomena taking place from the first layer determined difficulties in estimated the layer occupancies. This is why in the plot only the very first points have been taken into account.

On the right of Figure 7.5, instead, the plot of $ln\Phi(T)$ vs. $1/T$ is reported: from the slope a desorption energy of $E_{des} = (21 \pm 5)meV$ is found. As an error bar on the desorption energy the error on the linear fit has been considered.

This value is partially in agreement with the previous one ([7]), $E_{des} = (52 \pm 5)meV$. The discrepancy (our calculation is half of that), maybe, is due to our 80°C and 100°C experiments, which show a smaller flux of molecules at 80°C instead that at 100°C. Also in the right plot of Figure 7.5, the 100°C value seems to be out of trend. We did not understand why this happened, anyway, the order of magnitude of the two estimations, is the same, so we consider our value reasonable. We also calculated the desorption energy without taking in to account the 100°C point, obtaining $E_{des} = (24 \pm 1)meV$. As can be seen, the measure is more precise but slightly bigger.
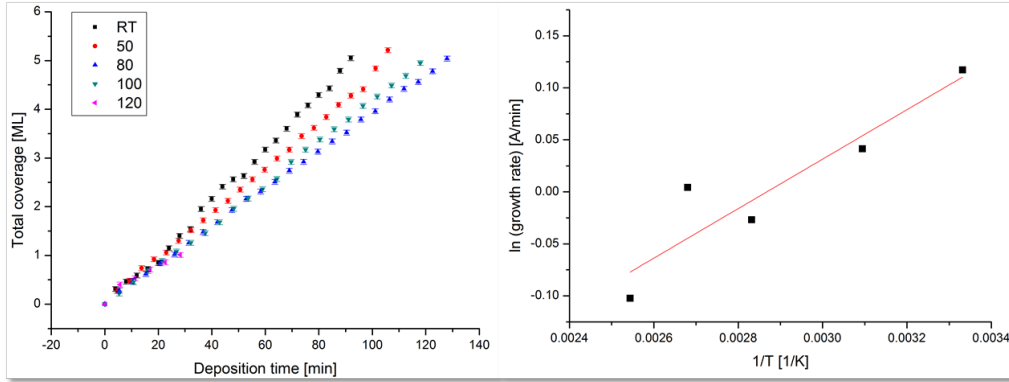
Figure 7.5: (left) Total coverage monitored after each growth step vs. time. (right) Desorption energy plot yielding, from the slope, $E_{des} = (21 \pm 5)meV$.

7.2.2 Experimental growth energies

As can be seen by Figure 7.6, we want to compare the island density at (approximately, due to experimental reasons, i.e. absence of QCB) the same coverage but different temperature of the substrate. In order to be in the aggregation regime we select the AFM images referring to a coverage of $\sim 0.3ML$. As described in subsection 1.2.4, since the flux of molecules was the same for each different experiment, a plot of $\ln(n)$ vs. $1/T$, yields the energy E driving the growth.
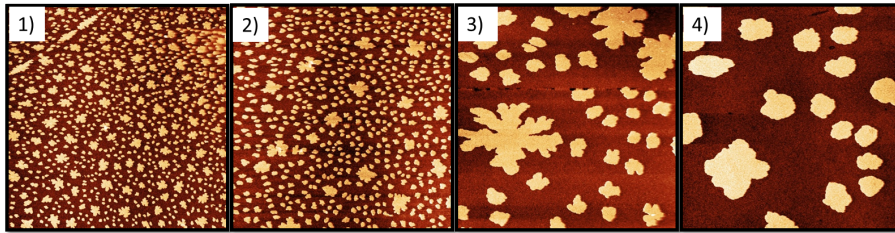

Figure 7.6: Different first layer island density for approximately the same coverage but different substrate temperature. 1)RT, $\theta = 0.3ML$ 2)50°C, $\theta = 0.27ML$ 3)80°C, $\theta = 0.28ML$ 4)100°C, $\theta = 0.22ML$

In Figure 7.7, all the measured island density are plot with respect to the substrate temperature, left graph, while on the right the plot yielding the E_1, the relevant energy parameter for the first layer, is reported. From the slope one can obtain
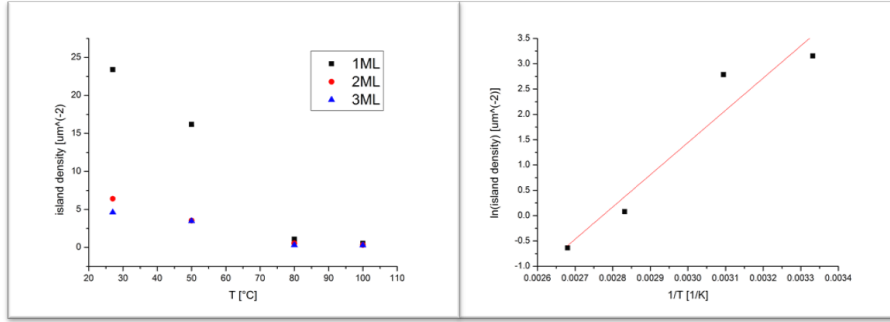
Figure 7.7: (left) Island density vs. temperature. A clear decrease is visible. (right) $\ln(island\ density)vs.(1/T)$ plot: the slope yields the energetic of the growth.

$E_1 = (548 \pm 110)meV = (0.5 \pm 0.1)eV$, where the error bar is the one given by the linear fit.

The same procedure applied to the second layer and the third layer (not the fourth and the fifth due to 3D growth) gives: $E_2 = (430 \pm 60)meV = (0.43 \pm 0.06)eV$ and $E_3 = (429 \pm 105)meV = (0.4 \pm 0.1)eV$.

Once these energy values are known, it is possible to gain knowledge about the diffusion energy. Indeed, if we make the hypothesis to be in the complete condensation regime of the aggregation's one, where desorption is negligible (actually, this is not true for our situation, since the desorption energy was calculated to be 21 meV. However, since E is one full order of magnitude bigger, we can, as a first approximation, rule out the desorption contribution), then we can claim, see subsection 1.2.4:

$$E = \frac{i^* E_{dif} + E_b}{i^* + 2} \tag{7.2}$$

which means

$$E_{dif} = \frac{i^* + 2}{i^*} E - \frac{1}{i^*} E_b \tag{7.3}$$

From this expression, in this regime, once the critical nucleus size and the binding energy of the critical cluster are known, the diffusion energy can be calculated.

Moreover, another observation regarding growth energies can be done, taking into account how the island density change, at the same substrate temperature and flux, when we focus on (approximately) the same coverage (in the aggregation regime) but different layers. For instance, in Figure 7.8 it is shown the situation at 50°C.

This change in the substrate will affect the binding energy E_{i^*} (see subsection
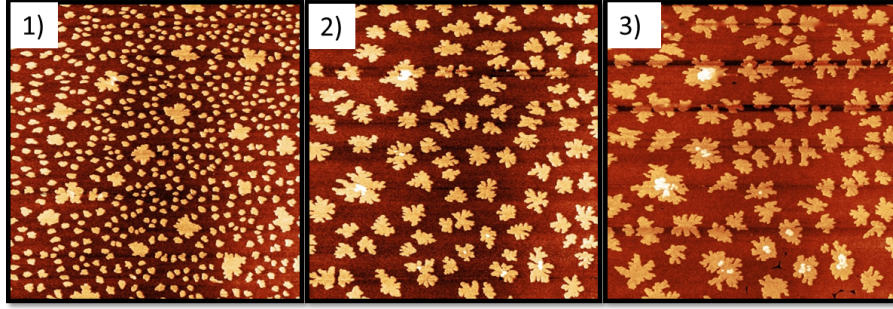
Figure 7.8: Change of the island density at (approximately) the same coverage, the same flux and temperature (50°C), but different layer: 1)1st monolayer: $\theta_1 = 0.27ML$ 2)2nd monolayer $\theta_2 = 0.30ML$ 3) 3rd monolayer $\theta_3 = 0.33ML$.

1.2.4). Specifically, if the density of 6T islands on silicon oxide is bigger than the density of second layer 6T islands on the first monolayer, this means that the $E_{i^*}(SiO_x - 6T) > E_{i^*}(6T - 6T)$. Since these energies are binding energies, they are negative and this result is telling us that 6T-6T interaction is stronger than SiO_x-6T's one, which is exactly what we are expecting (silicon oxide is an inert substrate).

From the AFM images it can be also appreciated that the biggest change in the island density regards the shift from image 1) to image 2), since here we are passing from SiO_x to 6T as substrates. On the other hand, the difference between image 2) and 3) is quite negligible since the substrate is always the same.

Once the other relevant energies, like the diffusional one, are known, these binding energies can be in principle calculated.

7.2.3 The Distributed Growth Model and the Ehrlich-Schwoebel barrier

To get more physical information about the growth kinetics under investigation, we fit the experimental data, i.e. the rms values, with a simple but powerful model, the Distributed Growth Model (DGM), introduced by Cohen and coworkers ([8]) and already used to study the growth dynamics of Ag ([9]), GaN ([10]) and pentacene ([11]). As described in subsection 1.3.6, the DGM makes the hypothesis that, of the $(\theta_n - \theta_{n+1})/\tau$ atoms per unit time arriving on the top of the nth layer, a fraction α_n transfer down to the nth layer and a fraction $1 - \alpha_n$ remains on top of the nth layer. More specifically, in the DGM the downwards transfer (and not the upwards, which is excluded), or interlayer diffusion, is taken into account assuming the probability of jump α_n related to the perimeters of the nth and $(n+1)th$ layer. In other words,

α_n measures the rate at which molecules transfer down from the $n + 1$th layer o the nth one.

The procedure we followed for the fit was the following:

- calculate the rms from the experimental layer occupancies

- calculate theoretical occupancies θ_n

- calculate rms from theoretical occupancies using the formula $\sigma^2 = \sum_{n=0}^{\infty}(n - \theta_{tot})^2(\theta_n - \theta_{n+1})$

- compare experimental and theoretical rms (fit)

- find the best fit, using as free parameters A_n and the perimeters

- once found the best fit, plot also the layer occupancies associated with that best fit

We are now ready to show the result of the simulation in Figure 7.9.

Several observations can be done: first, there is a good agreement between the experimental data, layer occupancies and rms, and the DGM best fit. This means that the assumptions behind this model are the correct ones to describe the physics driving this 2D+3D growth process. This was not obvious, other models, would not be able to catch the main points of this kinetics. Since the main idea behind the DGM, is the downwards transfer of molecules (in a distributed way, distributed with respect to the perimeters), the result shown in Figure 7.9, underlines the importance of this diffusive phenomena to describe the growth of 6T on silicon native oxide. Moreover, using only one simple model (dependent on just two kinds of parameters, A_n and d_n), we are able to describe two different growth mechanism, 2D and 3D.

Regarding the roughening transition happening at the third layer, one can notice that the oscillation behaviour of the rms actually holds true also for the third layer, where a smoother oscillation can be seen mainly at low temperatures. This does make sense, since we expect the transition from 2D to 3D growth to take place in a smooth way, gradually yielding a power law trend of the rms. Notably, the DGM is able to describe also this behaviour. This is due to the fact that, the probability best fit parameters, A_n, have been chosen independent between each other, thus giving the possibility to have different rms behaviours at each layer.
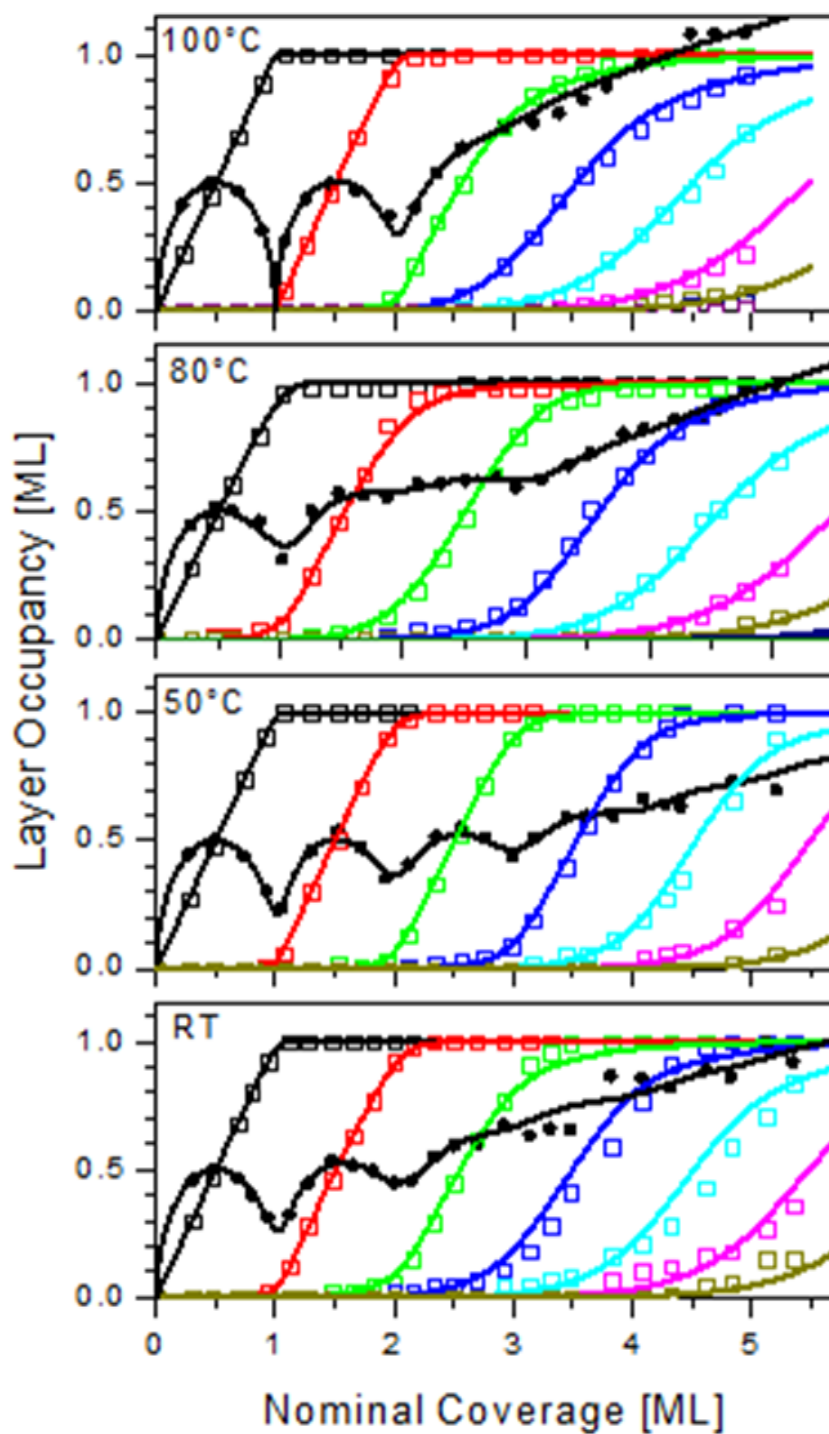
Figure 7.9: Experimental data and best DGM fir for RT, 50°C, 80°C and 100°C.

Actually, one aim of the DGM simulation was also to obtain the Ehrlich-Schwoebel barrier. Following ([11]), indeed, it is possible to make the following assumption re-
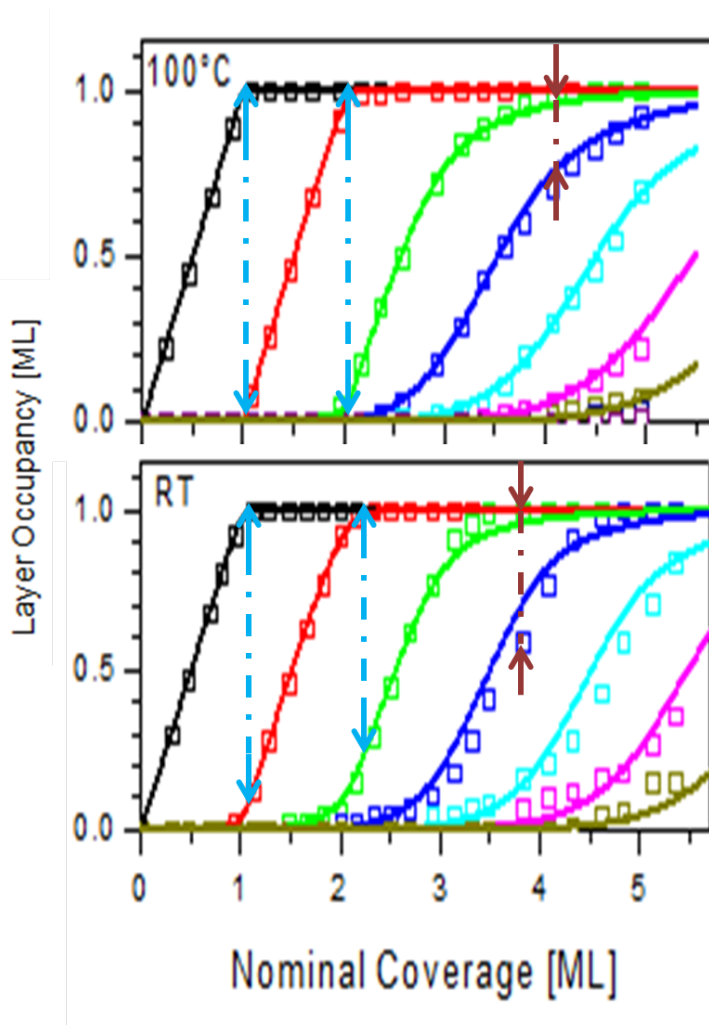
Figure 7.10: Figure 7.9 zoom of RT and 100°C case. The arrows show how to claim the 2D and 3D growth from the layer occupancies. Both the second and the third layer start only when the previous ones have been completed. This does not hold true for the fourth layer which starts before the third one has a layer occupancy of 1.

garding A_3, i.e. the probability of a molecule to jump off the fourth layer and join the third one:

$$A_3 \sim \exp\left(-E_{ES}/kT\right) \tag{7.4}$$

This relation describes the existence of an energy barrier at the top of the third layer which molecules can overcome due to thermal energy. Moreover, as expected, it states that this probability increases with temperature.

As already seen, we were not able to calculate this value since, increasing temperature, the system grows more into 3D, meaning that the probability to jump off

the top of the third layer (where the roughening transition takes place) is decreasing with time and not increasing.

In Figure 7.11, indeed, one can see the evolution with temperature of the calculated probability of jump (from the best fit of experimental rms)
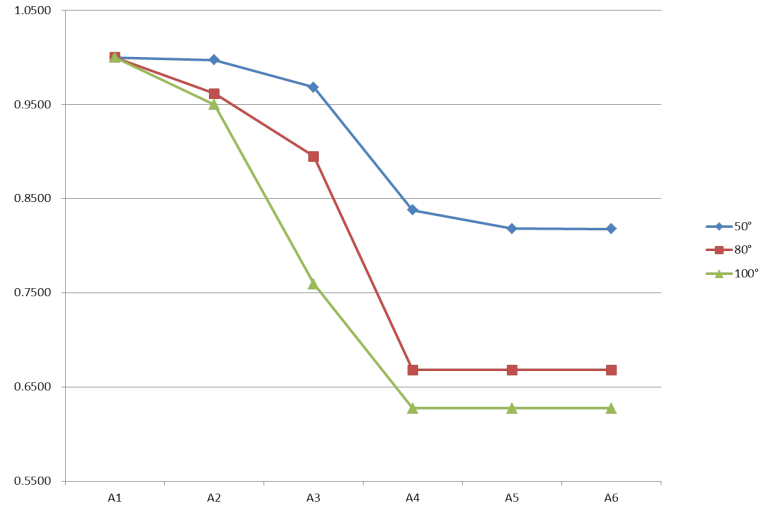

Figure 7.11: Evolution with time of jump off probability. As can be seen the trend is decreasing with temperature, a behaviour not in agreement with the classical interpretation of the Ehrlich-Schwoebel barrier.

As expected, A_1 is one for each temperature: the probability to jump off the second layer to join the first one is equal to one. This is needed to have a 2D growth, which is what we observe. Similar situation for A_2: the values are slightly different from one but still, one can see it as a sign of layer by layer growth.

From A_3 onwards, instead, the probabilities starts to decrease: this is the signature of a roughening transition taking place at the third layer, see discussion above. Moreover, one can also notice the probabilities for the fourth, fifth and sixth layer being constant at fixed temperatures; this means that it is the third layer the real transition layer between 2D and 3D growth.

7.2.4   2D+3D growth

As already noticed by the AFM images, the whole growth mechanism is 2D+3D with a roughening transition at the third layer. This can be properly quantified

by the layer occupancies for each substrate temperature. As can be seen in Figure 7.12, indeed, at each temperature, when the first layer occupancy is 1, the second layer is just starting to nucleate, and when the second layer is complete the third occupancy is almost negligible. This does not hold true, for the following layers: for instance, when the third occupancy is 1, the fourth layer has already started to nucleate, determining an increase in the roughness of the thin film. On the other hand, the same conclusion can be drawn looking at the root mean square (rms) roughness plot of the film. Indeed, for each temperature as well, the first two layers are characterized by an oscillating behaviour, while from the third layer on, a clear slope can be seen. This is in agreement with a 2D+3D growth: the oscillating behaviour in the rms is the typical signature of a layer by layer (or 2D) growth while, a power law trend of the rms ($\sigma \sim \theta^\beta$) involves a 3D growth ([6,12]). One can also notice that the two peaks of the oscillating behaviour are basically at half monolayer, with a value equal to 0.5 ML, as well: this is exactly what one would expect.

Moreover, looking better the rms (but the same conclusion can be obtained considering the layer occupancies), one can see this 2D and 3D growth to be more pronounced at higher substrate temperature. Indeed, the minimum of the rms are lower at 100°C with respect to RT, while, on the other hand, the slope of the rms for the fourth and fifth layer is bigger at 100°C, as well. The first observation is completely in agreement with the previous work of Straub ([7]), which performed the same kind of in-situ experiment up only to the third layer, see Figure 7.13.

Regarding the power law behaviour $\sigma \sim \theta^\beta$, valid only during 3D growth, from the experimental data, the *beta* values can be calculated by a power law fit. In Figure 7.14, the results can be seen for the four relevant substrate temperatures. The trend is not what we were expecting. If an Ehrlich-Schwoebel barrier is present, a higher temperature should increase the interlayer diffusion thus driving the growth process towards a layer by layer growth, i.e. decreasing β. A part for the RT point, which we will discuss later, the experimental observation is exactly the opposite: temperature is driving the growth towards a more 3D morphology.

This is not the first observation of such a behaviour, also Ernst ([13]) and Mayer ([11]) found a similar trend. Specifically, Ernst and coworkers analyze the homoepitaxial growth of Cu (100) finding a growth exponent β at 160K equal to 0.26 and at 200K equal to 0.56. As an explanation they report a previous suggestion of Kunkel *et al.* ([14]), whose idea is that the Ehrlich-Schwoebel barrier becomes less effective when islands become small (i.e. at low temperatures). In the work of Mayer, in-
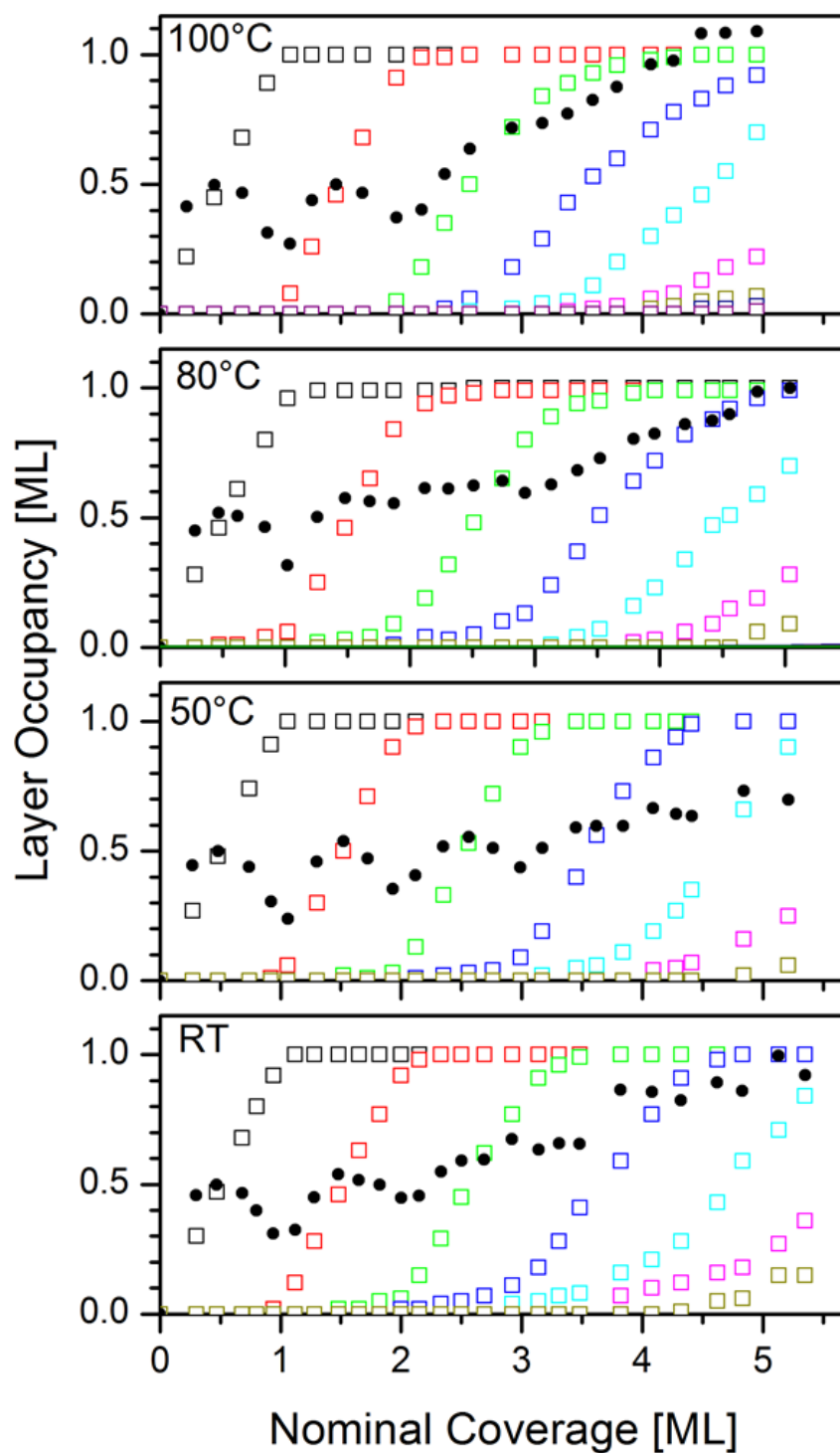
Figure 7.12: Experimental data for each temperature: layer occupancies (coloured squares) and rms (black points. From these behaviours a 2D+3D growth can be claimed.)
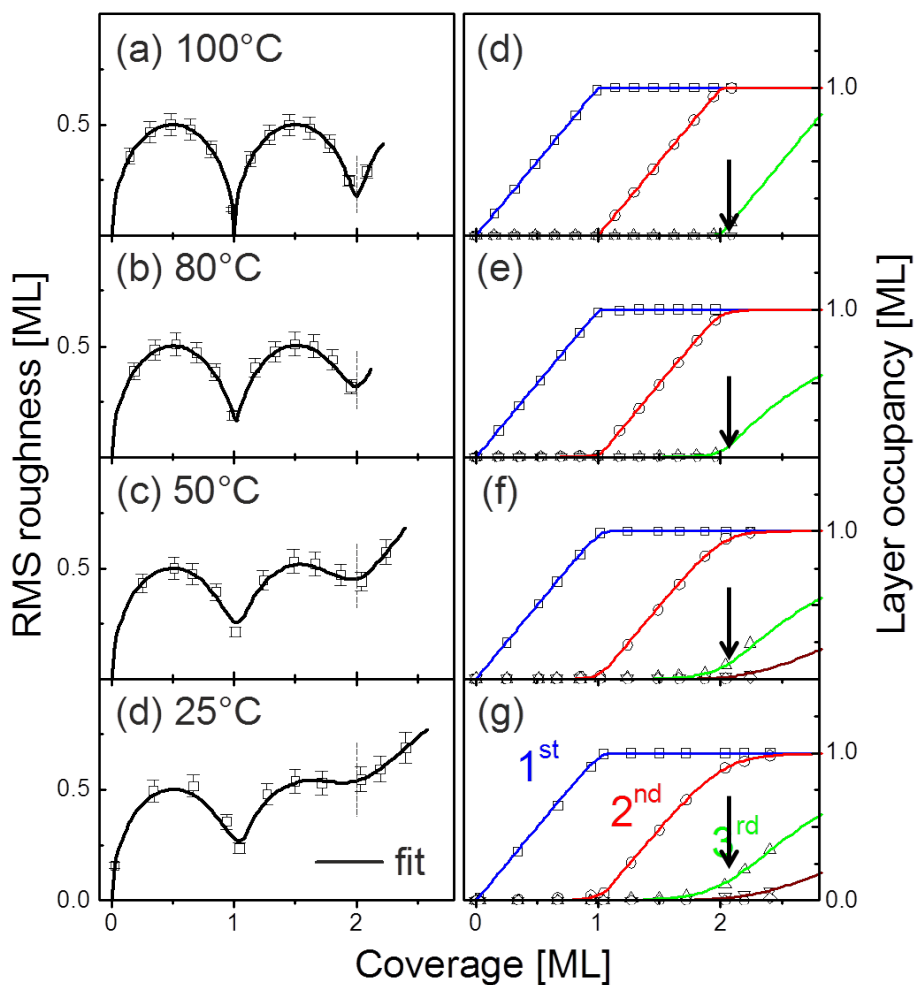
Figure 7.13: Roughness and layer occupancies evolution up to the third layer ([7]). The arrows clearly show the 2D growth mechanism to be sharper at 100°C, where one layer starts only when the previous has been completed. The fit line is the best fit result by DGM

stead, pentacene is deposited on HTS and, using a Distributed Growth Model (see subsection 1.3.6, the probability for downward diffusion at the third layer is calculated obtaining a decreasing behaviour with increasing temperature (i.e. more 3D growth). The explanation, in this case, regards the existence (confirmed by AFM images) of multimolecular steps which are not taken into account by the DGM model, dealing only with one layer steps.

Our idea, does agree both with Mayer's explanation and Ernst's one, more specifically, we think to be in front of a so called *reentrant* ([12,14]) layer by layer growth (applied, this time, to organic materials and not metals) characterized by multimolecular steps (see the AFM images of Figure 7.4). In fact, high temperatures
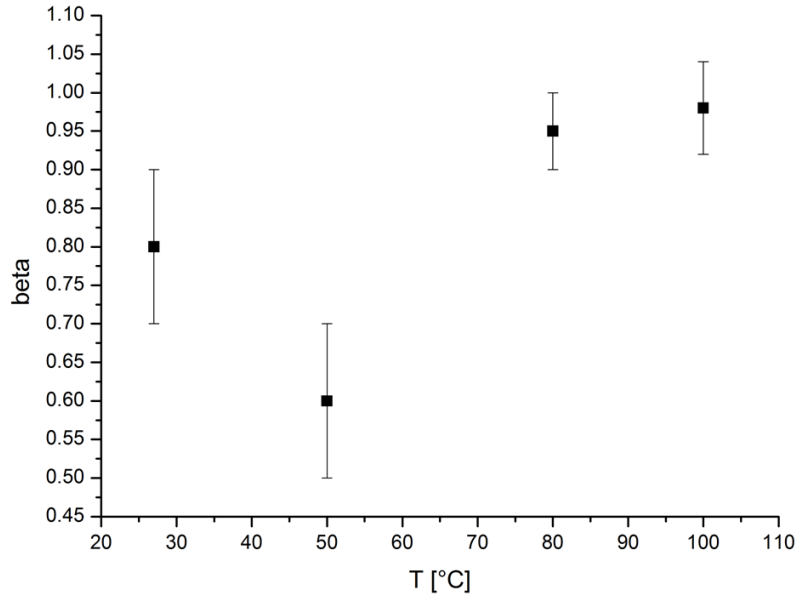
Figure 7.14: Growth exponent β values at the four different temperatures: RT, 50°C, 80°C and 100°C.

are not the only situation favouring 2D growth, due to a higher probability for the molecules to jump off and overcome the Ehrlich-Schwoebel barrier. It has been observed also at low temperature ([14]), with, as already explained, the reduced islands size and their irregular shape as a possible explanation for the behaviour. A more clear description of why the Ehrlich-Schwoebel energy barrier should be less important at low temperatures comes from Evans and coworkers ([15]), who recently proposed *downward funneling* ([16]) as a possible smoothing effect at low temperatures.

Moreover, following ([17]), since our relevant *beta* values are bigger than 0.5 (the random deposition limit ([18])), we are in front of a *rapid roughening* behaviour, which has already been observer for a number of systems ([17,19,20]). Since roughness beyond the random deposition limit, i.e. 0.5, can occur only if matter is transported to higher layers ([17]), this is in contradiction with the assumption of the Distributed Growth Model. In this model, indeed, only downward interlayer diffusion is taken into account. How to match these two different points of view, is still under investigation. Surely, the DGM is able to capture the main behaviours of the growth of 6T on silicon oxide but, at the same time, it is not able to give a complete description of the physics. Probably it is oversimplified and generalizations need to be applied.

Regarding the RT point, we claim it to be not relevant. Probably, the small AFM scan zone, $6\mu m$ x 6 mum (small if compared with typical x-ray experiments),

can give an explanation for such a 3D growth which must be seen as an exception due to local fluctuation of the morphology. In the next future we will repeat the whole RT experiment to check such behaviour.

7.2.5 Morphology and fractal dimension

As already observed in Figure 7.1, 7.2, 7.3 and 7.4, there is a shape transition for the 6T islands, both at a fixed temperature, with coverage, and at different temperature at a fixed coverage.

To quantify this effect, following ([8]), we calculate by Fractalyse (see subsection 2.6.2) the fractal dimension of the islands to estimate how much dendritic or compact they are. The result is shown in Figure 7.15.

As can be seen, at each fixed temperature, for the first two layers (from the third on, due to 3D growth, it is quite complicated to obtain the fractal dimension)), an oscillating behaviour is present. This underlines that islands with a fractal (dendritic) shape are more present in the initial stage of the formation of a layer, while, towards the end, the shape become more compact (roundish). In the next future, we aim to correlate this fractal dimension estimation of the islands' shape, with the *beta* behaviour found in Section 7.2.4. Indeed, as already pointed out, we think the *beta* correlation with temperature of the substrate can be explained as a reentrant layer by layer growth applied to organic material. This correlation, following ([14]), can be ascribed to a less effective Ehrlich-Schwoebel barrier at low temperatures, when the island density is higher and the shape is more fractal-like.

7.3 120°C experiment

We report here also some AFM images (Figure 7.16 and 7.17) showing the morphological evolution of the thin film at a substrate temperature 120°C.

While almost all the first monolayer evolves with time in a 2D growth, from there on a different kind of morphology can be appreciate. The roughness of the film increases but not following a standard 3D growth mechanism. Indeed, precise geometrical angles at the edges of some "islands" can be observed, moreover, quite often, one can notice that nucleation on upper layers starts from the edges, as if molecules are moving upwards. These two phenomena are typically associate to dewetting, and, indeed, we think that for 6T on SiO_x at 120°C, this is the case.
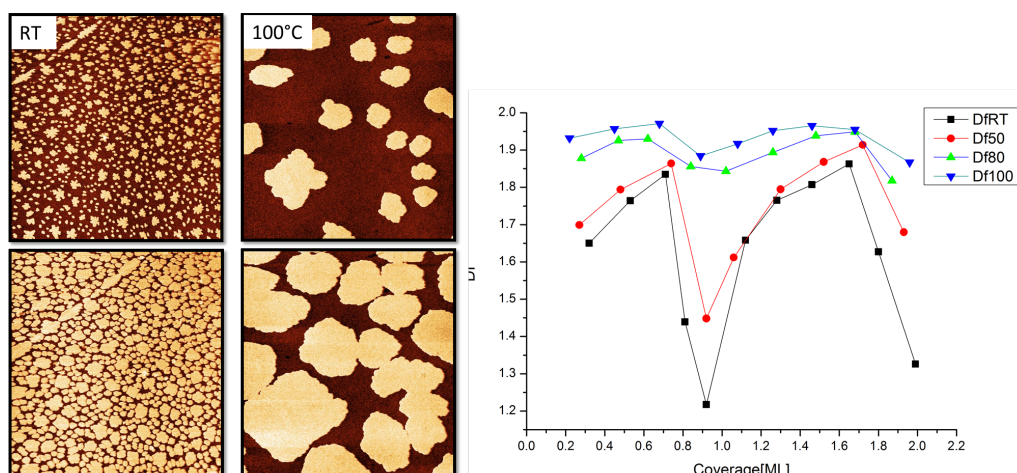
Figure 7.15: (left) Morphology of 0.30ML and 0.94ML at RT. (right) Morphology of 0.22ML and 0.89 ML at 100°C. Plot of the fractal dimension *vs.* coverage at different substrate temperature. An oscillating behaviour is clearly visible. Fractal islands are more present at low temperatures and in the beginning of the monolayer formation.

Since it is a different kind of growth we did not take this experiment into account in our data analysis, even because, practically, it would have been quite difficult to estimate with precision all the single layer occupancies.
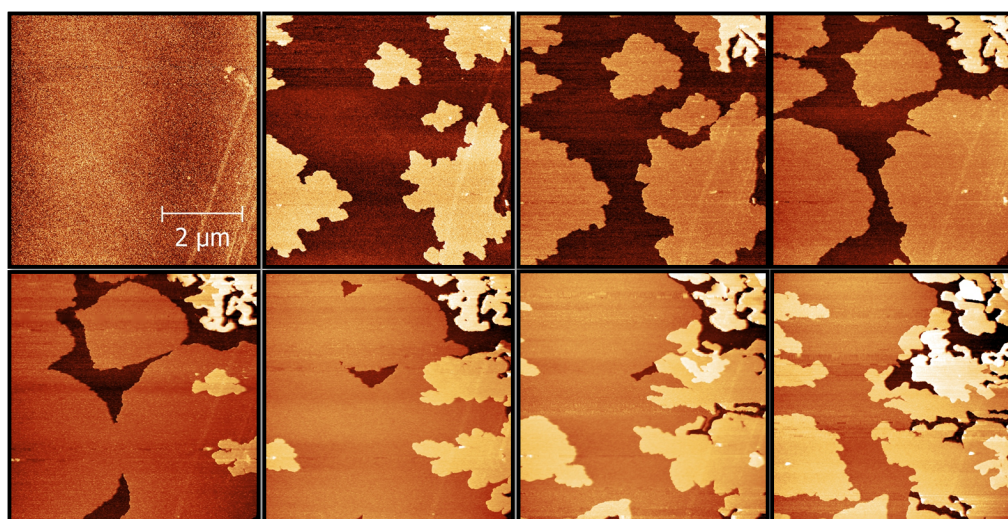

Figure 7.16: Morphological evolution of almost the first two monolayers, at 120°C. As can be seen, the morphology of the second layer is irregular due to a starting dewetting phenomena in the top right position of the AFM scan.
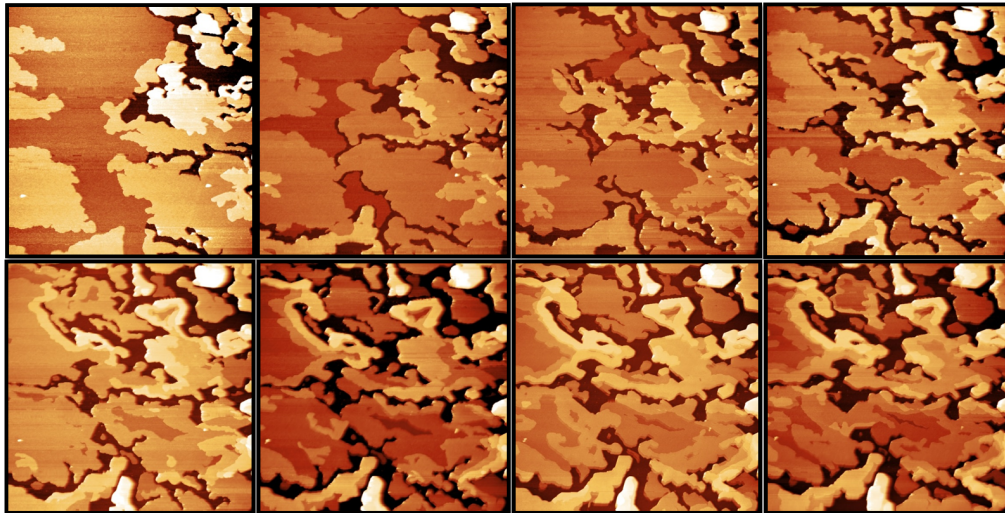
Figure 7.17: Morphological evolution of the thin 6T film, at 120°C, from the second layer onwards. Two basic phenomena are observable: the formation of edges at a specific geometrical angle and the upwards current of molecules from the edges. These are dewetting phenomena peculiarities.

7.4 Bibliography

[1] S. D. Quiroga. *In-situ real time investigation of organic ultra thin film transitors: growth, electrical properties and biosensing applications.* Ph.D. thesis, CNR-ISMN Bologna (2010)

[2] B. Voigtlaender, A. Zinner and T. Weber. *Rev. Sci. Instrum.*, **67**, 2568 (1996)

[3] F. J. Meyer zu Heringdorf, M. C. Reuter and R. M. Tromp. *Nature*, **412**, 517 (2001)

[4] J.-F. Moulin, F. Dinelli, M. Massi, C. Albonetti, R. Kshirsagar and F. Biscarini. *Nuclear Instruments and Methods in Physics Research Section B: Beam Interactions with Materials and Atoms*, **246**, 122 (2006)

[5] X. Zhang, E. Barrena, D. de Oteyza and H. Dosch. *Surface Science*, **601**, 2420 (2007)

[6] A.-L. Barabasi and H. E. Stanley. *Fractal Concepts In Surface Growth.* Cambridge University Press (1995)

[7] A. Straub. *Advanced SPM studies on the growth of ultrathin films of organic semiconductors at metal and dielectric interfaces.* Ph.D. thesis, Alma Mater Studiorum-Universita' di Bologna (2011)

[8] P. I. Cohen, G. S. Petrich, P. R. Pukite, G. J. Whaley and A. S. Arrott. *Surface Science*, **216**, 222 (1989)

[9] H. A. van der Vegt, H. M. van Pinxteren, M. Lohmeier, E. Vlieg and J. M. C. Thornton. *Phys. Rev. Lett.*, **68**, 3335 (1992)

[10] A. R. Woll, R. L. Headrick, S. Kycia and J. D. Brock. *Phys. Rev. Lett.*, **83**, 4349 (1999)

[11] A. C. Mayer, R. Ruiz, H. Zhou, R. L. Headrick, A. Kazimirov and G. G. Malliaras. *Physical Review B*, **73**, 1 (2006)

[12] C. Bartelt. *Physical Review Letters*, **75**, 4250 (1995)

[13] H.-J. Ernst, F. Fabre, R. Folkerts and J. Lapujoulade. *Phys. Rev. Lett.*, **72**, 112 (1994)

[14] R. Kunkel, B. Poelsema, L. K. Verheij and G. Comsa. *Phys. Rev. Lett.*, **65**, 733 (1990)

[15] J. Evans, P. Thiel and M. Bartelt. *Surface Science Reports*, **61**, 1 (2006)

[16] J. W. Evans, D. E. Sanders, P. A. Thiel and A. E. DePristo. *Phys. Rev. B*, **41**, 5410 (1990)

[17] a. Dürr, F. Schreiber, K. Ritley, V. Kruppa, J. Krug, H. Dosch and B. Struth. *Physical Review Letters*, **90**, 016104 (2003)

[18] J. Krug. *Advances in Physics* (1997)

[19] G. W. Collins, S. A. Letts, E. M. Fearon, R. L. McEachern and T. P. Bernat. *Phys. Rev. Lett.*, **73**, 708 (1994)

[20] T.-M. Fang, K. Lu and G.-C. Wang. *Phys. Rev. B*, **49**, 8331 (1994)

Chapter 8

Electrostatic Force Microscopy theoretical model

Electrostatic Force Microscopy (EFM) is a powerful tool to investigate the electric properties of materials at the nanoscale ([1]). An AFM cantilever-tip system is biased with respect to the substrate to detect and image the local electrostatic properties of the substrate surface. Depending on the method of measurement, electrostatic force techniques are known by a variety of names, including the generic electrostatic force microscopy, scanning capacitance microscopy ([2]), Kelvin probe microscopy ([3]) and possibly others.

EFM and its various implementations have been used to analyze different properties of solid surfaces ([4]), the dielectric response of single molecules ([5]), the behaviour of liquid samples ([6]), the formation of water nanobridges ([7]), till the recent Nanoscale Capacitance Microscopy (NCM) which allows to quantify intrinsic properties of thin dielectric films, including film thickness and dielectric constant ([8]).

Despite all the work done on EFM, still the picture is not complete. As demonstrated by several works ([9]), the EFM images are strongly dependent on the geometrical shape of the AFM tip: the truncated cone plus hemisphere geometry is, up to our knowledge, the most studied configuration, due also to the agreement with experimental data ([10],[11],[8]). However, a lack of this treatment is that it is not analytical but numerical.

Looking for analytical formulations of the physics behind a typical EFM experiments, we (re)propose an hyperboloidal geometry ([12]) for the tip and develop an original mathematical model to obtain, in a more complete way, the capacitance of the tip-metallic substrate system. We are working on an extension of the model to the case of a thin film on the substrate and we think it could help also to have a deeper understanding of the important concept of limit of resolution of an EFM

microscope.

8.1 EFM technique

When a voltage V occurs between a tip and a sample, the electrostatic force F can be written as ([13]):

$$F = |\vec{F}| = \frac{1}{2}V^2\frac{\partial C(z)}{\partial z}$$ (8.1)

where z is the tip sample distance.

Typically, EFM operations are made under room conditions in tapping mode on the basis of a **double pass method** ([14]). During the first pass (scan), the surface topography is acquired, then the tip is retracted from the surface by a constant height H_{lift}, also called lift height. The tip is moved following the topographic profile previously acquired in order to keep H_{lift} constant (second pass) and the potential V is applied to the tip (while the sample is grounded). The lift height is chosen higher than 10 nm to avoid van der Waals interactions that introduce topographical artifacts. In the second pass, the free amplitude of the tip vibration is reduced of δz due to the electrostatic force gradient. Such variation are small enough to stay in the linear regime of the amplitude tip-sample distance.

From 8.1, we can say the force gradient to be related to the cantilever-tip-sample capacitance $C(z)$ by:

$$F^{'}(z) = |\frac{\partial F}{\partial z}| = \frac{1}{2}V^2\frac{\partial^2 C(z)}{\partial z^2}$$ (8.2)

As shown in Figure 8.2, during the first scan the average tip-sample distance is approximately equal to the amplitude ($z_1 \sim \delta z_1$). During the second scan, the distance is the sum of the first scan amplitude δz_1 and the lift height H_{lift} ($z_2 \sim \delta z_1 + H_{lift}$). δz_2 is the second scan amplitude.

There are two possibilities to detect the local electrostatic force gradient. The first one is to measure directly the resonance frequency shift Δf_0 keeping the phase shift constant. The second possibility is to measure the mechanical phase shift $\Delta\Phi$ at constant driving frequency. If we consider that the cantilever-tip-sample system can be approximated by a spring mass system, the relationships between frequency $\Delta\omega$ or phase shifts $\Delta\Phi$ and force gradient, can be written as (see subsection 2.4.2)

$$\frac{\Delta\omega}{\omega_0} \sim -\frac{1}{2k_0}F^{'}(z)$$ (8.3)

$$\Delta\Phi \sim -\frac{Q}{k_0}F^{'}(z)$$ (8.4)
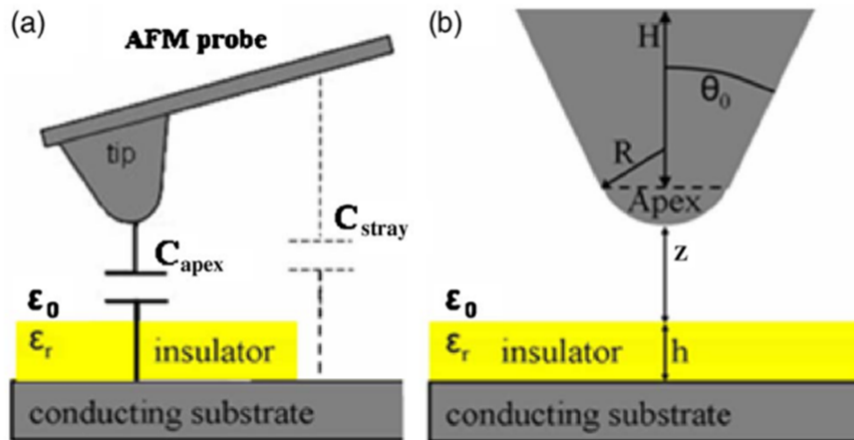
Figure 8.1: (a) The physical system under investigation, with the two main capacitances involved. (b) A magnification of the tip, showing the main geometrical factors.
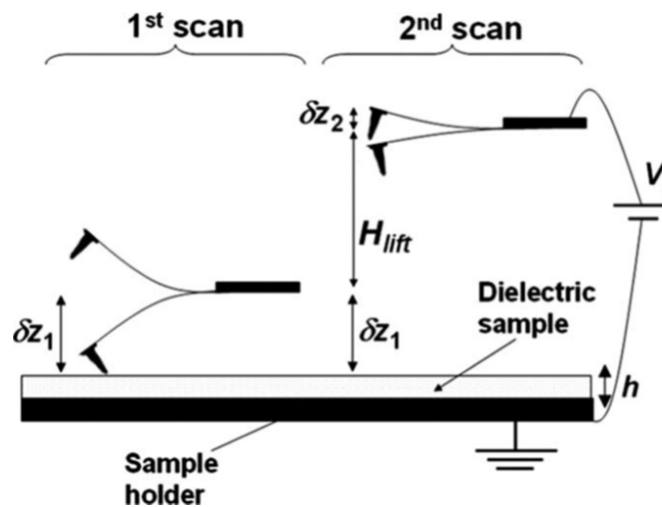
Figure 8.2: Principle of EFM microscopy using a double pass method. During the first scan topography is acquired. The tip is then retracted and during the second scan, a potential V is applied on the tip and the force gradient is detected.

As can be seen by all the previous expressions there is a strict correlation between the detected force gradient and the (derivatives) of the capacitance of the system. This is the reason for the strong tip-cantilever-sample capacitance modeling effort which has been done in the past.

8.2   Tip-sample capacitor: the hyperboloidal model

Several geometrical models have been used in the past to describe the EFM tip-sample geometry ([9]): among all, the **truncated cone plus an hemisphere** in front of an infinite plane (the sample) is the most studied one. Belaidi ([9]) used a **numerical method** to evaluate the force-distance relation in this geometry. Hudlet, ([15]) proposed an **analytical approximation** for the same force-distance relation which is found to be in agreement with Belaidi up to 10%. More recently, several EFM works ([10],[11],[8]), aiming to calculate the dielectric constant of thin dielectric films, strongly referred to these numerical-(approximate) analytical results. Calculations have been done also for the cantilever-sample system, both in the case of a metallic sample or a thin dielectric film ([10],[16]) but here we will focus only on the tip-metallic sample capacitance.

Looking for exact analytical calculations of this tip-substrate physical system, we refer to another geometry, already introduced in the past ([12]), which fits better the system.

In this view, the tip corresponds to an **hyperboloidal surface**, truncated somewhere up due to its finite dimension. Cartesian coordinates (x,y,z) are not directly able to describe such a shape, so it is better to shift to an orthogonal as well set of coordinates, the **prolate spheroidal coordinates (ξ, η, Φ)**, where hyperboloids are easily parameterized setting one of the coordinates (η) equal to a constant. Moreover, even the other important equipotential surface, the sample, is identified by the same coordinate η equal to zero.

Two definition of the prolate spheroidal coordinates are proposed in literature, the one we choose is the following:

$$x = a\sqrt{(\xi^2 - 1)(1 - \eta^2)}cos\Phi \tag{8.5}$$

$$y = a\sqrt{(\xi^2 - 1)(1 - \eta^2)}sin\Phi \tag{8.6}$$

$$z = a\xi\eta \tag{8.7}$$

with $1 \leq \xi < \infty, 0 \leq \eta < 1, 0 \leq \Phi < 2\pi$ and a being the focus of the hyperboloidal η=constant surfaces. These definitions are followed also by ([17],[18]).

As can be seen by the figure, one of the advantages of this orthogonal set of coordinates is that the tip is described by η=constant value, with small values of η corresponding to dull tips while high values to sharp tips. In Cartesian coordinate we would have been forced to deal with a more complicated quadratic expression.
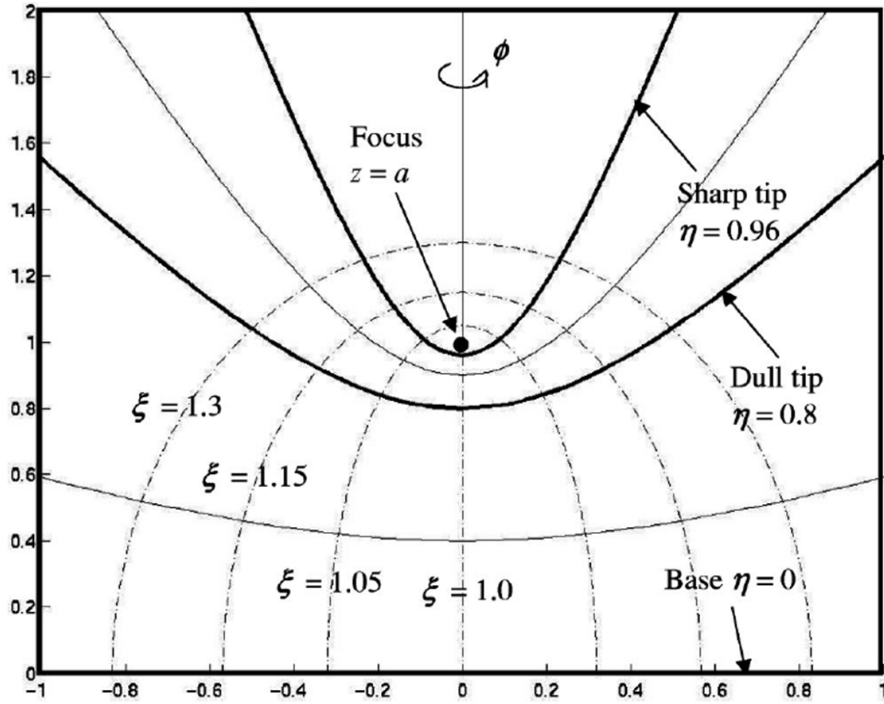
Figure 8.3: Tip-substrate system represented in prolate spheroidal coordinate.

We also here report the so called scale factors, useful in case of a change of coordinates, from (x,y,z) to (ξ, η, Φ), inside an integral:

$$h_\xi = |\frac{\partial \vec{r}}{\partial \xi}| = a\sqrt{\frac{\xi^2 - \eta^2}{\xi^2 - 1}} \tag{8.8}$$

$$h_\eta = |\frac{\partial \vec{r}}{\partial \eta}| = a\sqrt{\frac{\xi^2 - \eta^2}{1 - \eta^2}} \tag{8.9}$$

$$h_\Phi = |\frac{\partial \vec{r}}{\partial \Phi}| = a\sqrt{(\xi^2 - 1)(1 - \eta^2)} \tag{8.10}$$

More specifically:

$$\int d\vec{x} = \int dx\, dy\, dz = \int h_\xi h_\eta h_\Phi d\xi\, d\eta\, d\Phi \tag{8.11}$$

Following ([12],[19] and [20]) we aim to obtain an exact (not approximate like for Hudlet) analytical formula for the capacitance C between the tip and the substrate system.

To calculate $C_0 = Q/V$ of the system, where V is the selected potential difference between the tip and the sample (connected to ground), we need to calculate
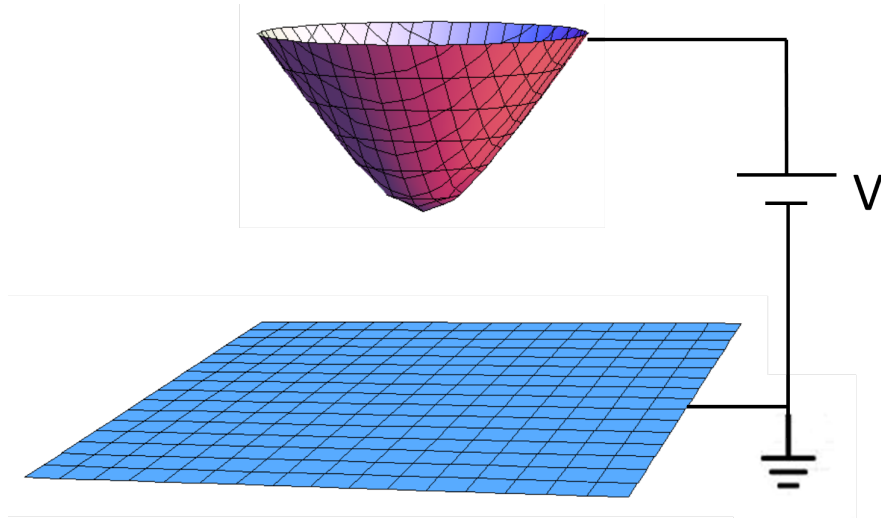
Figure 8.4: A picture of the capacitor under investigation. In between the two plates we suppose to have vacuum.

the charge Q accumulated on the tip. This is obtained by a surface integral of the surface charge density which, instead, by the Coulomb theorem known from electrostatics ([13]), is depending on the electric field evaluated on the surface of the tip. The electric field is (-) the gradient of the electric potential so, in the end, what we need is to solve the well known **Laplace equation** for the electric potential itself, with known boundary conditions (Dirichlet problem). Between the tip and the sample we suppose to have vacuum (later we will face the problem with a dielectric in between), then the starting point is:

$$\nabla^2 V = 0 \tag{8.12}$$
$$V(tip) = V$$
$$V(sample) = 0$$

Some remarks should be done concerning the first boundary condition. If we refer to $\eta = \eta_0$ we are considering the whole infinite hyperboloidal surface which of course is not the proper geometrical configuration of the real truncated tip (while, instead, the sample can be considered as an infinite plane). More specifically then, the proper Dirichlet problem for the Laplace equation should be referred to a tip truncated somewhere up with a disk:

$$\nabla^2 V = 0 \tag{8.13}$$
$$V(tip + disk) = V$$
$$V(sample) = 0$$

Unfortunately, solving this Laplace equation is not easy. Indeed, the first boundary condition should be written in the following way $V(A \cup B) = V$ with:

$$A = \{(\xi, \eta, \Phi)| \ \eta = \eta_0, \ 1 \leq \xi \leq \xi_{max}, 0 \leq \Phi < 2\pi\} \tag{8.14}$$
$$B = \{(x, y, z)|x^2 + y^2 = r_{max}^2, \ r_{max} = a\sqrt{(\xi_{max}^2 - 1)(1 - \eta^2)}, \ z = a\xi_{max}\eta_0\}$$

This mathematical problem is very hard to solve in a closed form, so we have to shift to the previous -more easy to solve- Dirichlet problem dealing with an infinite tip. **Once we will have the solution we will try to impose the finiteness of the tip with a cut off (in the charge integration)**.

Before this, another remark should be done: is the cut-off procedure after solving the Laplace equation equivalent to solve the Laplace equation with the cut-off already inside the boundary conditions like in 8.14? The answer is no. This can be understood taking into account the so called **edge effects** (or fringe effects). If we let the tip be infinite, of course, the edge effects will not be part of the calculations and when we will cut the tip, with a cut-off in the charge integration, they will not be considered as well. Imposing the finiteness of the tip directly in the boundary conditions of the Laplace equation, instead, is a way to describe also the edge effects but, as already mentioned, this is a quite difficult mathematical problem. For the sake of simplicity, we will rule out the edge effect problem, trying to directly solve 8.12.

Coming back to the Laplace equation, in Cartesian coordinates this famous equation is very well known, but in our case we need to solve it in prolate spheroidal coordinates. In these coordinates the Laplace operator reads (we directly get rid of Φ contributions due to rotational symmetry of the tip):

$$L_{(\xi, \eta)} = \frac{1}{a^2(\xi^2 - \eta^2)}\left[\frac{\partial}{\partial\xi}[(\xi^2 - 1)\frac{\partial}{\partial\xi}] + \frac{\partial}{\partial\eta}[(1 - \eta^2)\frac{\partial}{\partial\eta}]\right] \tag{8.15}$$

If the Φ contribution can be excluded, less obvious, instead, is whether we can also exclude the ξ coordinate part. If the tip was infinite, this coordinate would be useless as a small calculation referred to the boundary condition can prove (even if not in the most general way). Let's suppose V depending only on η and ξ (Φ has been excluded before). If we separate the two contributions in the standard way: $V(\eta, \xi) = v(\eta)u(\xi)$ then, referring to the first boundary condition we have $V(\eta_0, \xi) = v(\eta_0)u(\xi) = V$. Being $v(\eta_0)$ a number we can conclude that $u(\xi) = V/v(\eta_0)$ can not be a function of ξ. In other words, if the tip is supposed infinite, and we use the separation of variables method, than the potential is a function only of the η coordinate. This quick demonstration is not the most general one can image, because it refers only to electric potential functions that can be written with

the separation of variables which is not the whole class of solutions of the Laplace equation. However, this is a quick way to show, at least theoretically, that when the real truncated geometry of the tip is considered, even the η coordinate should be taken into account in order to have the complete solution.

Coming to the solution of the Laplace equation, if by electrostatics we have understood this equation to be the starting point, from now on, the problem will be just mathematical.

If we look at 8.15, the operator has two separated contribution in ξ and η and so, one could be tempted to solve this partial differential equation (PDE) by separation of variables (a standard way to solve PDE, also used, for instance, to solve Schroedinger's equation in Cartesian coordinates for hydrogen-like atoms ([21])). However, the simple check of the first boundary conditions above, excludes this possibility since the ξ contribution, $u(\xi)$, would be constant, in reality. This check, actually contradicts also some works present in literature where, with the same boundary conditions, authors try to solve the Laplace equation in prolate spheroidal coordinates by separation of variables ([22]).

Since we can not solve by separation of variables then we have two possibilities left:

1. we look for another method to solve Laplace equation with those specific boundary conditions

2. we simplify the Laplace operator ruling out one of the two ξ or η contributions

In the following section we will focus on the second possibility, while, in Section 8.4 we will take in consideration point number 1.

8.3 η contribution

8.3.1   The electric potential

Since the two most important surfaces in the physical system under investigation are described by $\eta = constant$ value, one can expect η to be the most relevant parameter in the Laplace operator. If we accept this assumption, we strongly simplify the mathematical problem and with few calculations we can reach a result for the capacitance of the system. Indeed, if we rule out the ξ part of the Laplace operator 8.15, keeping only the η contribution, then the Laplace equation becomes:

$$\frac{d}{d\eta}[(1 - \eta^2)\frac{d}{d\eta}]V(\eta) = 0 \tag{8.16}$$

with $V(\eta_0) = V$ and V(0)=0 as boundary conditions (the tip is still infinite, so far). This second order differential equation can be solved in different ways: if, for instance, we call $f(\eta) = V'(\eta)$ we shift to a first order differential equation which, by indefinite integration, gives:

$$\frac{df}{d\eta}(\eta) = \frac{2\eta}{1-\eta^2} f(\eta) \tag{8.17}$$

$$f(\eta) = A\frac{1}{1-\eta^2} \tag{8.18}$$

where A is an integration constant. Since $f(\eta) = V'(\eta)$, now with another integration one can directly obtain:

$$V(\eta) = \frac{A}{2} ln(\frac{1+\eta}{1-\eta}) + B \tag{8.19}$$

where B is a second integration constant. Taking into account the boundary conditions, we can now finally get the solution:

$$V(\eta) = \frac{V}{ln(\frac{1+\eta_0}{1-\eta_0})} ln(\frac{1+\eta}{1-\eta}) = \alpha \ ln(\frac{1+\eta}{1-\eta}) \tag{8.20}$$

where we have defined $\alpha = V/ln((1 + \eta_0)/(1 - \eta_0))$. This solution is in agreement with $(^{17\,12}, ^{23})$.

8.3.2   The capacitance

From the electric potential one can calculate the electric field between the tip and the plane substrate. Being $\vec{E} = -\nabla \vec{V}(\eta)$ we have to use the expression of the gradient in prolate spheroidal coordinate, which is:

$$\vec{\nabla} = \frac{\hat{\xi}}{h_\xi}\frac{\partial V}{\partial \xi} + \frac{\hat{\eta}}{h_\eta}\frac{\partial V}{\partial \eta} \tag{8.21}$$

where h_ξ and h_η are the scale factors. The potential is a function only if η so the gradient operator can be simplified and the electric field calculated as:

$$\vec{E} = -\hat{\eta}\frac{\alpha}{a}\frac{2}{\sqrt{(\xi^2 - \eta^2)(1 - \eta^2)}} \tag{8.22}$$

in agreement with $(^{17})$.

Following Coulomb theorem known from electrostatics $(^{13})$, we are now able to obtain the surface charge density σ on the tip. Indeed, being the versor $-\hat{\eta}$ the unit vector normal to the tip:

$$\sigma = \epsilon_0\vec{E}(\eta_0) \cdot (-\hat{\eta}) = \frac{2\alpha\epsilon_0}{a}\frac{1}{\sqrt{(\xi^2 - \eta_0^2)(1 - \eta_0^2)}} > 0 \tag{8.23}$$

One can check that the highest surface charge density corresponds to $\xi=1$ which is the point of the tip with the biggest curvature. This is in agreement with electrostatics ([13]).

Now we are ready to calculate the charge Q on the surface of the tip. Without taking into account the finite dimension of the tip the general ξ integration will be over the whole ξ range, from 1 to ∞:

$$Q = \int_{S_{tip}} \sigma \ dS = \int_0^{2\pi} \int_1^{\infty} \sigma h_\xi h_\Phi \ d\xi \ d\Phi \tag{8.24}$$

this integration, obviously, gives an infinite result since if we have an infinite surface of integration the charge on it will be infinite as well. The only way the get back the real finite shape of the tip, is to introduce a cut off in the ξ integration. Calling the cut off ξ_{max} the result is $Q = 4\pi\alpha\epsilon_0 a(\xi_{max} - 1)$.

Now, finally, we can obtain the capacitance as:

$$C_0 = \frac{Q}{V} = \frac{4\pi\epsilon_0 a(\xi_{max} - 1)}{ln(\frac{1+\eta_0}{1-\eta_0})} \tag{8.25}$$

which can be written also as:

$$C_0 = \frac{2\pi\epsilon_0 a(1 - \eta_0^2)}{V}(\xi_{max} - 1)V'(\eta_0) \tag{8.26}$$

Typical values of a, ξ_{MAX} and η_0 are: 40nm, few units and 0.8, respectively. With these it can be calculated that the order of magnitude of C_0 is $10^{-18}aF(attoFarad)$ which is in total agreement with previous calculations referred to different geometries ([8],[11]).

In order to test this capacitance formula one could look for a parallel plate capacitor limit. We notice that if we flatten the tip, letting $\eta_0 \to 0$, we should approximate two flat surfaces one in front of the other, the flatten tip and the sample. However, the tip is finite so we are not really approximating a parallel plate capacitor: the limit capacitor will be the one made of a finite disk and a plane, a geometry necessarily affected by edge effects. This is why we do not expect to have a strict coincidence between the capacitance of the system with $\eta_0 \to 0$ and the very well known formula $C_0 = \epsilon_0 \ S/d$ (with $S =$surface of the tip and $d =$ tip-sample distance) which is connected with two surfaces of the same (big) area.

Indeed, making use of first order Taylor expansions we obtain:

$$\lim_{\eta \to 0} C_0 = \frac{2\pi\epsilon_0 a(\xi_{max} - 1)}{\eta_0} \tag{8.27}$$

If, instead, we calculate the surface of the tip with respect to a general value of η_0, we flatten the tip $\eta_0 \to 0$ and we check the result for $C_0 = \epsilon_0 S/h$ we have:

$$\lim_{\eta \to 0}(\epsilon_0 \frac{S_{tip}}{d}) = \frac{\pi\epsilon_0 a(\xi_{max}^2 - 1)}{\eta_0} \tag{8.28}$$

The two formulas are quite similar but not equal. This is due to the edge effects: in the last capacitance no fringe effects are present because we are referring to a real parallel plate (disk) capacitor, while in the first formula there must be some side contribution of the electric field line because we are dealing with a finite disk in front of an infinite plate.

Evaluations of these edge effects are under investigation.

8.3.3 The phase and frequency shift

As described in Section 8.1, the main experimental parameters, $\Delta\omega$ and $\Delta\Phi$ are correlated with the gradient of the force, which is, then, the physical value to be calculated.

Making use of Equation 8.2, one has to calculate the second derivatives of the previously investigated capacitance C_0. This can be done, and taking into account that $\eta_0 = \sqrt{z/(z+r)}$ and $r_{max} = \sqrt{zr(\xi_{max}^2 - 1)}$ the result is (we report only $\Delta\Phi$ since $\Delta\omega$ will be straightforward):

$$\Delta\Phi \sim \frac{Q}{k_0}(\pi\epsilon_0 V^2)[\frac{-2r\ln(\xi_{max})}{z^2} + (1 - \frac{1}{\xi_{max}^4})(\frac{r}{2(z+r)^2})] \qquad (8.29)$$

8.4 ξ contribution

We now come back to a second possibility to solve Laplace equation, i.e. trying to solve it also taking into account the ξ contribution but without making use of the separation of variables method (see Section 8.2). We can already expect a change in the final capacitance value since new electric field lines are going to be taken into account with the ξ contribution. The problem is to quantify this change.

8.4.1 The electric potential: Sturm-Liouville method

The mathematical problem we have to solve is again:

$$\nabla^2 V(\xi, \eta) = 0 \qquad (8.30)$$

$$V(\xi, \eta_0) = V \qquad (8.31)$$

$$V(\xi, 0) = 0 \qquad (8.32)$$

where the Laplace operator, $\nabla^2 = L$, in prolate spheroidal coordinates, reads:

$$L_{(\xi,\eta)} = \frac{1}{a^2(\xi^2 - \eta^2)}[\frac{\partial}{\partial\xi}[(\xi^2 - 1)\frac{\partial}{\partial\xi}] + \frac{\partial}{\partial\eta}[(1 - \eta^2)\frac{\partial}{\partial\eta}] = \frac{1}{a^2(\xi^2 - \eta^2)}[L_\xi + L_\eta] \quad (8.33)$$

The final Φ-term inside the laplacian has been ruled out for symmetry reason.

The key observation is that, if the first boundary condition was equal to zero, we could see the laplace equation in prolate spheroidal coordinates as a Sturm-Liouville equation ([24]). We can recover this request on the boundary conditions by making the hypothesis that $V(\xi, \eta) = \Psi(\eta) + u(\xi, \eta)$, where, so far, $\Psi(\eta)$ is a generic function of η with $\Psi(\eta_0) = V$ and $\Psi(0) = 0$ to fulfill the request. Now, the problem can be written in the following way:

$$[L_\xi + L_\eta][\Psi(\eta) + u(\xi, \eta)] = 0 \qquad (8.34)$$

If we choose, without losing generality, $\Psi(\eta)$ in such a way that $L_\eta[\Psi(\eta)] = 0$, then $\Psi(\eta)$ has been already obtain in 8.20, i.e. $\Psi(\eta) = V(\eta)$, and

$$L[u(\xi, \eta)] = 0 \qquad (8.35)$$
$$u(\xi, \eta_0) = 0 \qquad (8.36)$$
$$u(\xi, 0) = 0 \qquad (8.37)$$

which has the proper boundary conditions. Moreover, since electrostatics is a linear theory, the decomposition $V(\xi, \eta) = V(\eta) + u(\xi, \eta)$ will propagate till the final capacitance C_{tot} which we expect to be equal to the already calculated C_0 (Equation 8.25) plus a ΔC to be estimated.

Since we make the reasonable assumption that all the relevant functions of η are in $L^2([0, 1[)$, then we can use as an orthonormal basis of this space of function the Sturm-Liouville eigenfunctions $\Phi_j^{SL}(\eta)$, ([24]) with j=0,1,2,3.., such that they obey the eigenvalue equation:

$$L_\eta \Phi_j^{SL}(\eta) = \lambda_j^{SL} \Phi_j^{SL}(\eta) \qquad (8.38)$$

where the set of λ_j^{SL}, j=0,1,2,3.., is the set of Sturm-Liouville eigenvalues, which can be proven to be always positive ([24]).

This set of eigenfunction can be proved to be a complete orthonormal set of functions for $L^2([0, 1[)$, which means:

$$< \Phi_j^{SL}(\eta) | \Phi_k^{SL}(\eta) > = \delta_{j,k} \qquad (8.39)$$
$$\sum_j |\Phi_j^{SL}(\eta) > < \Phi_j^{SL}(\eta)| = 1_{L^2} \qquad (8.40)$$

where 1_{L^2} is the identity operator in L^2. Due to this, each function $f(\eta)$ in this space can be written as

$$f(\eta) = \sum_{j=0}^{\infty} f_j \Phi_j^{SL}(\eta) = \sum_{j=0}^{\infty} < \Phi_j^{SL}(\eta) | f(\eta) > \Phi_j^{SL}(\eta) \qquad (8.41)$$

This holds true even for the u function of the potential and we can say:

$$u(\xi, \eta) = u_\xi(\eta) = \sum_{j=0}^{\infty} c_j(\xi)\Phi_j^{SL}(\eta) = \sum_{j=0}^{\infty} < \Phi_j^{SL}(\eta)|u_\xi(\eta) > \Phi_j^{SL}(\eta) \qquad (8.42)$$

Applying the Laplace operator one gets:

$$[L_\xi + L_\eta] \sum_{j=0}^{\infty} c_j(\xi)\Phi_j^{SL}(\eta) \qquad (8.43)$$

$$\sum_j L_\xi[c_j(\xi)]\Phi_j^{SL}(\eta) + \sum_j c_j(\xi)L_\eta\Phi_j^{SL}(\eta) = 0 \qquad (8.44)$$

$$\sum_j L_\xi[c_j(\xi)]\Phi_j^{SL}(\eta) + \sum_j c_j(\xi)\lambda_j^{SL}\Phi_j^{SL}(\eta) = 0 \qquad (8.45)$$

since 8.38 holds. Therefore, one is left with

$$L_\xi[c_j(\xi)] + \lambda_j^{SL}c_j(\xi) = 0 \qquad (8.46)$$

which, more explicitly, reads

$$[(\xi^2 - 1)c_j^{'}(\xi)]^{'} + \lambda_j^{SL}c_j(\xi) = 0 \qquad (8.47)$$

This is a Legendre-like equation. Indeed, the general Legendre equation, for a complex function $f(z), z \in C$, reads:

$$[(z^2 - 1)f^{'}(z)]^{'} - \nu(\nu + 1)f(z) = 0 \qquad (8.48)$$

for each $\nu \in C$ and $z \in C/\ ]-\infty, 1]$. Therefore, in our case, since each eigenvalue λ_j^{SL} is real, we can claim $\nu(\nu + 1) \in R$ which has the solution $\nu = -1/2 + iq$, with q a real number related to the eigenvalues by $q_j = \sqrt{\lambda_j^{SL} - 1/4}$. As we will see in Section 8.5, a numerical treatment of the Sturm-Liouville equation provides all the eigenvalues, which are found to be always greater than $1/4$, so the last square root is well defined.

Following ([25]), the general solution of this Legendre equation can now be written as:

$$c_j(\xi) = b_j B_{\nu_j}^0(\xi) + d_j D_{\nu_j}^0(\xi) \qquad (8.49)$$

where the set of b_j and d_j are unknown constants, and $\nu_j = -1/2 + iq_j$.

Before coming to the determination of these constant, some detail on the Legendre functions $B_{\nu_j}^0(\xi)$ and $D_{\nu_j}^0(\xi)$, which are called Legendre function of the first and second kind, respectively. In ([25]) one can find integral representations:

$$B_{\nu_j}^0(\xi) = \frac{\sqrt{2}}{\pi} \cosh \pi q_j \int_0^\infty dx \frac{\cos q_j x}{\sqrt{\xi + \cosh x}} \qquad (8.50)$$

$$D_{\nu_j}^0(\xi) = \frac{1}{\sqrt{2}}[\int_0^\pi dx \frac{\cosh q_j x}{\sqrt{\xi - \cos x}} - i \sinh \pi q_j \int_0^\infty dx \frac{e^{-iq_j x}}{\sqrt{\xi + \cosh x}}] \qquad (8.51)$$

While the B functions are real, the D functions are generally complex. This could be a problem since we need real physical expressions.

A second check that one can do on the Legendre functions involves their behaviour at $\xi \to 1$ and $\xi \to \infty$. In $(^{25})$ one can find that:

$$\lim_{\xi \to 1} B^0_{\nu_j}(\xi) = 1 \tag{8.52}$$

$$\lim_{\xi \to \infty} B^0_{\nu_j}(\xi) = 0 \tag{8.53}$$

and

$$\lim_{\xi \to 1} D^0_{\nu_j}(\xi) = ln(\xi - 1) \tag{8.54}$$

$$\lim_{\xi \to \infty} D^0_{\nu_j}(\xi) = 0 \tag{8.55}$$

As can be seen only one behaviour is not well defined, i.e. $ln(\xi - 1)$. Indeed, in $\xi = 1$ this limit diverges. Due to this problem, two possibilities arise: or one excludes the D Legendre functions giving as a motivation this bad behaving limit or one keeps also these functions believing that the divergence will disappear in the relevant physical expressions.

In the beginning, we tried with the second possibility: it would not be, indeed, the first time for a divergence to disappear in the relevant physical formulas. Examples can be found even in electrostatics $(^{13})$, if, for instance, the electric potential of an infinite charged line is considered. By standard calculations even this potential will present a divergence, but it will not propagate into the electric field (and so in the capacitance, in our case). Being the Legendre equation a second order differential equation, one needs two boundary conditions to have a unique solution. The first conditions we chose is related to the need to truncate somewhere the tip. So far, indeed, the hyperboloidal surface have been considered infinite, an assumption, which, of course, is not physically acceptable. An infinite surface would mean an infinite charge and then an infinite amount of energy which is impossible. We decide to cut the tip imposing that, from a specific ξ_{max} outward, the potential V is zero. This assumption, a Dirichlet boundary condition, introduces an approximation but it seems a reasonable way to cut the problem since we expect the potential to decrease to zero as long as we get far from the tip.

As a second boundary condition, instead, we chose $c'_j(\xi_{max}) = 0$, which means that we are not dealing with Dirichlet boundary conditions but Neumann's ones. This condition, impose an internal ($\xi < \xi_{max}$) region independent from the external one, and seemed to us a reasonable way to describe the system.

Unfortunately, after setting the boundary conditions, the solution of the problem

gave us a final capacitance formula too big with respect to the expected order of magnitude, $10^{-18}F$.

This is why, we decided, in the end, for the first option dealing only with B Legendre function. Moreover, in this way, one reduces the problem since the only coefficients to be calculated will be the b_j.

So, let $V(\xi_{max}, \eta) = 0$ be the first and unique boundary condition, as well. Then, one can write

$$V(\eta) + \sum_j [b_j B^0_{\nu_j}(\xi_{max})]\Phi^{SL}_j(\eta) = 0 \tag{8.56}$$

Since $V(\eta) \in L^2([0, 1[)$, then we can decompose even this function by the Sturm-Liouville eigenfunctions and write

$$V(\eta) = \sum_j <\Phi^{SL}_j(\eta)|V(\eta)> \Phi^{SL}_j(\eta) \tag{8.57}$$

Therefore we get

$$b_j B^0_{\nu_j}(\xi_{max}) = - <\Phi^{SL}_j(\eta)|V(\eta)> \tag{8.58}$$

which means

$$b_j = \frac{- <\Phi^{SL}_j(\eta)|V(\eta)>}{B^0_{\nu_j}(\xi_{max})} \tag{8.59}$$

Finally, we can write the electric potential as:

$$V(\xi, \eta) = V(\eta) + u(\xi, \eta) \tag{8.60}$$

$$V(\eta) = \frac{V}{ln(\frac{1+\eta_0}{1-\eta_0})} ln\ (\frac{1+\eta}{1-\eta}) \tag{8.61}$$

$$u(\xi, \eta) = \sum_j \frac{- <\Phi^{SL}_j(\eta)|V(\eta)>}{B^0_{\nu_j}(\xi_{max})} B^0_{\nu_j}(\xi)\Phi^{SL}_j(\eta) \tag{8.62}$$

8.4.2 The capacitance

Once the electric potential is found, one can obtain the capacitance of the capacitor following standard electrostatics.

Firstly, the electric field can be calculated by the gradient in prolate spheroidal coordinate:

$$\vec{E} = -\vec{\nabla}V = -\frac{\hat{\xi}}{h_\xi}\frac{\partial V}{\partial \xi} - \frac{\hat{\eta}}{h_\eta}\frac{\partial V}{\partial \eta} = -\hat{\xi}E_\xi(\xi, \eta) - \hat{\eta}E_\eta(\xi, \eta) \tag{8.63}$$

where $\hat{\xi}$ and $\hat{\eta}$ are the coordinate unit vectors (versors).

Secondly, the charge density on the tip's surface can be obtained by Coulomb's theorem

$$\sigma = \epsilon_0[\vec{E} \cdot (-\vec{\eta})]_{tip} \tag{8.64}$$

where $-\hat{\eta}$ is the outwards unit vector perpendicular to the surface of the tip.

Once the charge density σ is known, the total electric charge on the tip's surface can be calculated by integration on the tip's surface S in prolate spheroidal coordinates:

$$Q = \int_S \sigma dS = \int \sigma h_\xi h_\Phi d\xi d\Phi \qquad (8.65)$$

and so the capacitance of the hyperboloidal capacitor is obtained as $C_{tot} = Q/V$.

All the calculation are straightforward so, here, we only report the capacitance C:

$$C_{tot} = C_0 + \Delta C \qquad (8.66)$$

$$C_0 = \frac{2\pi\epsilon_0 a(1-\eta_0^2)}{V}(\xi_{max}-1)V^{'}(\eta_0) \qquad (8.67)$$

$$\Delta C = \frac{2\pi\epsilon_0 a(1-\eta_0^2)}{V}\sum_j \frac{-<\Phi_j^{SL}(\eta)|V(\eta)>}{B_{\nu_j}^0(\xi_{max})}\Phi_j^{'SL}(\eta_0)\int_1^{\xi_{max}} d\xi B_{\nu_j}^0(\xi)$$

With a numerical integration, see section 8.6, setting $V = 1$, ΔC was estimated to be equal to 1%. This is a small correction for the leading term and indeed this was what we were expecting since already C_0 is of the right experimental order of magnitude ([11],[8]). From these works ([11],[8]), we can not say if such a correction is measurable.

A final important remark on the b_j. Due to their relation with the inverse of the $B_{\nu_j}^0(\xi_{max})$, a question arises: does this expression diverge, i.e. does $B_{\nu_j}^0(\xi_{max})$ ever vanish?

A plot of the function for several j gave us a positive answer: the function is strongly oscillating and several zeros can be found in it. This is a critical point of our treatment which we overcame in the following way: in the capacitance formula a sum in j is present which, obviously, can not be numerical estimated due to its infinite terms. A truncation is needed. Numerical plot of the final result with respect to j_{max}, led us to assume only the first ten j-terms of the sum relevant, up to a certain precision to be estimated. Since plots of B_j functions, showed us the first zero to progressively decrease towards $\xi = 1$, as j is increased, we decided to assume ξ_{max} slightly smaller then the first zero of $B_{\nu_{10}}^0(\xi)$. Automatically, the range $1 < \xi < \xi_{max}$, will be well defined for each $j < j_{max}$.

8.4.3 The phase and frequency shift

From the total capacitance C_{tot} (Equation 8.66), we can calculate the phase shift variation taking into account also the ξ contribution. Thanks to the linearity of the theory, we expect it to be equal to the previous one (Equation 8.29) plus a

contribution related to the Legendre functions and the Sturm-Liouville first deriva-
tives. In particular, the latter can not be obtained analytically but only numerically.
This calculus is not trivial and its numerical estimation is currently under investiga-
tion. This will allow us to achieve a complete formula for the phase shift variation
therefore, for the moment, we do not report it.

8.5 Sturm-Liouville numerical computation: SLEIGN2

To numerically evaluate the capacitance of the system 8.66, we need the Sturm-
Liouville eigenvalues and eigenfunctions. These, can not be obtained explicitly with
an analytical formula, however, they can be calculated numerically by the Fortran
program SLEIGN2 ([26] and references therein) that will be introduced just in its
main functions.

The general expression of a Sturm-Liouville differential equation for $y(x)$ is:

$$-(p(x)y')' + q(x)y = \lambda w(x)y \qquad (8.68)$$

where $p(x)$, $q(x)$ and $w(x)$ are three general functions of x and $lambda$ is an eigen-
value. Depending on them, **to be specified by the user**, lots of different dif-
ferential equations can be obtained, among them the Bessel equation ($p(x) = -x$,
$q(x) = x - \nu^2/x$, $\nu \in C, w(x) = 0$) and the Legendre equation ($p(x) = (1 - x^2)$,
$q(x) = \nu(\nu + 1)$ $\nu \in C, w(x) = 0$).

After selecting the functions p, q and w, several specifications about the Sturm-
Liouville problem has to be answered. For instance, the kind of x interval (finite or
not), the kind of boundary conditions (Dirichlet, Neumann..) and, of course, if the
user is interested in getting a numerical evaluation of a specific eigenvalue or, maybe,
a numerical estimation of an eigenfunction with its relative plot. Estimations of all
the numerical errors are provided.

For our purposes, we chose:

- p(x)=$1 - x^2$

- q(x)=0

- w(x)=1

- $x \in [0, 0.8]$, where $x = \eta$

- Dirichlet boundary conditions

- all the mathematical requests were defined as - Regular -

- $V = 1$ V

Here, one can find some relevant typical screenshots of the SLEIGN2 program:
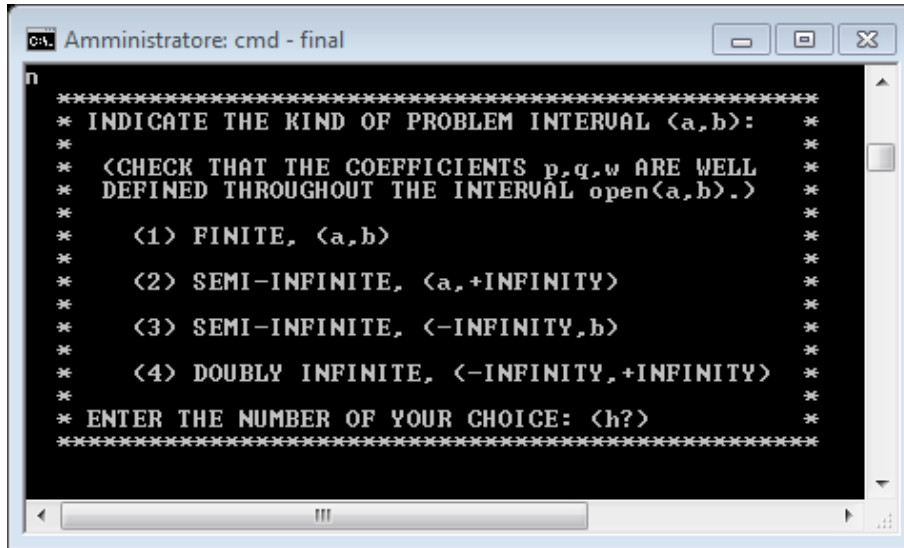
Figure 8.5: SLEIGN2 screenshot asking for the kind of x range under investigation.
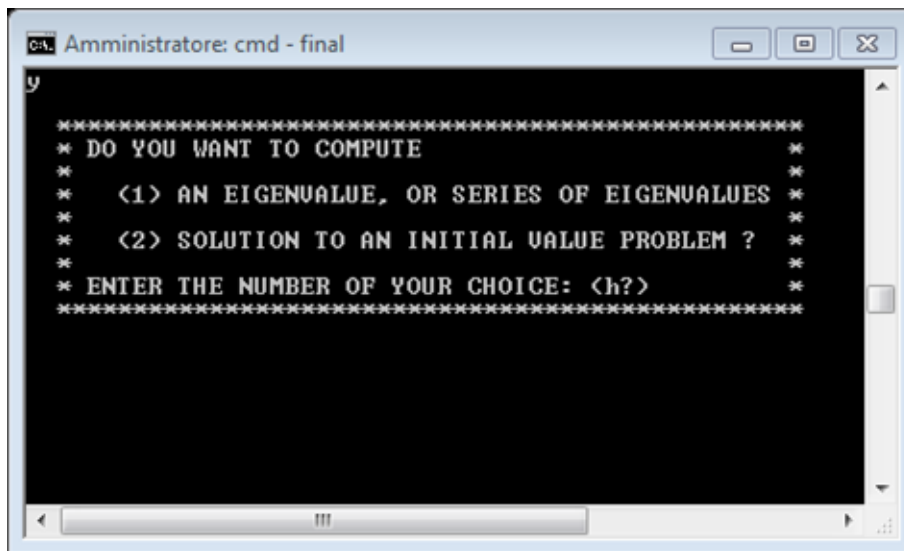
Figure 8.6: SLEIGN2 screenshot question about what the user would like to numerically evaluate.
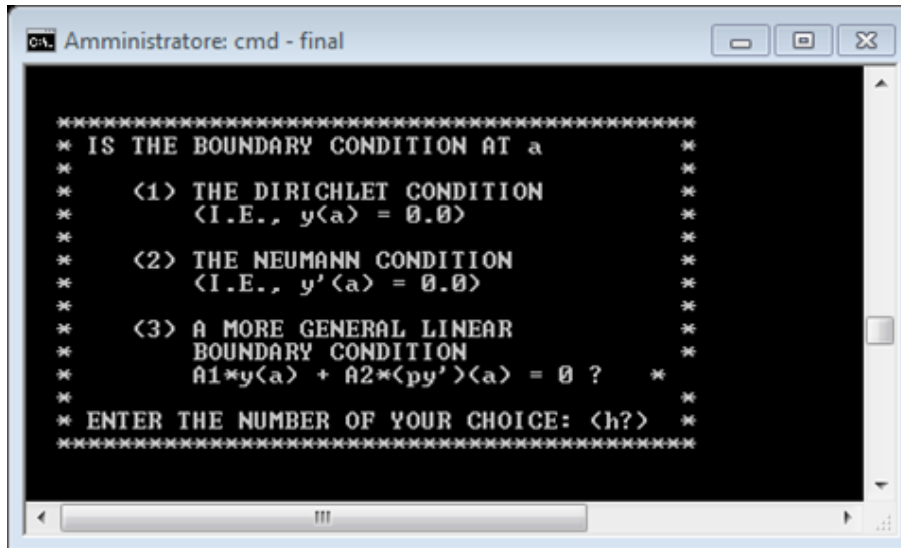
Figure 8.7: SLEIGN2 screenshot asking for details on the boundary conditions.

8.6 Octave computation

To estimate the final capacitance expression 8.66, a numerical integration was done. The Legendre B function integral formula, indeed, is not analytically solvable, therefore, numerical procedures are needed. For this we used Octave ([27]), an open source software. We report here the main code lines to be implemented in Octave to perform the numerical double integration appearing in Equation 8.66.

```
a(1:10) = 0;
for j = 1:10;
for i = 0:10;
a(j) = a(j) + dblquad(@(x,y)(sqrt(2)/pi)*cosh(pi*q(j))*cos(q(j).*x)./sqrt(y+cosh(x)),
0+10*i,10+10*i,1,1.0004);
i++;
endfor;
j++;
endfor;
```

Some explanation about these code lines: the first line is setting an array a of

ten values initially equal to zero. The first for-loop defines a loop of ten iterations: these are the ten j-value Legendre B function to be integrated. As reported, indeed, in the final part of section 8.4.2, we assume the j-sum to be properly approximated by the first ten j-values. The second i-loop, instead, is a technical trick to be able to perform the integration. Basically, a direct integration on the whole x-range (truncated up to 100), indeed, would give to Octave a too difficult integral. This is due to the highly oscillating behaviour of the B Legendre function. To overcome the problem, therefore, we decided to split the x-range into ten parts (ten units long), to be summed up in order to get the result of the integration from zero to 100.

The fourth code line is the main one since, due to the *dblquad* instruction, the numerical integration is achieved. To be noticed, the final two fields inside the bracket which define the extremes of integration.

8.7 Bibliography

[1] S. Kalinin and A. Gruverman. *Scanning Probe Microscopy. Electrical and Electromechanical Phenomena at the Nanoscale. Vol. II.* Springer (2007)

[2] C. D. Bugg and P. J. King. *J. Phys. E*, **21**, 147 (1988)

[3] M. Nonnenmacher, M. O'Boyle and H. K. Wickramasinghe. *Appl. Phys. Lett.*, **58**, 2921 (1991)

[4] B. D. Terris, J. E. Stern, D. Rugar and H. J. Mamin. *Phys. Rev. Lett.*, **63**, 2662 (1989)

[5] C. Gomez-Navarro, A. Gil, M. Alvarez, P. J. De Pablo, I. Moreno-Herrero, F. Horcas, R. Fernandez-Sanchez, J. Colchero, G.-H. J. and A. M. Baró. *Nanotechnology*, **13**, 314 (2002)

[6] A. Verdaguer, G. M. Sacha, H. Bluhm and M. Salmeron. *Chem. Rev.*, **106**, 1478 (2006)

[7] S. Gomez-Monivas, J. J. Saenz, M. Calleja and R. Garcia. *Phys. Rev. Lett.*, **91**, 056101 (2003)

[8] G. Gomila, J. Toset and L. Fumagalli. *Journal of Applied Physics*, **104**, 024315 (2008)

[9] S. Belaidi, P. Girard and G. Leveque. *Journal of Applied Physics*, **81**, 1023 (1997)

[10] L. Fumagalli, G. Ferrari, M. Sampietro, I. Casuso, E. Martinez, J. Samitier and G. Gomila. *Nanotechnology*, **17**, 4581 (2006)

[11] L. Fumagalli, G. Ferrari, M. Sampietro and G. Gomila. *Applied Physics Letters*, **91**, 243110 (2007)

[12] A. M. Russell. *Journal of Applied Physics*, **33**, 970 (1962)

[13] J. D. Jackson. *Classical Electrodynamics*. John Wiley ans Sons (1998)

[14] P. Girard, M. Ramonda and D. Saluel. *J. Vac. Sci. Technol. B*, **20**, 1348 (2002)

[15] S. Hudlet, M. Saint Jean, C. Guthmann and J. Berger. *The European Physical Journal B*, **2**, 5 (1998)

[16] S. Gomez-Monivas, L. S. Froufe-Perez, A. J. Caamano and J. J. Saenz. *Appl. Phys. Lett*, **79**, 4048 (2001)

[17] S. Patil, A. V. Kulkarni and C. V. Dharmadhikari. *Journal of Applied Physics*, **88**, 6940 (2000)

[18] V. J. Peridier, L.-H. Pan and T. E. Sullivan. *Journal of Applied Physics*, **78**, 4888 (1995)

[19] A. Passian, A. Wig, F. Meriaudeau, M. Buncick, T. Thundat and T. L. Ferrell. *Journal of Applied Physics*, **90**, 1011 (2001)

[20] O. D. Momoh, M. N. O. Sadiku and C. M. Akujuobi. *Microwave and optical technology letters*, **51**, 2361 (2009)

[21] S. Gasiorowicz. *Quantum Physics*. John Wiley and Sons, Inc (2003)

[22] A. Passian, S. Koucheckian, S. B. Yakubovich and T. Thundat. *J. Math. Phys.*, **51**, 023518 (2010)

[23] Y. Shen, D. M. Barnett and P. M. Pinsky. *Applied Physics Letters*, **92**, 134105 (2008)

[24] M. A. Al-Gwaiz. *Sturm-Liouville Theory and its Applications*. Springer (2008)

[25] W. Magnus, F. Oberhettinger and R. P. Soni. *Formulas and Theorems for the Special Functions of Mathematical Physics*. Springer (1966)

[26] 'SLEIGN2 website:'. http://math.niu.edu/SL2/

[27] 'Octave website:'. http://gnu.org/software/octave/

Chapter 9

Observation of flat-lying molecules layer by AFM

When conjugated oligomers, like 6T, are deposited on chemically inert and flat silicon oxide surfaces, firstly form stable nucleus of few molecules. Subsequently, nucleus evolve as islands during the deposition and coalesce one each other to form a continuous organic layer ([1]). The film growth is characterized by two contemporaneous molecular configurations: the upright configuration of the islands and the flat-lying configuration in between of them ([2]).

During the film's growth, these flat-lying molecules can affect islands coalescence in two ways: if they remain flat, an empty space in between islands is created; otherwise, if they are collected from islands, the interfacial disorder between islands is increased (domain boundaries) ([3]).

To utilize these films in electronic and optoelectronic devices, the molecular orientation with respect to the substrate is crucial: for Organic Light Emitting Diodes (OLEDs) or solar cell applications, growth of the molecules should preferably occur in a lying fashion. This allows for the charge carrier transport, which is perpendicular to the molecule's long axis, between the electrodes as is illustrated in Figure 9.1. For OTFTs, instead, growth of standing molecules is desired on the gate oxide between source and drain.

These flat lying molecules are observed in the case of sexithiophene sub-monolayer films deposited on thermal silicon dioxide surfaces. Photoluminescence spectroscopy (PS) has revealed crucial information on the molecular organization allowing to identify a significant population of domains made of 6T molecules lying flat in direct contact with the substrate ([4]). PS has allowed for the first time to provide insight into the initial growth stages of organic films in reason of the 6T J-aggregates formed on thermal SiO_2 ([5]). In 2011, these 6T flat-lying aggregates on thermal SiO_2 have

been directly imaged by Ultrasonic Force Microscopy (UFM) ([6]).

PS has failed to image flat-lying molecules on native SiO_x. On the other side, recently, SPM techniques such as Lateral Force Microscopy, Atomic Force Microscopy (in tapping mode) proved to be a powerful tool to investigate the mechanical properties of the flat lying molecular layer on native silicon oxide, while, Ultrasonic Force Microscopy, allowed a direct identification of it ([2]).

Towards an always more complete way to identify flat lying molecules layers, we present in this chapter unprecedent (up to our knowledge) UHV non contact AFM images of 6T flat lying molecules aggregates, both on thermal silicon oxide and on top of 6T islands.
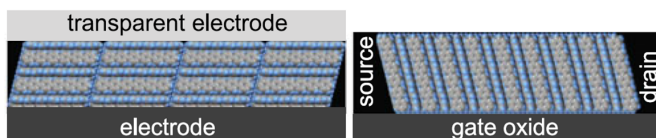

Figure 9.1: (left) Desired molecular orientation for OLEDs or organic solar cells. (right) arrangement for an OTFT application.

9.1   Experimental details

The experiment was performed with the VT AFM microscope described in Chapter 5 in UHV ($10^{-8} mbar$).

All the non contact AFM images were achieved with MikroMasch AFM cantilevers (NSC 35) with resonance frequency of 318 kHz.

The substrate was thermal silicon dioxide, with a thickness of 223 nm. Before deposition it was not chemically treated: once a $1cm^2$ region was cut from a wafer (p-type, 1-10 $\Omega \cdot cm$), properly stocked to avoid any environmental contamination, then it was directly put inside the microscope FEL.

The heating procedure of the OME cell was done exactly in the way described in Chapter 4.

$\sim 30\% ML$ of 6T was deposited on the substrate after a 4 minutes deposition. This corresponds to a low rate of molecules $\Phi \sim 1 A/min$. The substrate was kept at RT.

The main microscopy details were the following:

- generator oscillation amplitude = 0.1 V

- gain = 4%

- set point = -35 Hz

- pixel = 400

- scan rate = 0.33 Hz for standard images, up to 1.3 Hz for images with flat lying aggregates

- scan size starting from $2\mu m$ x $2\mu m$ down to a minimum of $70nm$ x $70nm$

9.2 Results

While performing a routine experiment (a RT calibration), we noticed the height of the 6T islands to be close to 3 nm instead of the common 2.4 nm. This led us to think about a flat lying molecules layer on top of standard up-right 6T molecules deposited on the substrate.

In Figure 9.2, the first four images can be seen, starting from a scan size of $1\mu m$ x $1\mu m$, down to $200nm$ x $200nm$. For image 1) and 3) the height profiles of three and one islands, respectively, is reported in Figure 9.3. In Figure 9.4, instead, we report a Gwyddion (see Section 2.6) step fit (Gwyddion $\rightarrow$ Fit critical dimension $\rightarrow$ Fit) of the first island (on the left) of the height profile shown on the right of Figure 9.3. As can be seen, the fit is evaluating the step to be $(3.0 \pm 0.2)nm$, a value not in agreement with the standard 2.4 nm height of 6T molecules.

Already in the image 4) some rod like features are visible both on the substrate and on top of 6T island. To be sure not to be in front of an artifact we tilted the scanning of 45 degrees obtaining image 1b) of Figure 9.5. As can be appreciated, the whole image has rotated of 45 degrees, the 6T island **together** with the rod like features. This can be taken as a strong sign that those features are not artifact. Moreover, to see better the flat lying molecules layer and check if they down scale with the image we achieved a zoom down to $160nm$ x$160nm$ and $70nm$ x$70nm$, obtaining images 2) and 3) of Figure 9.5. As can be seen, the features appear bigger as it should be for real objects after zooming.
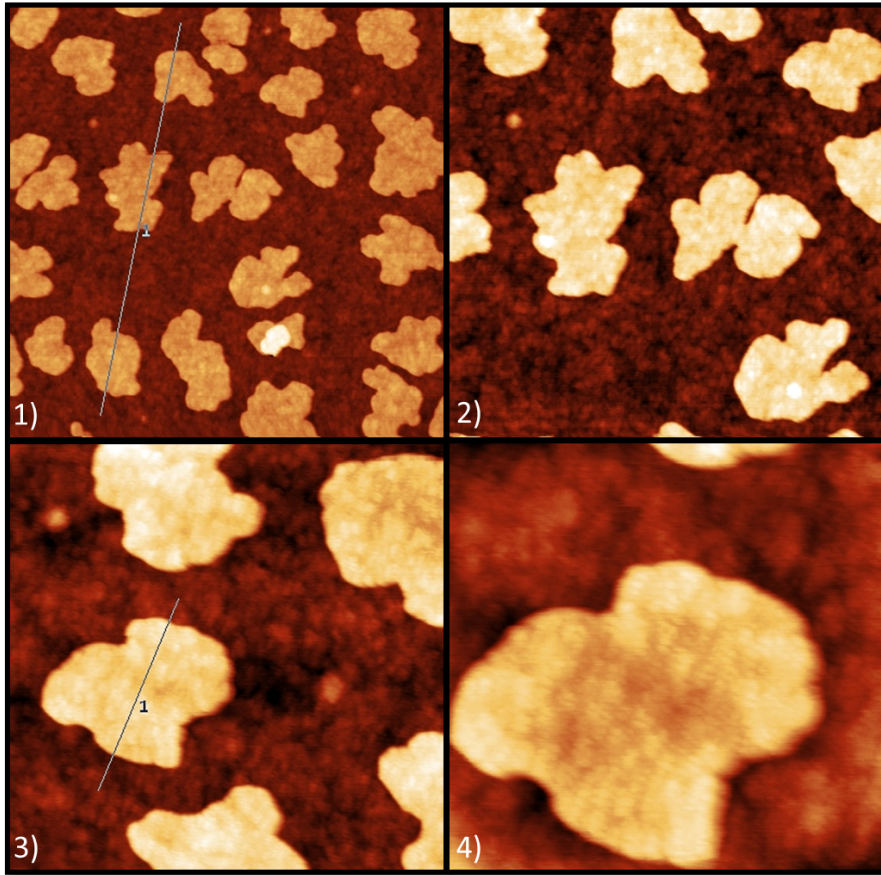
Figure 9.2: 6T islands on thermal silicon oxide. 1)$1\mu m$ x $1\mu m$ 2)Zoom of the central part of the first image. Scan size: $700nm$ x $700nm$ 3)Zoom of the upper-right part of the second image. Scan size: $400nm$ x $400nm$ 4)Zoom of image 3). Scan size: $200nm$ x $200nm$
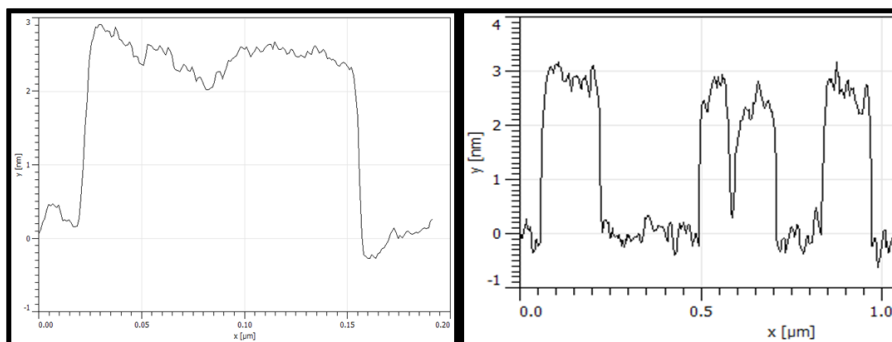

Figure 9.3: Height profiles of 6T islands of images 1) and 3) of Figure 9.2. The threshold of 3 nm is quite close to the top of the islands.
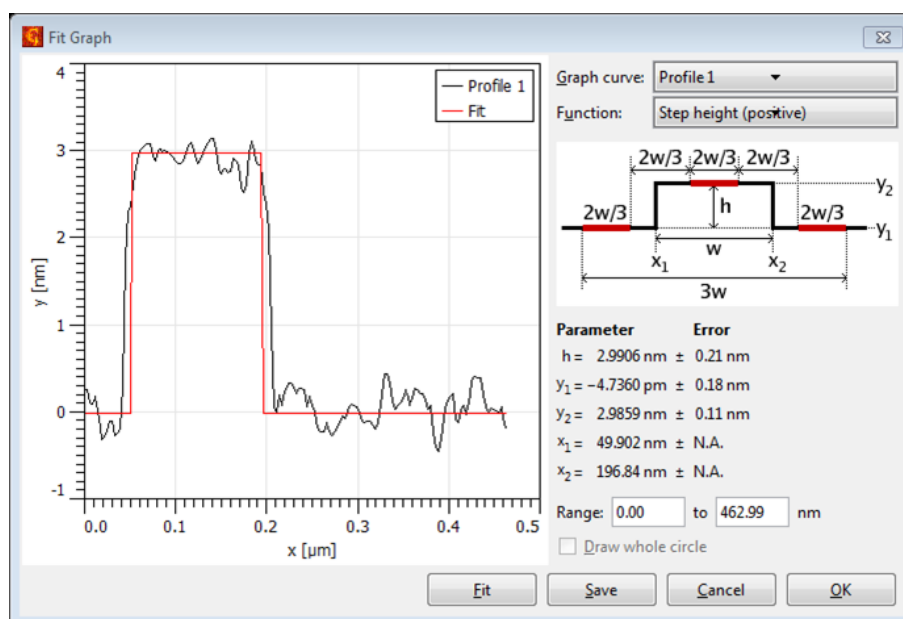
Figure 9.4: Step-like fit of the first island (from the left) of the height profile on the right of Figure 9.3. The parameter h, giving the height of the step, is evaluated: $(3.0 \pm 0.2)nm$

9.3   Data analysis

Assuming we are in front of a flat lying layer, the question is now to check the typical dimension of the rod like features. As a first step we achieve a height profile of a specific zone of the image where four features can clearly be seen. These are visible in Figure 9.6, where exactly four mounds in the height profile can be distinguished. Deciding to take as a typical transverse dimension of each feature the average of the distance between two consecutive height minimums in the height profile, we look for the minimum, measure them and calculate the average. In Figure 9.7 the x position of each minimum can be seen. From here an average (out of the four mounds) $\xi = (4.2 \pm 0.9)nm$ can be calculated, with the discrepancy as the error bar since we have a non statistical sample of measurements. We are far from the 2.4 nm typical length of the 6T molecules but the chosen method is still quite rough.

Looking for a better evaluation of the typical transverse dimension of the flat lying molecules we achieve a (horizontal direction) Power Spectrum Density Function (PSDF) method ([7,8]), directly in Gwyddion with the option: $Calculate$ $1D\, statistical\, functions$. To do this, we make use of all the images were the flat lying molecules are clearly visible (image 1b), 2) and 3)), get the correspondent correlation lengths and associate as a total error bar the discrepancy of the three values.
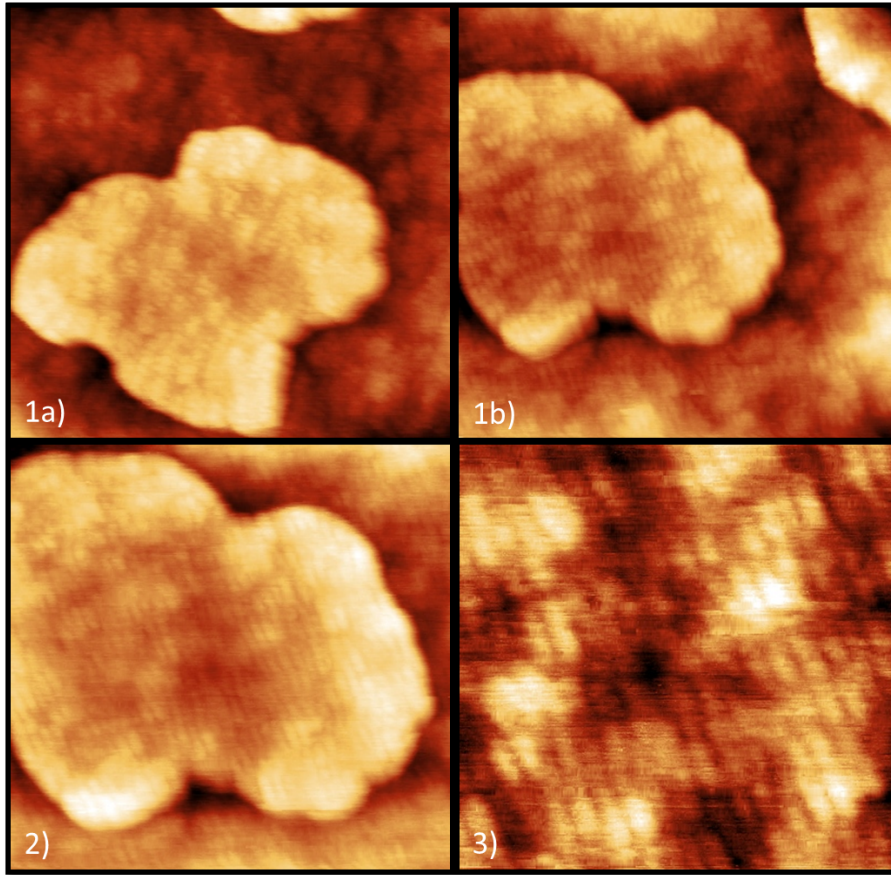
Figure 9.5: 1a)6T island on thermal silicon oxide. Scan size: $200nm$ x $200nm$ 1b) 45 degrees clockwise rotation of image 1a) showing the rod like features rotating as well and confirming that we are not dealing with an artefact. Scan size: $200nm$ x $200nm$ 2)Zoom of image 1b). Scan size: $160nm$ x $160nm$ 3)Zoom of image 2). Scan size: $70nm$ x $70nm$.

Since we are interested in the transverse typical length of the AFM image, we first apply a plane subtraction, we fix the zero (see Section 2.6) and then rotate the image in order to have the features under investigation perpendicular to the x axis.

In Figure 9.8, the PSDF plot is reported for image 3). Two main slopes are visible and the $k - vector$ (or wave number) at the intersection (shown on the right screenshot) is roughly $k = 2.08nm^{-1}$. The corresponding wave length, which we interpret as a correlation length ξ or the typical dimension of the AFM image, is then:

$$\xi = \frac{2\pi}{k} = 3.0nm \tag{9.1}$$

For image 2) and 1b), instead, the wave numbers that we obtain following the same procedure are $k = 2.604nm^{-1}$ and $k = 2.728nm^{-1}$, respectively. These corre-
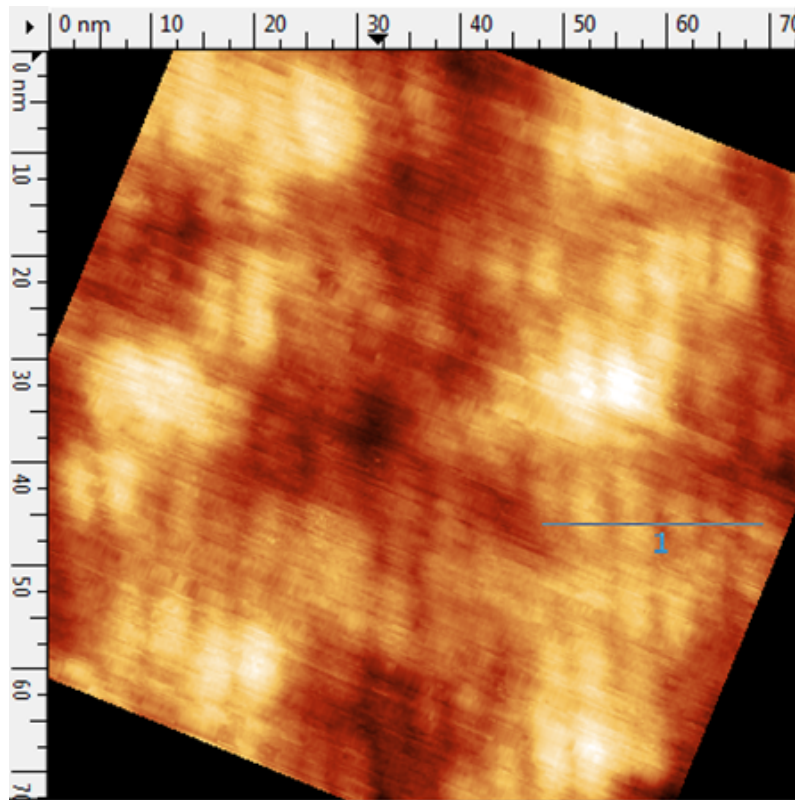
Figure 9.6: Image 3) of Figure 9.5 properly rotated (clockwise) in order to have vertical rod like features. The dimension is $70nm$ x $70nm$.
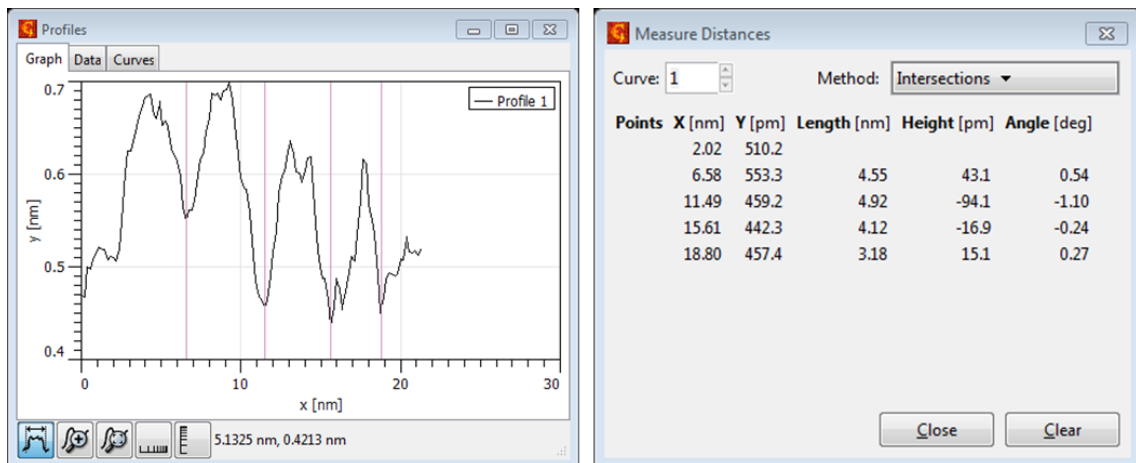

Figure 9.7: Height profile of four features selected in Figure 9.6 and associated measured distances. An average of $(4.2 \pm 0.9)nm$ distance between two consecutive minimums is found.

sponds to wave lengths of 2.4 nm and 2.3 nm.

Making the average and taking the discrepancy as error bar we can conclude, finally,

that the main correlation length in the AFM images is:

$$\xi = (2.6 \pm 0.4)nm \tag{9.2}$$

which is in complete agreement with the standard 2.4 nm chain length of 6T molecules.
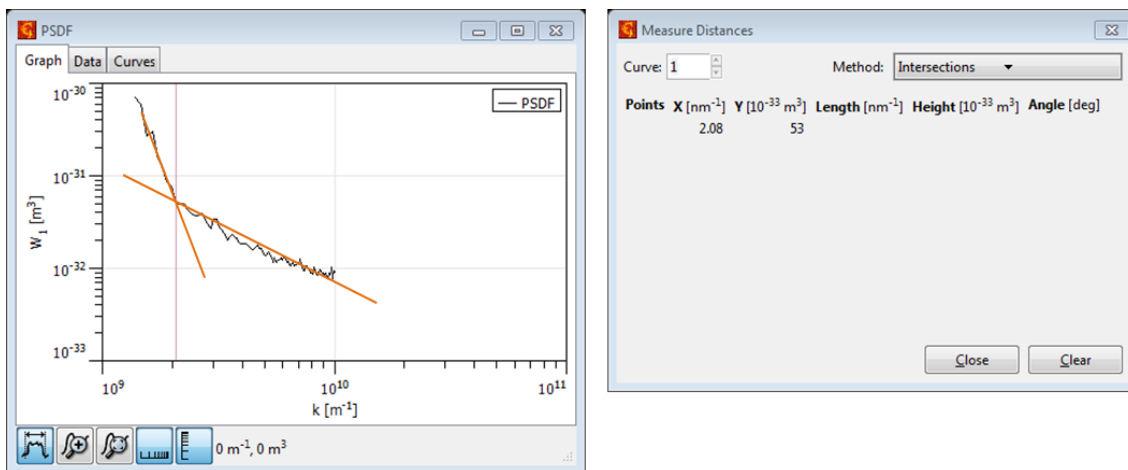

Figure 9.8: Relevant part of the PSDF of figure 9.6. The two main slopes are visible (left). Measured x and y position of the cross point between the two slopes (right).

To conclude, we have proven, after depositing 6T molecules on thermal silicon oxide (223 nm) kept at RT, that $(2.6 \pm 0.4)nm$ wide features are present both on the substrate and on top of 6T islands. Our idea is that these are flat lying molecules aggregates where lots of single flat lying molecules are packed together to form long rod like features.

Despite the AFM observation of flat lying molecules aggregates, still there are several open questions:

- is the whole experiment reproducible?

- are these aggregates present also on native silicon dioxide?

- are these aggregates still present if we change the temperature of the substrate?

Regarding the first question, in the future, we will try to observe again this flat lying molecules layer by non contact AFM in UHV. During the PhD period we

tried several times without success. We guess the contribution of the (not known) sharpness of the AFM tip can be a very relevant parameter affecting the possibility to achieve such high resolution AFM images.

In the end of this section, we also report another experimental observation perhaps related to a flat lying molecules layer.

During one of the trails to achieve the RT in-situ AFM experiment with the VT AFM microscope, we obtained the peculiar 6T morphology images shown in Figure 9.9 and 9.10.
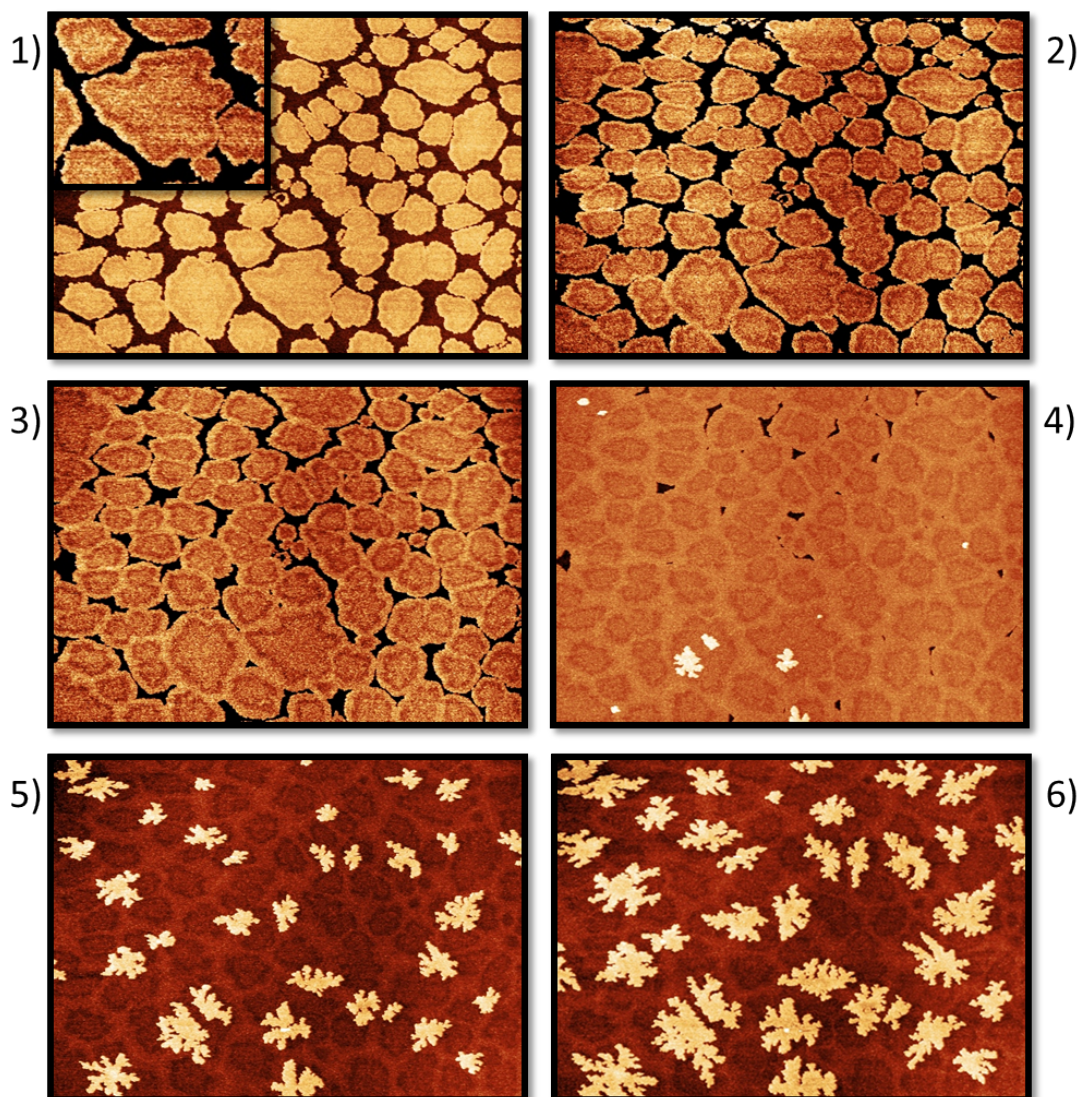

Figure 9.9: 6T AFM images showing the morphological evolution of a peculiar topography: a border decoration plus a layer of molecules on the basal plane of each island is present. In between them, a depletion zone. 1)0.7ML with inset of the bottom central island 2)0.8 ML 3)0.9ML 4)1ML 5)1.1ML and 6)1.3ML
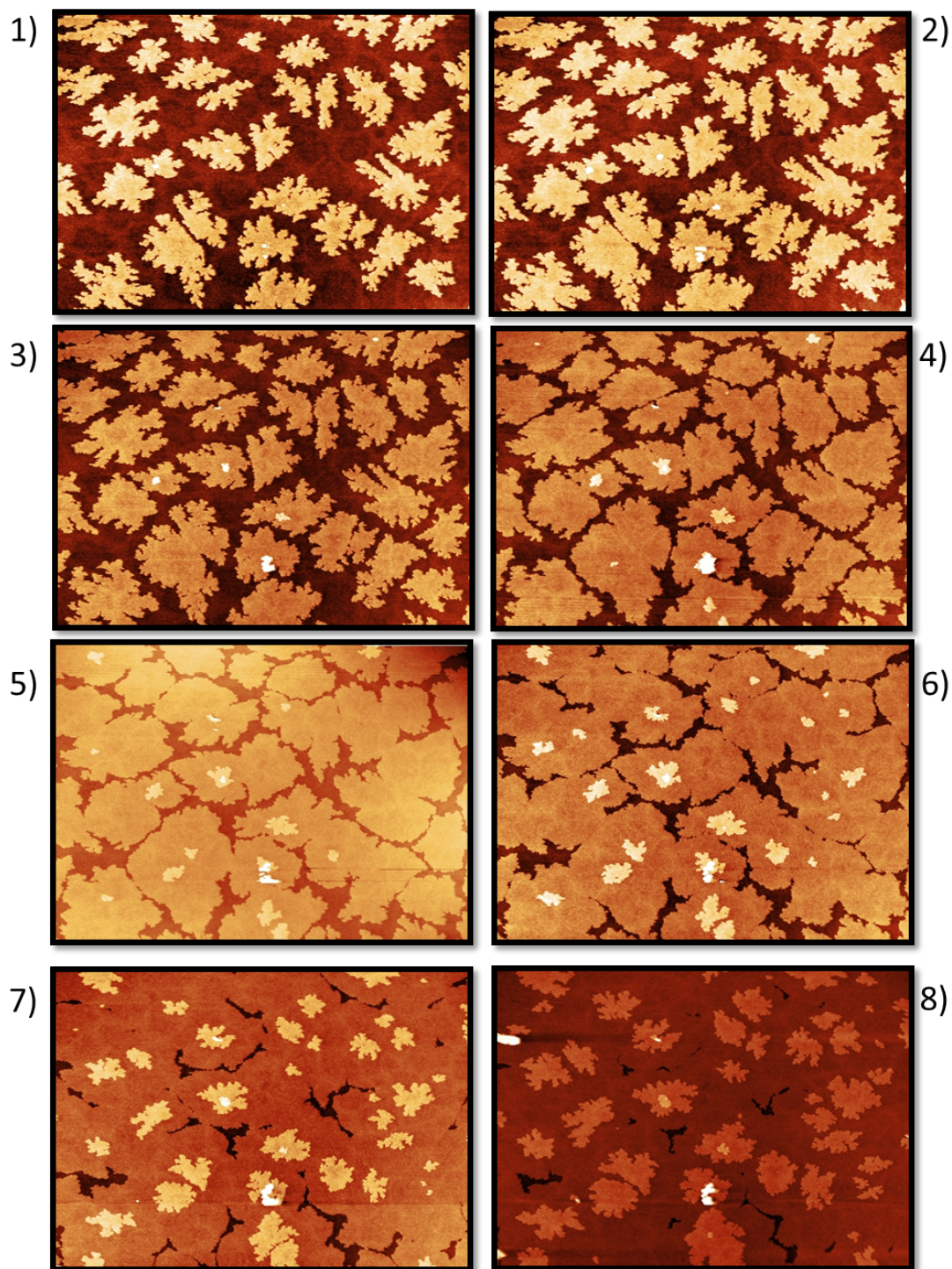
Figure 9.10: Morphological evolution of 6T topography shown in Figure 9.9. 1)1.4ML 2)1.5ML 3)1.6ML 4)1.7ML 5)1.8ML 6)1.9ML 7)2.1ML and 8)2.2ML

The 1 cm^2 substrate we used was cut from a wafer of native silicon oxide (boron doped, p-type, 5-10 $\Omega \cdot cm$), properly stocked to avoid any environmental contami-

nation. The experiment was achieved in UHV ($2x10^{-9}$mbar). The AFM cantilever had a resonance frequency of 330 kHz (Nanosensors), the scan size was $6\mu m$ x $6\mu m$, the scan frequency 0.3 Hz, the generator oscillation amplitude 0.1 V, the typical gain 5% and the standard set point -45Hz.
Each deposition lasted four minutes and the typical coverage step was 0.1 ML corresponding to a low rate of deposition of $\sim 1A/min$.

In the figures, showing the morphological evolution of the thin film, we report the relevant topographies for our purposes, from 0.7ML up to 2.2ML. We are in front of a standard layer by layer growth of 6T on native silicon oxide. In the first image we are in the aggregation regime, while, in image 2), at 0.8 ML, the coalescence it taking place. In order to have percolation the image 4), at 1ML, has to be considered. Then, after the first layer has been completed, the growth of the second layer starts, again in a layer by layer way, even if a small coverage of the third layer is already appeared before the second one has been completed (last images).

As clearly visible from the first image of Figure 9.9, each 6T island shows a marked border decoration plus a layer of molecules covering the basal plane of the island. A depleted zone appears in between such regions that can not be measured by using the height profile because of the noise induced by the image size. Such island decoration is promoted by 6T molecules deposited on its basal plane during the film growth. This process appears in the sub-monolayer regime and it goes on for every coverage, including islands coalescence and percolation. As qualitatively observed in the inset of Figure 9.9, islands show a comparable colour contrast of the two decorated regions (viz. same height).

Notably, the height of the islands is about 2nm which is lower than the expected island height (2.4nm). The decoration effect disappears for the islands of the second monolayer that are more dendritic than those of the first monolayer. On the other hand, their height remains about 2nm. Moreover, there is no correlation between the centre of the islands of the second monolayer with respect to the centre of the first monolayer islands. This seems in agreement to the step edge effect ([9]), where the island nucleation occurs in correspondence to higher edges of the first monolayer islands. At a first glance, this is true for all islands of the second monolayer (see Figure 9.9) therefore the existence of flat lying molecules on the borders promotes their growth. Of course, this is an hypothesis not confirmed by data analysis, but it seems reasonable.

Experimentally, we can associate these observations to the only one experimental parameter that was changed, viz. the coverage steps. Indeed, all the AFM images

performed during the in-situ quasi real time experiments (see Chapter 7), had 0.2ML as a coverage step whereas, in this case, it was 0.1ML. New experiments are needed for confirming such effect.

To conclude, we report a 6T topography on native silicon oxide which shows higher edges on the 6T islands. We have not yet completely understood the origin of this observation nor we had the possibility to repeat the experiment because it was partially out of the thesis focus. In the next future, we will try to repeat the whole experiment in order to see if this effect is reproducible both on native and thermal silicon oxide, also changing the temperature of the substrate.

9.4   Bibliography

[1] R. Ruiz, D. Choudhary, B. Nickel, T. Toccoli, K.-C. Chang, A. C. Mayer, P. Clancy, J. M. Blakely, R. L. Headrick, S. Iannotta and G. G. Malliaras. *Chemistry of Materials*, **16**, 4497 (2004)

[2] C. Albonetti and F. Biscarini. *Microscopie*, 36 (2011)

[3] P. Annibale, C. Albonetti, P. Stoliar and F. Biscarini. *J. Phys. Chem. A*, **111**, 12854 (2007)

[4] M. A. Loi, E. Da Como, F. Dinelli, M. Murgia, R. Zamboni, F. Biscarini and M. Muccini. *Nat. Mat.*, **4**, 81 (2005)

[5] E. Da Como, M. A. Loi, M. Murgia, R. Zamboni and M. Muccini. *Journal of the American Chemical Society*, **128**, 4277 (2006)

[6] F. Dinelli, C. Albonetti and O. V. Kolosov. *Ultramicroscopy*, **111**, 267 (2011)

[7] F. Biscarini, P. Samorì, O. Greco and R. Zamboni. *Physical Review Letters*, **1**, 2389 (1997)

[8] F. Biscarini, Q. K. Ong, C. Albonetti, F. Liscio, M. Longobardi, K. S. Mali, A. Ciesielski, J. Reguera, C. Renner, S. De Feyter, P. Samori' and F. Stellacci. *Langmuir*, **29**, 13723 (2013)

[9] M. Schneider, M. Brinkmann, M. Muccini, F. Biscarini, C. Taliani, W. Gebauer, M. Sokolowski and E. Umbach. *Chemical Physics*, **285**, 345 (2002)

Chapter 10

Ex-situ AFM imaging of pentacene-C60 bilayer

In this work we elucidate the interplay between Charge Transfer (CT) and interface morphology of the pentacene-C60 heterojunction. The experiment was carried out using an in-situ real time electrical characterization technique which allows the monitoring of electrical performance of a transistor during the growth of the organic semiconductor. This gives us the possibility to relate growth phenomena to device performances.

The work, carried out in my group, was collaborative and my contribution to it has been to perform ex situ AFM imaging on the set of bilayer films and the morphological analysis. The used AFM microscope is described in Chapter 6.

CT processes, such as electron-hole separation or recombination, occur at interfaces between electron and hole transport layers in organic devices such as light emitting diodes, photovoltaic cells (OPVs), light emitting transistors and ambipolar field effect transistors (FET) ([1–4]).
The efficiency of CT depends on the alignment of the energy levels at the heterojunction, as well as on the molecular organization and the morphology of the interface. In ambipolar FETs based on bilayer heterojuctions, the morphology of the bottom layer determines the quality of the heterojunction interface and the charge transport in these devices ([5]). Flat and continuous films in the first semiconducting layer would produce a smooth heterojunction interface. Additional charge carriers accumulated at the heterojunction can fill the trap states and thereby improve carrier transport. In reality, the heterojunction is a rough fluctuating interface with lateral correlation lengths.

In order to explore the role of morphology on CT at the heterojunction, we use in-situ real time electrical characterization technique that enables us to measure

the characteristics of an ambipolar transistor during the growth of the bilayer. As model compounds for the bilayer we chose pentacene as p-type and fullerene (C60) as n-type transporter, because their heterojunction forms a well-characterized donor-acceptor pair. Theoretical studies address the role of molecular architecture ([6,7]), interface geometry ([8]), polarization ([9]) and dipole formation due to electrostatic interaction, however evidence from experimental results is still marginal.
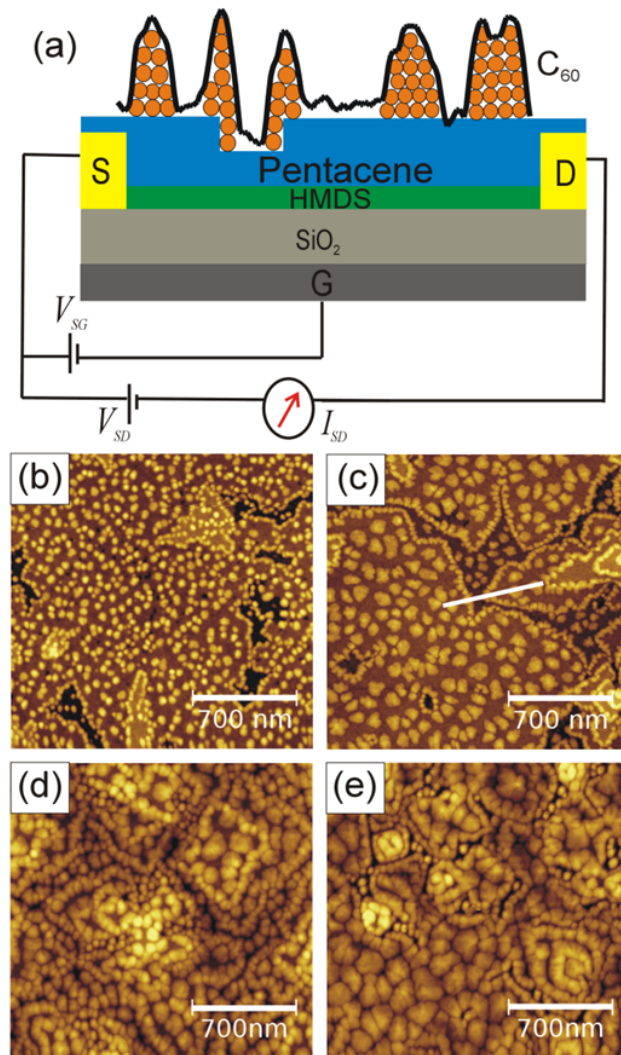

Figure 10.1: Device layout and morphology of bilayer (a) Schematic diagram of ambipolar C60/pentacene FET. The profile drawn in Figure 10.1c is displayed as the envelope of C60 molecules (represented as circles). (b-e) AFM topographical images at different C60 coverage on a 2 ML pentacene film: (b) 0.6 ML (0.5 nm) (c) 1.2 ML (1 nm) (d) 3 ML (2.5 nm) and (e) 6 ML (5 nm).

Our goal has been to investigate how CT process is governed by the change in film

thickness and morphology of the pentacene-C60 heterojunction. We sequentially deposited films of pentacene and C60 with varying thicknesses, while probing in-situ and at real time their electrical transport properties in the direction parallel to the evolving interface. This enabled us to relate percolation of the p-type and n-type charge transport paths, n- and p-type mobility and threshold voltage to film thickness and morphology.

Ex situ AFM imaging was performed on a set of bilayers comprising a $\theta = 2ML$ (3 nm) pentacene film at the bottom and a C60 film with θ_{C60} increasing up to 12.5 ML (10 nm) on top. The morphological evolution is displayed in the AFM micrographs shown in Figure 10.1.

Two distinct features appear: (i) C60 small grains decorate step edges around pentacene islands, while (ii) larger C60 grains nucleate and grow on the basal plane of the island. The latter exhibits lower areal density. The line profile in Figure 10.1a (extracted along the line drawn on the AFM image in Figure 10.1c) suggests that C60 molecules are in intimate contact with pentacene at step edges. Figure 10.1b,c display the early stage of C60 growth on pentacene film: terrace edges are decorated by strings of interconnected C60 grains $\sim$30-60 nm wide and 2.6 nm ($> 3ML$) high, while C60 molecules nucleating on the basal plane form disc shape grains with average diameter 40-80 nm and height 1.6 nm (2 ML). As θ_{C60} increases above 3 ML, the grains in the basal plane grow larger and coalesce into a connected percolation network across the pentacene layer (Figure 10.1d,e).

Having known this morphological evolution of C60 on pentacene, our next step has been to relate the growth phenomena to the electrical characteristics obtained from the in situ real time electrical characterization. Figure 10.2 shows the evolution of electron current I_e in the C60 channel during the growth of C60 on 2 MLs of Pentacene. In the beginning there is a slow rise in current during the initial growth of C60 up to $\theta_{C60} = 2ML$. When $\theta_{C60} > 2ML$ we see a very rapid increase in the electron current. Looking at the AFM images, we can say that the initial rise in the current is actually due to a quasi 1D percolation along the borders of pentacene because at initial growth the C60 grains at the basal plane are disconnected. However, at $\theta > 2ML$, the C60 grains on the basal plane form a 2D percolation network (as we see also from the images from Figure 10.1d-e) and this gives rise to the rapid jump of the electron current. This interpretation has been confirmed using a percolation theoretical model which we will not discuss here.

The main conclusion of this work is that we can clearly demonstrate a direct relation between evolution of film growth on the channel of a transistor and its electrical performances.
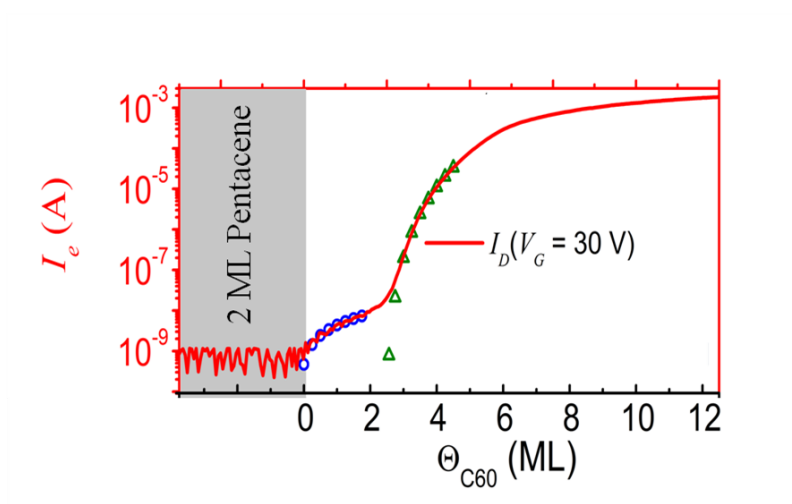
Figure 10.2: Evolution of electron current during C60 growth on 2 ML of pentacene.

10.1   Bibliography

[1] P. Heremans, D. Cheyns and B. P. Rand. *Acc. Chem. Res.*, **42**, 1740 (2009)

[2] N. Koch. *ChemPhysChem*, **8**, 1438 (2007)

[3] M. Muccini. *Nat. Mater.*, **5**, 605 (2006)

[4] A. Rao, M. Wilson, J. M. Hodgkiss, A. S. Sebastian, H. Bassler and R. H. Friend. *J. Am. Chem. Soc.*, **132**, 12698 (2010)

[5] J. Wang, H. Wang, X. Yan, H. Huang and D. Yan. *Appl. Phys. Lett.*, **87**, 093507 (2005)

[6] L. Muccioli, G. D'Avino and C. Zannoni. *Adv. Mater.*, **23**, 4532 (2011)

[7] Y. T. Fu, C. Risko and J. L. Bredas. *Adv. Mater.*, **25**, 878 (2013)

[8] Y. Yi, V. Coropceanu and J. L. Bredas. *J. Am. Chem. Soc.*, **131**, 15777 (2009)

[9] E. F. Valeev, V. Coropceanu, D. A. da Silva Filho, S. Salman and J. L. Bredas. *J. Am. Chem. Soc.*, **128**, 9882 (2006)

Conclusions

To conclude, during the PhD, we have focus on these two main works: an in-situ real time AFM study of organic semiconductor thin film growth on silicon oxide and an Electrostatic Force Microscopy (EFM) theoretical model. Regarding the first experimental issue, we have achieved an almost unprecedent in-situ real time AFM experiment, showing the morphological evolution of alpha-sexithiophene, a benchmark organic semiconductor, on native silicon oxide, a technologically relevant substrate. We report a 2D+3D growth with a roughening transition at the third layer, followed by a rapid roughening. From the AFM images at different substrate temperatures, important morphological parameters like desorption energy, activation-diffusion energies and fractal dimension have been obtained. To have a deeper understanding of the growth kinetics behind the evolution of the ultra thin film on the substrate, we have simulated the growth with a distributed growth model. This model was able to describe the 2D+3D growth, allowing us to conclude that the downward interlayer diffusion is relevant for this kind of growth dynamics. Moreover, due to some discrepancies between the distributed growth model and the experimental data, we suggest that also the upward interlayer current should be taken into account in order to properly describe the evolution of the growth exponent *beta* with substrate temperature.

On the other hand, the theoretical EFM model allowed us a better estimation of the capacitance between an EFM tip and a metallic substrate. This parameter is important to better understand EFM images, Phase-EFM images and to estimate relevant parameters like the dielectric constant of thin films. In the next future, we aim to generalize this EFM model also to the case of an organic ultra thin film in between the EFM tip and the substrate. This could be important for a more precise definition of nucleation center and resolution limit of an EFM microscope.

Moreover, two additional work have been concluded. The first regards UHV non contact AFM images of flat lying molecules layer on thermal silicon oxide and on top of 6T islands. This AFM experimental observation, to our knowledge, was still lacking. The second work, elucidates the interplay between morphology and charge

transport at the heterojunction between two relevant organic semiconductor like pentacene and C60.

...ma ne vale la pena?

SI